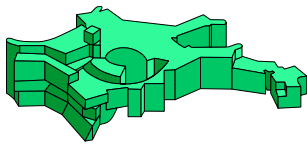
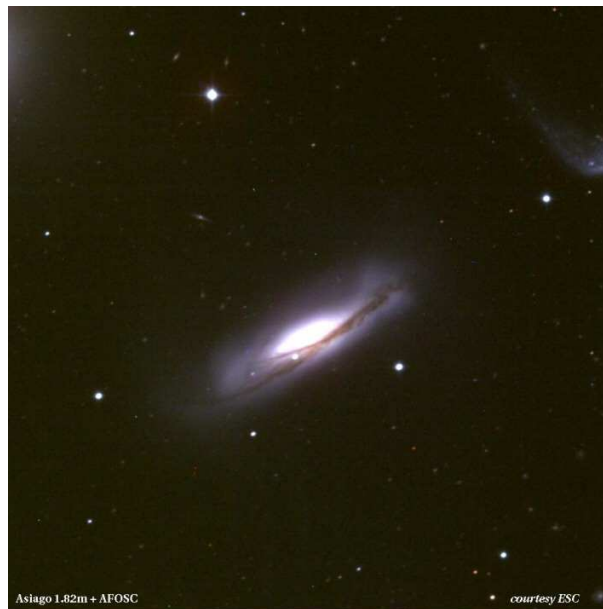
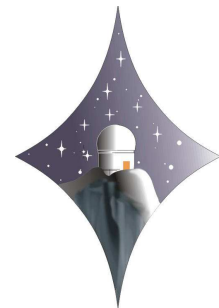


Abundance Tomography of Type Ia Supernovae

Matthias Stehle



Max-Planck-Institut
für Astrophysik



**Abundance Tomography
of
Type Ia Supernovae**

Matthias Stehle

Dissertation
an der Fakultät für Physik
der Ludwig–Maximilians–Universität
München

vorgelegt von
Matthias Stehle
aus Sigmaringen

München, 4. November 2004

Erstgutachter: Prof. Dr. A.W.A. Pauldrach

Zweitgutachter: Prof. Dr. W. Hillebrandt

Tag der mündlichen Prüfung: 22. Dezember 2004

If what one finds is made of pure matter, it will never spoil. And one can always come back. If what you had found was only a moment of light, like the explosion of a star, you would find nothing on your return. But you experienced a light explosion, and that was already worthwhile.

*Paul Coelho (1947-),
The Alchemist*

Abstract

Many uncertainties about the physics of Type Ia Supernovae have been revealed in the recent past, and numerous pieces are puzzled together to achieve a complete description of the phenomenon of thermonuclear explosions in the sky. However, very important parts are still missing. In particular, the concept lacks a proper connection between the various evolutionary steps, namely the progenitor scenario, explosion theory, nucleosynthesis from the burning, and the observations. Early time spectra of Type Ia Supernovae naturally contain information about all of these processes and are at the centre of the entire scenario. Appropriate models of that phase can provide the missing link and improve our understanding of this field enormously.

The goal of this thesis is to advance new methods to calculate synthetic spectra in order to extract the information contained in the observations more efficiently. Based on a well established radiation transfer code, a new technique called *Abundance Tomography* is developed to derive the abundance distribution of Type Ia Supernovae ejecta. While previous approaches were limited to the determination of the abundances of specific species in restricted regions of the supernova envelope, here a complete stratified distribution of all major elements is obtained. This method is applied to the very well observed normal SN 2002bo. Combining the early spectra with those of the nebular phase leads to a coverage of the entire ejecta from the centre out to the highest velocities. The abundances derived are used to compute a synthetic bolometric light curve to test the radial distribution of Fe group and intermediate-mass elements.

The sampling procedure of the incident radiation field at the lower boundary is modified to obtain a better description of the real situation in Type Ia Supernovae. This improves the overall flux distribution significantly, especially in the red part of the spectrum, where almost no real line opacity is found. Synthetic spectra with this new procedure reproduce the observations much more accurately, as is shown by models of SN 2002er.

Hydrogen lines have never been detected convincingly in Type Ia Supernovae spectra. However, using spectra that were observed more than 10 days before maximum light, it is shown that small amounts of hydrogen in the outer parts of the ejecta can explain high velocity line absorptions, seen rather frequently

in various objects, e.g. SN 2002dj, SN 2003du, and SN 1999ee. The hydrogen is not claimed to be primordial to the white dwarf but it is rather the effect of the supernova ejecta interacting with circumstellar material, namely the white dwarf's accretion disk build up prior to the explosion.

Finally, UV spectra of Type Ia Supernovae are discussed. The ability of the Monte Carlo technique to deal naturally with this wavelength region is proven. Applications are presented by modelling spectra of SN 2001ep and SN 2001eh obtained with the Hubble Space Telescope.

The results are discussed in the broader context of Type Ia Supernovae physics: What causes the diversity in the nearby sample? What are the progenitors and how does the explosion work? What is the influence on cosmological models?

A detailed knowledge of the abundances, their distribution in the Supernova ejecta, and their ultimate causes delivers the key to these fundamental issues.

Zusammenfassung

Die Entdeckung der Dunklen Energie basiert nicht zuletzt auf der Interpretation von Beobachtungen weit entfernter bzw. hoch rotverschobener Supernovae vom Typ Ia ($z > 0.1$). Gleichwohl steht eine vollständige und konsistente Beschreibung des physikalischen Ablaufs thermonuklearer Explosionen, die dem Phänomen der Supernovae Ia zugrunde liegen, immer noch aus.

So konnte bislang der Zusammenhang zwischen den einzelnen Entwicklungsstufen – vom Vorläuferstern über die explosive Nukleosynthese bis hin zur Phase der homologen Expansion – und den Beobachtungen noch nicht hinreichend geklärt werden. Die Spektren aus der frühen Phase, d. h. einige Tage nach der Explosion, enthalten wichtige Informationen über diesen Ablauf; deren Interpretation steht damit im Zentrum der derzeitigen Supernova Ia Forschung. Geeignete Modelle zur Erzeugung synthetischer Spektren sind das notwendige Werkzeug, um wesentliche Details der thermonuklearen Explosion zu überprüfen und so eine Möglichkeit zur Quantifizierung der Dunklen Energie bereitzustellen.

Ziel dieser Arbeit ist es, mit Hilfe neuer Methoden zur Berechnung synthetischer Spektren die in den Beobachtungen enthaltenen Informationen zu extrahieren und zu analysieren. Den entscheidenden methodischen Schritt stellt dabei die Entwicklung der Tomographie der Elementhäufigkeiten dar. Als wesentlicher Fortschritt kann die Verteilung der Elemente in der Hülle der Supernovae detailliert untersucht werden. Bisherige Verfahren beschränkten sich hierbei lediglich auf die Bestimmung globaler Häufigkeiten spezieller Elemente, während die neue Methode eine vollständige Analyse der radialabhängigen Verteilung aller wichtigen Elemente zulässt. Die Ergebnisse einer ersten Anwendung werden für die Supernova 2002bo präsentiert. Dabei wurde die Spektralanalyse der frühen Phase mit den Ergebnissen der Nebelphase kombiniert, um so eine vollständige Bestimmung der Häufigkeiten – vom innersten Punkt der Hülle bis hin zu den höchsten Radialgeschwindigkeitswerten – zu erhalten. Im nächsten Schritt wurden die Ergebnisse der Häufigkeitsverteilung dazu verwendet, die bolometrische Lichtkurve zu berechnen. Durch den Vergleich mit der beobachteten Lichtkurve konnte so die geschichtete Verteilung der Eisengruppen- und mittelschweren Elemente präzise bestätigt werden.

Desweiteren wurde das Samplingverfahren zur Berechnung des Strahlungsfeldes im innersten Bereich erheblich verbessert und so modifiziert, dass es den bei Supernovae Ia vorherrschenden physikalischen Bedingungen besser

entspricht. Damit konnte die Strahlungsflussverteilung signifikant verbessert werden, was insbesondere im opazitätsarmen roten Bereich des Spektrums von entscheidender Bedeutung ist. Anhand von Modellen zur Supernova 2002er wird ferner gezeigt, dass die auf der neuen Methode basierenden synthetischen Spektren die Beobachtungen in wesentlichen Punkten, wie beispielsweise die dominanten Spektrallinien von S, Si, Ca und Fe, erheblich besser repräsentieren.

Ein weiterer für das Gesamtverständnis wichtiger Punkt bezieht sich auf die Frage nach der Wasserstoffhäufigkeit. Bislang konnten in Typ Ia Supernova Spektren keine Wasserstofflinien nachgewiesen werden. Anhand von Spektren, die mehr als 10 Tage vor dem Helligkeitsmaximum aufgenommen wurden, konnten wir jedoch zeigen, dass bislang ungeklärte Linienabsorptionen, hauptsächlich von Ca und Si, bei sehr hohen Geschwindigkeiten durch kleine Mengen Wasserstoff aus der Akkretionsscheibe erklärt werden können. Dieses Ergebnis birgt erhebliche Implikationen für das Verständnis der Supernova Ia Vorläufersterne.

Für die Diskussion der Ergebnisse in einem größeren astrophysikalischen Rahmen sind desweiteren folgende Fragestellungen relevant: Was verursacht bei den nahen Objekten das unterschiedliche Verhalten ihrer Lichtkurven? Woraus entstehen sie und wie läuft die Explosion im Detail ab? Welche Konsequenzen hat die präzise Parameterstudie von Supernovae Ia für die Kosmologie?

Wie in dieser Arbeit gezeigt wird, liefert die exakte Kenntnis der Häufigkeitsverteilung der Elemente in den Supernovae Ia Hüllen den Schlüssel zur Beantwortung dieser elementaren Fragen.

Contents

Abstract	ix
Zusammenfassung	xi
List of Figures	xvi
List of Tables	xvii
1. Introduction	1
1.1. The importance of Type Ia Supernovae	4
1.1.1. Astrophysical relevance	4
1.1.2. Type Ia Supernovae and cosmology	5
1.2. Objectives of this work	8
1.3. Organisation of the thesis	11
2. Observational and theoretical aspects of Type Ia Supernovae	13
2.1. Observational characteristics	13
2.1.1. Light curves and luminosity	13
2.1.2. Spectra	18
2.1.3. Supernova Ia rates	22
2.2. Progenitor scenarios	22
2.3. Explosion mechanism	26
3. Radiation transfer methods	29
3.1. The radiative transfer equation	29
3.2. Radiative transfer in SN ejecta	31
3.3. Numerical approaches to the problem	33
4. The Monte Carlo code	35
4.1. Model supernova envelope	35
4.1.1. Temperature stratification	36
4.1.2. Method of radiative transfer	37
4.1.3. Ionisation and excitation	38
4.2. Numerical technique	40

4.2.1. Input data	40
4.2.2. Line selection	41
4.2.3. Determination of the temperature structure	41
4.2.4. Radiative transfer	42
4.2.5. Emergent spectrum	46
4.3. The modelling procedure	50
5. Abundance Tomography of Type Ia Supernovae	51
5.1. Stratified abundances in supernovae	51
5.2. Abundance Tomography	53
5.3. Abundance Tomography: The case of SN 2002bo	55
5.3.1. Observations	56
5.3.2. Model of the early IR-spectrum at day -8.5	56
5.3.3. Is there carbon in SN 2002bo?	59
5.3.4. Spectral Analysis	61
5.3.5. Nebular phase	74
5.3.6. Abundance Tomography of SN 2002bo	76
5.3.7. Expansion velocities	81
5.3.8. Bolometric light curve	82
5.3.9. Conclusions	83
6. The incident radiation field	87
6.1. The flux distribution in the supernova envelope	87
6.2. The incident radiation field in the Monte Carlo procedure	88
6.3. Synthetic spectra of SN 2002er	90
6.3.1. Day -2.4	92
6.3.2. Day -11.3	94
6.4. Conclusion	95
7. Evidence for circumstellar interaction in Type Ia Supernovae	97
7.1. High velocity line features	97
7.1.1. SN 2003du	98
7.1.2. SN 2002dj	99
7.1.3. SN 1999ee	101
7.2. An abundance enhancement?	105
7.3. A density enhancement?	110
7.4. Circumstellar interaction?	112
7.5. Discussion	116
8. UV spectra of Type Ia Supernovae	119
8.1. The line blocking effect	119
8.2. Monte Carlo treatment of the UV	120
8.3. Models of UV spectra	121

8.3.1. SN 2001eh	121
8.3.2. SN 2001ep	124
8.4. Conclusion	126
9. Conclusions	129
9.1. Improvements to synthetic spectra calculations	129
9.2. Future prospects	132
Bibliography	133
Danksagung	149
Lebenslauf	151

List of Figures

1.1. SN 2002bo in NGC 3190.	2
1.2. Supernova taxonomy	3
1.3. SNe Ia confidence contours from all sources for Ω_M and Ω_Λ and the residual Hubble diagram of 172 SNe Ia	7
2.1. Light curves of different types of supernovae	14
2.2. Colour light curves of SN 2003cg	17
2.3. Representative spectra near maximum light of different types of supernovae	19
2.4. Comparison of the maximum light spectra of SNe Ia with different decline rates	21
2.5. Accreting white dwarf	24
2.6. Final fate of an accreting C+O WD depending on its initial mass M_{C+O} and the accretion rate \dot{M}	25
4.1. Random walk of a photon through the SN ejecta	43
4.2. Photon encounters line and scattering events during its flight through a model shell	45
5.1. Schematic plot of the concept of Abundance Tomography	54
5.2. Spectral evolution of SN 2002bo	57
5.3. Models for the near-infrared of SN 2002bo on day -8.5	60
5.4. Model of SN 2002bo on day -12.9	63
5.5. Models for SN 2002bo between day -12.0 and day -4.1	66
5.6. Models for SN 2002bo between day -3.9 and day $+5.9$	71
5.7. Models of nebular spectra for SN 2002bo	75
5.8. The abundance distribution in the ejecta of SN 2002bo	77
5.9. Expansion velocities in SN 2002bo	81
5.10. The uvoir light curve of SN 2002bo	83
6.1. Modified photospheric radiation field	90
6.2. Synthetic spectra of SN 2002er at day -2.4 , ($f = 0.0$ and $f = 0.5$, $\lambda_c = 6200 \text{ \AA}$)	93

6.3. Observed and synthetic spectrum of SN 2002er at day -11.3 , ($f = 0.5$, $\lambda_c = 6200 \text{ \AA}$)	95
7.1. Synthetic spectra of SN 2002dj at day -10.9	100
7.2. Decomposition of the absorption part of the Ca II IR triplet into three gaussian components in SN 1999ee	102
7.3. Time evolution of the observed velocity of the Ca II IR triplet components, the Si II 6355 \AA line, and the photospheric velocity adopted in model calculations for SN 1999ee.	103
7.4. Synthetic spectral sequence of SN 1999ee using W7 densities and abundances	104
7.5. Synthetic spectra of SN 2003du at day -11.5 using normal W7 density and flat density profile with Hydrogen	106
7.6. Model for the Oct. 9 of SN 1999ee spectrum with increased abundances of Si, Ca, and increased optical depth of Fe II lines	108
7.7. Synthetic spectral series for SN 1999ee using the abundance distribution	109
7.8. Model for the Oct. 9 SN 1999ee spectrum with increased density at high velocity	111
7.9. Synthetic spectral series for SN 1999ee using the increased density	112
7.10. Synthetic spectrum of SN 2002dj at day -10.9 using flat density profile and a $0.04 M_{\odot}$ Hydrogen outer shell	114
7.11. The effect of H on the Ca II H&K doublet and Ca II IR triplet in SN 2002dj	115
7.12. Model for the Oct. 9 SN 1999ee spectrum using the increased density and an outer $0.004 M_{\odot}$ of Hydrogen	117
8.1. Synthetic spectra of SN 2001eh at day $+10$ showing the effect of Titanium on the UV	123
8.2. Synthetic spectra of SN 2001ep at day $+10$ showing the influence of Titanium on the UV	126

List of Tables

5.1. Spectroscopic observations of SN 2002bo	58
5.2. Main parameter values of SN 2002bo and its host galaxy	59
5.3. Input parameters and converged T_{BB} for SN 2002bo models	62
5.4. Total mass of elements in the ejecta of SN 2002bo spectroscopically confirmed by the Abundance Tomography and nucleosynthesis products of different SN Ia explosion models	78
6.1. Main parameters of SN 2002er and its host galaxy	91
8.1. Abundances of SN 2001eh	122
8.2. Abundances of SN 2001ep	125

1. Introduction

*... He saw; and blasted with excess of light,
Closed his eyes in endless night.*

*Thomas Gray (1716-1771),
The Progress of Poesy*

Many people all around the globe witnessed the enormous afterglows of cosmic explosions for millennia, always speculating about their origin and nature. Since these transient phenomena in the night sky or sometimes even during daylight were thought to be new stars, they were called novae or supernovae. Although the observations of “new stars” in ancient times were only made with the naked eye, some of these measurements provide astonishing accuracy, which sometimes even allow to reconstruct their light curves (Stephenson & Green 2002, Green & Stephenson 2003). The modern era in European astronomy began with systematic observations of two supernovae, by Tycho Brahe in 1572 (Brahe 1573) and Johannes Kepler in 1604. However, it took almost another 300 years until serious supernova research began. On August 31, 1885, Hartwig discovered a “nova” near the center of the Andromeda galaxy, which became invisible about 18 months later. When Lundmark estimated the distance to M31 to be about 7×10^5 lyrs in 1919, it became obvious that Hartwig’s nova had been several 1000 times brighter than a normal nova (Lundmark 1920). With the introduction of the term *supernova* by Baade & Zwicky (1934) a clear distinction to classical novae was made. Indeed, supernovae are one of the most powerful events in the Universe. Their luminosity raises to a maximum of up to $10^{42} - 10^{43}$ erg s⁻¹ within ~ 3 weeks, equivalent to the luminosity of an entire galaxy.

By that time, with only a handful of observations available, all events showed little dispersion in their maximum luminosity and consequently Wilson (1939) and Zwicky (1939) suggested that supernovae (SNe) could be used as distance indicators. Only a few months later Minkowski realised that there exist at least two types of SNe, differing in their spectral features (Minkowski 1941). He called



Figure 1.1.: SN 2002bo in NGC 3190.

them type I if they do not exhibit Balmer lines of hydrogen near maximum light and type II if they do so. Still, it was not clear, whether these objects have the same origin or the spectral distinction reflects different physical mechanisms to explain their nature. It took until 1960, when Hoyle & Fowler (1960) suggested that thermonuclear burning in an electron-degenerate stellar core may explain its explosion, finally leading to the complete disruption of the star. This scenario was completed with the idea of Truran et al. (1967) and Colgate & McKee (1969), who proposed the light curves to be powered by the radioactive decay of ^{56}Ni , which is synthesised in the explosion. Finally, the strict allocation to the various subclasses of type I SNe was made years later by Wheeler & Harkness (1990).

The classification of SNe was originally completely based on spectroscopic differences but soon it became clear that the spectroscopically distinct varieties are correlated with the origin and the explosion mechanism of the various classes.

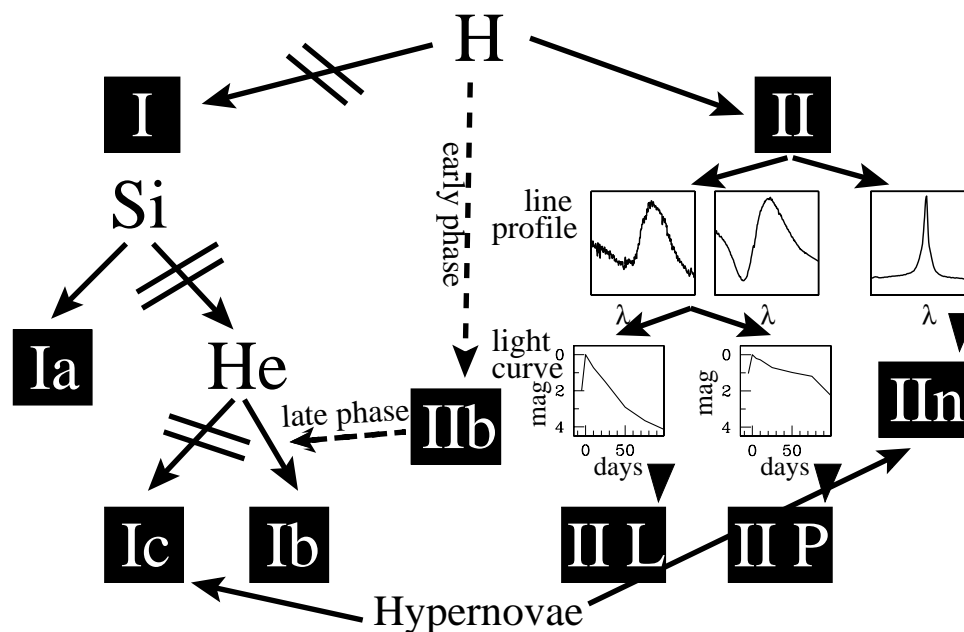


Figure 1.2.: Supernova taxonomy (Cappellaro & Turatto 2001).

Indeed, the strong P Cygni line of Si II near 6100 \AA , which is only seen in type Ia events, is a typical sign of a thermonuclear explosion, because Si is the main element in the fusion reactions to ^{56}Ni and indicates thermonuclear carbon burning. Nowadays, it is widely agreed that type Ia supernovae (SNe Ia) result from the thermonuclear disruption of a white dwarf composed of carbon and oxygen (C+O WD). Whether the WD is a single star or member of a binary system as well as the nature of the possible binary companion is still uncertain.

Figure 1.2 shows the supernova taxonomy with the main criteria to distinguish them. If strong H lines are detected in the spectrum of a SN, the progenitor must have had an extended H envelope which is not affected by the burning. These objects are called *type II SNe*. Type II SNe originate from the gravitational collapse of the core of massive stars. The thermal pressure is insufficient to stabilise the gravitational collapse after the thermonuclear burning of the core has ceased and therefore a heavy compact object, namely a neutron star or even a black hole, is formed. Different subclasses of type II supernovae were defined to account for their diversity in spectra and light curves.

By far not all type I events are thermonuclear explosion but there are additional subclasses of type I SNe that show neither H lines nor Si lines. These objects are

classified as *type Ib SNe* if they exhibit strong He I lines and *type Ic* if there are neither Si nor He lines around maximum light. Both classes can be explained as core collapse SNe like the type II but having their H envelopes and – in the case of the type Ic SNe – also most of their He envelopes stripped by strong stellar winds or binary interaction prior to the explosion (Nomoto et al. 1995).

Within the last two decades great efforts have been made to improve our knowledge of all types of supernovae. Originally only few observational programmes (e.g. Zwicky 1965) were undertaken, detecting about a dozen supernovae each year. The big turn in this field came with the discovery of SN 1987A and the following emergence of deep coordinated searches for distant supernovae. Recently, research on core collapse supernovae is boosted. Several very high energetic SNe Ic, sometimes called “*Hypernovae*”, were observed and there is strong evidence, that these objects are connected to Gamma Ray Bursts (GRBs), the most powerful sources in our known Universe. Thermonuclear supernovae are of special interest primarily caused by their ability to serve as distance indicators and their implications for cosmology. This work concentrates on the physics of SNe Ia and the methods at hand to improve our still limited understanding of these fascinating and important astrophysical objects.

1.1. The importance of Type Ia Supernovae

The interest in understanding the physics of SNe Ia has risen tremendously in the last decade. Several reasons are responsible for the boom in this field. First of all, SNe Ia are exciting objects on their own and there is great scientific concern to unravel their physical properties. Although there has been enormous progress in the understanding of these objects, there are still many uncertainties concerning the mechanism of SNe Ia. There are ideas and models for every stage of the evolution. However, a consistent and complete picture including the progenitor scenario, the explosion, and the post-explosion time is still missing.

1.1.1. Astrophysical relevance

SNe Ia cannot be understood without taking into account that they interact with their environment. They are the main producers of iron in the Universe. SNe Ia progenitors have relatively long life times compared to massive stars, which

are the progenitors of core collapse SNe, the other main contributor to the metal abundances in galaxies. Therefore, they serve as a clock for the metal enrichment of matter. This fact can be used to determine the relative metal abundances of α -elements and iron-group elements (Renzini 1999).

Independent of the details of the progenitor scenario (Sect. 2.2), it is widely agreed that SNe Ia originate from the disruption of a degenerate carbon-oxygen white dwarf in a binary system. Therefore, SNe Ia are the end of one of the major channels of stellar evolution. Although only a few white dwarfs really explode as SNe Ia, it is still possible to derive important information about the fraction and the evolution of binary systems, both in the Milky Way (e.g. Iben & Tutukov 1994, 1999) and with “look-back time”, i.e. the time that a light signal would require to travel from the galaxy in question to the Earth (e.g. Ruiz-Lapuente & Canal 1998).

SNe Ia also play a key role in the evolution of early type galaxies, they are responsible for the mass loss of galaxies (e.g. Burkert & Ruiz-Lapuente 1997, Ferrara & Tolstoy 2000), and contribute significantly to the regulation of star formation processes and the chemical evolution of galaxies (e.g. Chiappini et al. 2003).

1.1.2. Type Ia Supernovae and cosmology

In the past five years the SN Ia field has attracted enormous attention due to the application of SNe Ia to cosmology, suggesting that the expansion of the Universe is accelerated.

Although the luminosities of very nearby, well-observed objects span a range of more than a factor of ten, there are empirical correlations among them. To be more specific, their peak-luminosity is linked to distance-independent properties such as the light curve shape. Therefore, they can be calibrated as distance indicators, as is done for classical Cepheids. The two large and homogenous data samples of multifilter light curves of the Calán/Tololo search (Hamuy et al. 1996) and of the Center for Astrophysics (CFA) (Riess et al. 1999b) were essential to carry out this kind of analysis for the very first time. The nearby SNe of these samples were used to determine the corrections for the light curve shape and to fix the model lines in the Hubble diagram.

The surprising and revolutionary result of the application to the high- z SNe is that the distant SNe Ia appear fainter than their local counterparts. This statement ignited a heated and animated discussion, that is still continuing, because the impact on cosmology is enormous. Even for a Friedmann universe, i.e. models with a homogenous and isotropic metric (Robertson-Walker metric), that is completely empty, the SNe at high redshift seem to be too dim. The only explanation in a cosmological framework is the idea of an accelerated expanding universe. In order to account for the expansion a positive cosmological constant Λ (or a “dark energy” with negative pressure) is introduced. The faintness of the distant SNe suggests that the Universe started with the acceleration of the expansion, when the Universe was at about half of its present age. Tonry et al. (2003) derived latest results of the confidence contours from SNe Ia for the fractional matter energy density over the closure density[†] Ω_M and the fractional dark energy density over the closure density Ω_Λ (Fig. 1.3a). The results from the cosmic microwave background (CMB) anisotropy (e.g. results from the Wilkinson Microwave Anisotropy Probe (WMAP) observations; Spergel et al. 2003) and the estimates of the mass density from cluster evolution, mass-to-light ratios of clusters, and large scale structures (e.g. the Two Degree Field (2dF) Redshift Survey; Percival et al. 2002) are consistent with the SNe Ia data. Combining all results gives $\Omega_M = 0.3$ and $\Omega_\Lambda = 0.7$ as the most recent values. Owing to the accelerated expansion, the Universe is older than it was expected to be. This solves the long lasting inconsistency in standard cosmology between the age of the Universe and the oldest globular cluster stars.

Although using different methods for the corrections and based on different data sets, this result was established independently by two different groups, the Supernovae Cosmology Project (SCP) (Perlmutter et al. 1999) and the High- z Supernova Search Team (Riess et al. 1998). Recent results by Tonry et al. (2003) confirm the earlier analyses and substantiate the implications to cosmology and the fate of our Universe. Figure 1.3b shows the Hubble diagram (distance modulus vs. redshift) for 172 SNe Ia discovered and observed by the High- z Supernova Search Team (Tonry et al. 2003) normalised to an empty universe ($\Omega_M = 0, \Omega_\Lambda = 0$). The highlighted points correspond to median values in eight redshift bins.

[†]The closure density ρ_c is the density for a flat universe.

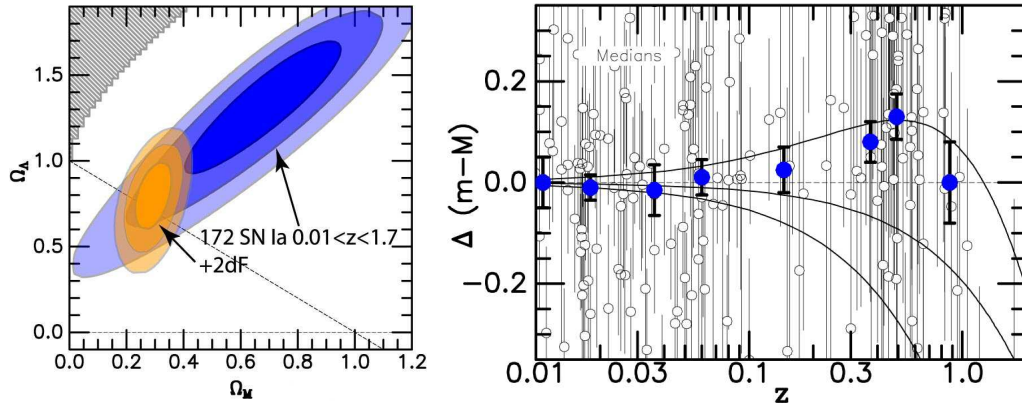


Figure 1.3.: a) SNe Ia confidence contours from all sources for Ω_M and Ω_Λ . Blue contours show 68,95 and 99.7% confidence intervals. Overlaid in orange are SNe Ia + 2dF (Percival et al. 2002) contours. b) The residual Hubble diagram (relative to an empty universe) of 172 SNe Ia. For better visual clarity, the blue points represent the binned median values of distances.

From top to bottom the curves show a flat universe $(\Omega_M, \Omega_\Lambda) = (0.3, 0.7)$, an open universe $(0.3, 0.0)$, and an Einstein-de Sitter model $(1.0, 0.0)$, respectively. One can clearly see that the first alternative model is favoured. However, to draw a final conclusion the statistical and especially the systematic errors have to be reduced.

Leibundgut (2001) discusses several alternative explanations for the dimming of distant SNe Ia. It can be speculated that the faintness may be due to absorption by “grey dust”, attenuation by gravitational lensing or evolutionary effects like the dependence of the explosion on different metallicity of the progenitor system. None of these explanations can be ruled out completely, but a strong argument against them is the fact that SNe Ia seem to become brighter again beyond a redshift of ~ 1 , which gives evidence of a past deceleration (Riess et al. 2004). All the above possibilities should dim the SNe more the further away they are.

Even if all of these concerns were obsolete, it should be noted that the correlation between the light curve shape and the peak luminosity that is used to calibrate the sample, is of pure phenomenological nature. These arguments call attention to the importance of a profound theoretical understanding of the physics behind SN Ia explosions.

1.2. Objectives of this work

The complexity and the variety of the SNe Ia issue makes it very hard to construct a consistent picture of the whole problem. In order to achieve a complete description, at least all of the following topics have to be addressed and taken into account: (1) Stellar evolution calculations to evolve and set up the progenitor system in the pre-supernova stage; (2) Hydrodynamics, non-explosive nuclear reactions, and kinematics of stellar systems to prepare the conditions that lead to the ignition of the star; (3) Hydrodynamics and explosive nucleosynthesis to describe the propagation of the flame and the disruption of the star; (4) Radiation/hydrodynamics calculations during the expansion of the stellar envelope; (5) γ -ray transport and radiative transfer calculations in order to extract spectra and light curves, that can finally be compared to the observations.

Although the importance of the results and the conclusions stated in Section 1.1.2 cannot be overemphasised, it is inevitable to remark that they fundamentally depend on the assumption that the properties of the nearby SNe Ia are exactly the same as for the distant ones. Therefore, after some years of extensive hunts for high- z SNe, more and more people realise that it is at least equally important to understand fully the physics of nearby SNe before firm conclusions about cosmology can be drawn. A big international collaboration called the *SN-Factory* (Aldering et al. 2002), which was launched in 2001 and taking data since March, 2004, became aware of this and consequently plans to discover and observe more than 300 SNe Ia at the low-redshift end of the smooth Hubble flow in the next few years. Its main goal is to increase the statistics of these measurements and thus to minimise the error in order to determine the cosmological parameters more accurately. Already in 2002 the European Supernova Collaboration (ESC), funded by the European Union as a Research Training Network (RTN), started to observe very nearby SNe Ia using a slightly different approach. We focus on much fewer objects (~ 5 SNe/year), but aim at achieving precise and extensive data of each object both spectroscopically and photometrically. Moreover, it is not enough to collect as much data as possible, but it is essential to catch the objects shortly after they have exploded. The motivation behind this approach is to study individual objects in detail in order to extract their exact properties and finally to reach a deeper insight into the complete evolution of such an event from the progenitor until a few years after the explosion. Based

on this knowledge, it should be possible to explain at least part of the diversity of SNe Ia. Recent results, partially presented in this work, confirm that this hope is justified.

Spectral analysis plays a key role in this game. Even though significant progress has been made in recent years, many of the properties of SNe Ia remain largely uncertain. There is a need for understanding both the processes and physical properties of SNe Ia in general and the peculiarities and special properties of individual objects. It is crucial to link theories of progenitor systems, numerical models of the explosion, and the observations. This link is provided by spectra of the early or so called photospheric epoch, i.e. the phase between the explosion and a few days after maximum light. Appropriate models of these spectra not only allow us to derive information about the physical properties of the SN ejecta such as temperature, chemical composition, etc., but they also can be used to verify observational based estimates of parameters such as reddening, distance, and epoch. In this phase the spectra are in fact very sensitive to small changes in these parameters. Even a slight increase in e.g. luminosity can strongly affect the temperature structure and therefore the ionisation of the various elements contained in the ejecta. This in turn influences line profiles and line ratios affecting the emergent spectrum. Additionally, these models serve as a powerful tool to test the results of numerical models of the explosion.

In particular very early observations, covering the first week after the explosion, are of great importance in this context. At these epochs the ejecta at velocities $\gtrsim 18,000 \text{ km s}^{-1}$ are dense enough to produce spectral lines. Therefore it is possible to derive information about the material at the surface of the WD. It may also be possible to detect signatures of an interaction between the SN ejecta and the circumstellar gas or winds from the WD or the companion star, thus shedding light on the progenitor system's properties. Clearly these observations are very hard to come by, since they can only be obtained if the supernova is discovered very early on when it is still quite dim.

Together with synthetic spectra of the nebular or late phase (months to years after the explosion) and models of light curves, one can connect theory and observations and therefore prove physical models that cannot be measured directly.

If we want to know about the properties of the progenitor, the explosion, and the post-explosion phase, we are limited by the fact that these objects can only be observed at best a couple of days after the star was disrupted. The events

happen too far away from us to resolve them and they are unpredictable both with respect to their location and their date so that we do not know where we should point our instruments. Therefore, there is no way to obtain immediate information about the event and we have to restrict ourselves to the radiation that escapes the SN ejecta little by little, finally arriving at the Earth.

There are two different ways to face the challenge. The first possibility is to calculate the whole process from first principles. In this case numerical calculations of the hydrodynamics and the explosive nucleosynthesis are carried out. The number of free parameters is reduced to a minimum, ideally they are even eliminated. The hydrodynamics deliver the density profile of the expanding envelope and the kinetic energy. The nucleosynthesis calculations determine the chemical distribution and therefore, indirectly via the amount of ^{56}Ni that is produced, the energy that is converted into radiation. With such an input model at hand, the energy deposition by γ -rays and the radiation transport in the ejecta can in principle be calculated consistently, and the emergent spectrum can be compared with the observations. Although there are even 3-dimensional explosion models available (e.g. Röpke & Hillebrandt 2004a, Gamezo et al. 2004), the bottleneck is the radiation transport. In order to solve the radiation transfer equation from first principles only, it is necessary to use full non-LTE (Local Thermal Equilibrium) physical conditions. This makes the calculation extremely expensive in computation time. Several groups developed such codes or the development is in progress, but none of these attempts has been successful in either constraining the explosion models or in reproducing the observations meaningfully (Eastman & Pinto 1993, Höflich 1995, Pauldrach et al. 1996, Hauschildt & Baron 1999).

A somewhat different approach is to neglect some physical aspects of minor importance at the expense of overall consistency. This consequently leads to the introduction of free parameters and assumptions into the radiation transport calculation. This method may sound unsatisfactory at a first glance, but it has enormous advantages compared to the previous approach. The code becomes more manageable and most notably very fast. Still the density profiles and the abundance distribution of the explosion models can enter the radiation transport calculation directly and without modifications, and therefore be tested. Moreover, being aware of the limitations and the basic assumptions, this method serves as an efficient and powerful tool to further our knowledge about SNe Ia.

In this work a Monte Carlo procedure to calculate synthetic spectra of SNe Ia in their early phase is presented. A new method called “*Abundance Tomography*” to derive the detailed abundance distribution of the SN ejecta is investigated, implemented into the MC code, and applied to several well observed objects. The so called “black body assumption”, used as the incident radiation field in the code, is improved and tested. Finally, from the spectral analyses conclusions are drawn to further constrain different explosion models, possible interaction of the SNe with their environment, and the properties of UV spectra of SNe Ia.

1.3. Organisation of the thesis

This work is organised as follows: After the general introduction, an overview of the various aspects of SNe Ia is given in Chapter 2. This includes observational facts, such as light curves (Sect. 2.1.1), spectra (Sect. 2.1.2), and SN rates (Sect. 2.1.3), as well as more theoretical topics, including the state of the art in the understanding of the progenitors of SNe Ia in Section 2.2, and a brief overview of the different explosion models in Section 2.3.

In Chapter 3, different methods for spectral synthesis are discussed. Section 3.1 deals with the general physics of the radiation transport, while Section 3.2 explains the characteristics of the radiation transport in SNe. Different numerical approaches to this problem are discussed in Section 3.3.

The Monte Carlo code used in this work to calculate the radiation transport in SNe ejecta, is presented and discussed in Chapter 4. The basic concept and the setup of the model SN envelope are given in Section 4.1, followed by a detailed description of the numerical technique in Section 4.2. The modelling procedure is explained in Section 4.3.

One of the main purposes of this work is to introduce a new method in spectral analysis of SNe Ia. This is called “*Abundance Tomography*” and is explained in Chapter 5. The method itself and its implementation in the Monte Carlo code are discussed in Section 5.1 and 5.2. Section 5.3 describes the application of the method to SN 2002bo, and includes a complete analysis of this object.

Chapter 6 addresses a long standing shortcoming of the code, namely the correct description of the flux in the red part of the spectra. A solution of this problem is presented in Section 6.2. Section 6.3 contains synthetic spectra of

SN 2002er that are calculated with the modified code.

Circumstellar interaction of SNe Ia is a very interesting topic, especially because up to now there are very little reliable information available. Chapter 7 explains how spectral analyses can contribute to this field. We discuss and analyse high-velocity components seen in several SNe Ia in Section 7.1. Possible explanations for this phenomenon are given in Section 7.2, 7.3, and 7.4.

In Chapter 8 the UV spectra of SNe Ia are discussed. We discuss the line blocking effect in SNe Ia envelopes (Sect. 8.1) and explain the UV treatment of our MC code (Sect. 8.2). The spectral analysis of two objects observed in the UV bands with the Hubble Space Telescope (HST) are presented in Section 8.3.

Finally, an overall discussion of this work is given and possible directions and objectives for further work are described.

2. Observational and theoretical aspects of Type Ia Supernovae

This chapter gives an overview of the observational and theoretical aspects of SNe Ia. Since spectra are a crucial link between theory and observations, it is appropriate to discuss the related topics and their impact on spectral analysis. A brief introduction to the various topics of light curves, spectra, SN Ia rates, progenitors, and explosion models is presented.

2.1. Observational characteristics

A significant fraction of SNe Ia can be grouped due to their remarkable homogeneity in their light curves, spectra, and absolute magnitudes. This main bulk of objects is widely called “Branch normal” SNe Ia. Branch et al. (1993) were the first to classify a large sample of SNe Ia into a “normal” class and different groups of “peculiar” objects. The peculiar groups consist of the over-luminous SNe (“SN 1991T-like”) and the sub-luminous ones (“SN 1991bg-like”). The rate for the peculiar objects was estimated by Branch et al. (1993) to be $\sim 15\%$, but more recent observations indicate a higher value up to 30% (Li et al. 2000).

2.1.1. Light curves and luminosity

Photometry is a basic method to obtain data from SNe. The light curves derived from photometric measurements are therefore a very important source of information about all kinds of SNe. Not only the energy input from the explosion and the radiation escaping from the expanding envelope, but also information about the environment and the progenitor of the SN as well as interaction with circumstellar dust or clouds enter the light curves and influence their shape. Light curves are taken in several filter passbands. This increases complexity,

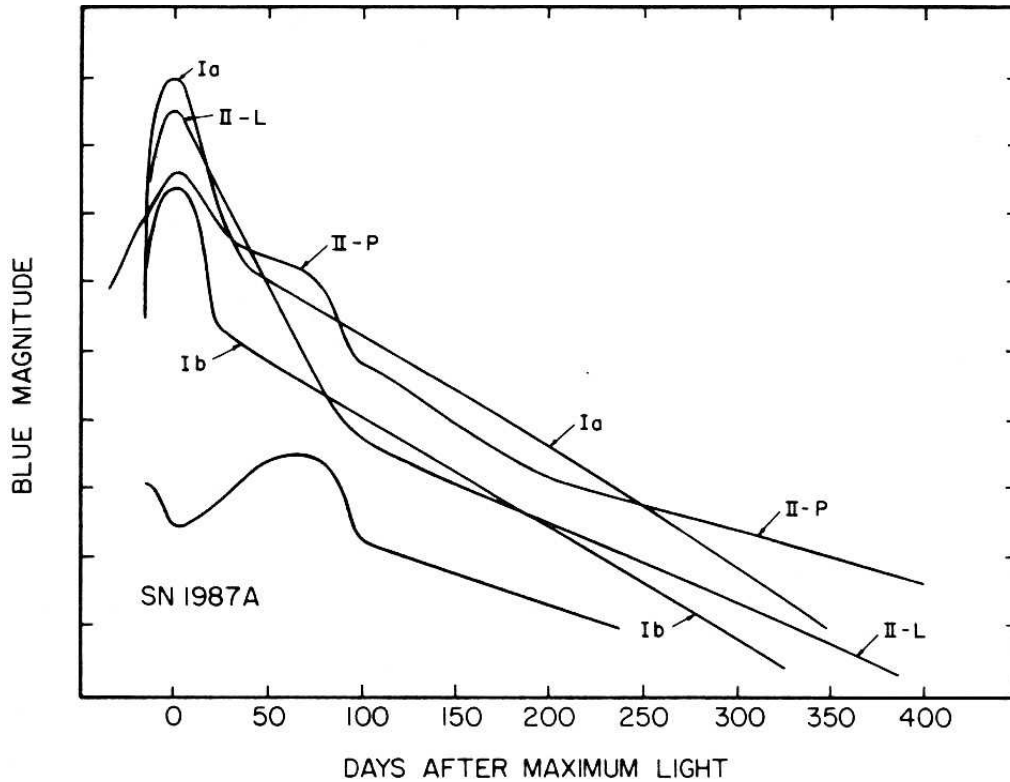


Figure 2.1.: Light curves of different types of supernovae (Wheeler et al. 1990).

but also the amount of information, because radiation from the various filters interacts differently with the environment.

The common property of all light curves is their power source. The main product of burning to nuclear statistical equilibrium (NSE) during the explosion is ^{56}Ni . With a half-life of 6.1 days ^{56}Ni decays because of electron capture to unstable ^{56}Co producing γ -rays. The ^{56}Co itself decays to stable ^{56}Fe through either electron capture (81%) or β -decay (19%) with a half-life of 77.1 days. The positrons from the β -decay channel annihilate to γ -rays. The γ -rays from both decays (^{56}Ni and ^{56}Co) are thermalised and escape the ejecta as optical or infrared photons. Since the SN envelope is mostly opaque at very early times these photons are trapped and cannot escape immediately. As the ejecta transparency increases, more and more photons are released and the light curve rises rapidly. According to Arnett law a phase is reached in which the released energy is balanced by the energy input from the radioactive decay. This is the maximum light

phase. Since the opacities are strongly wavelength dependent, the maximum occurs at different times in the various passbands. As the opacities drop further the reservoir of trapped photons empties out, and the lightcurve declines. Although there is a large dispersion in the post-maximum decline rates, a decrease of 1 ~ 3 mag is found for all types. In the late phase (several weeks after maximum light) the shape of the light curves resembles the exponential decrease of the ^{56}Co decay, because during this phase the ejecta is so diffuse that no more photons can be trapped. The γ -rays from the electron capture channel and from the β -decay channel then thermalise, and thus they make the ejecta shine. In the late times this is mostly through forbidden line emission.

A large number of factors influence the light curves and are responsible for their diversity. Figure 2.1 shows the light curves of different kinds of SNe. Since core collapse SNe occur in many different configurations, and their progenitor stars are restricted to be heavier than $\sim 8 M_{\odot}$, their intrinsic variations are very large. Especially those SNe whose H envelope has not been stripped at the time of the explosion, show a large variety in their light curves. Nevertheless, the early-time light curves ($t \lesssim 100$ days) can be grouped into two main classes, namely the SNe II-P and the SNe II-L. The abbreviations are for “plateau” and “linear”, respectively. The SNe II-L light curves generally resemble those of SNe I, whereas light curves of SNe II-P remain within ~ 1 mag of maximum brightness for an extended period. The absolute magnitude at peak brightness of the SNe II-P varies remarkably (Schmitz & Gaskell 1988) caused mostly by different radii of the progenitor stars. On the other hand, most SNe II-L have a nearly uniform peak absolute magnitude (Young & Branch 1989) which is about ~ 2.5 mag fainter than SNe Ia. At late times ($t \gtrsim 150$ days) most SN light curves look very similar both in shape and absolute flux (Patat et al. 1994). The type Ib/c events show light curves that are not very different from those of SNe Ia (see below). However, they are by far less homogenous with respect to their shape as well as their peak luminosity.

Until the 1990s all light curves of SNe Ia were thought to be the same. With better instruments and therefore a better signal-to-noise ratio and with a large number of objects observed, it became clear that there are differences. Better observations also allowed more accurate measurements. It was found that the maximum brightness of a SN Ia correlates with the decline rate of the light curve (Phillips 1993, Hamuy et al. 1996). The decline rate can be parametrised with

$\Delta m_{15}(B)$, which is the difference in magnitudes of the B band filter between maximum light and the luminosity 15 days after peak. The brighter SNe Ia have broader light curves and decline more slowly, thus having a smaller $\Delta m_{15}(B)$ than fainter objects, which show a narrower slope with larger values of $\Delta m_{15}(B)$. With this correlation it is possible to calibrate the light curves and to use SNe Ia as cosmological distance indicators (Sect. 1.1.2). The most plausible explanation for the relation between brightness and decline rate is the difference in the ^{56}Ni mass (Mazzali et al. 2001a). From analytical studies of the peak properties of a SN Ia light curve (Arnett 1982, 1996) it can be seen that:

1. The brightness of the light curve at maximum is proportional to the mass of synthesised ^{56}Ni (Arnett law).
2. The width of the light curve τ_{LC} depends on the ejected mass M_{ej} , the kinetic energy of the explosion E_K , and the gray opacity to optical photons κ_{opt} as follows:

$$\tau_{LC} \propto \kappa_{opt}^{1/2} M_{ej}^{3/4} E_K^{-1/4}. \quad (2.1)$$

It is observationally confirmed that SNe Ia produce different amounts of ^{56}Ni . The Branch-normal SNe Ia synthesise roughly $0.5 M_{\odot}$ with some dispersion (Nugent et al. 1995b), but extreme cases range from $0.1 M_{\odot}$ for SN 1991bg (Filippenko et al. 1992) to about $1 M_{\odot}$ for SN 1991T (Spyromilio et al. 1992), which is shown in Fig. 2.4. In principle all three quantities κ_{opt} , M_{ej} , and E_K could possibly explain the dispersion. The right panel in Fig. 2.4 suggests different M_{ej} to be responsible. This means that sub-Chandrasekhar and even super-Chandrasekhar explosions (Sect. 2.2) would be very common, which is in contradiction to the most favoured progenitor model (Sect. 2.2). Assuming that the initial mass is more or less the same for all SNe Ia explosions, the kinetic energy can also not account for the large diversity. Hence, we are left with the optical opacity. In SNe Ia, κ_{opt} depends mainly on line not continuum opacity. Line opacity is determined by low-ionisation species with a large number of active lines. Since low excitation ions of Fe group elements have many more lines (about a factor of 10) than low-excitation ions of intermediate-mass elements (IME), we can expect that the average opacity is higher in regions where Fe group elements dominate. Moreover, we can conclude that SNe Ia with a higher $^{56}\text{Ni}/\text{IME}$ production ratio also have a higher opacity, and therefore a broader light curve.

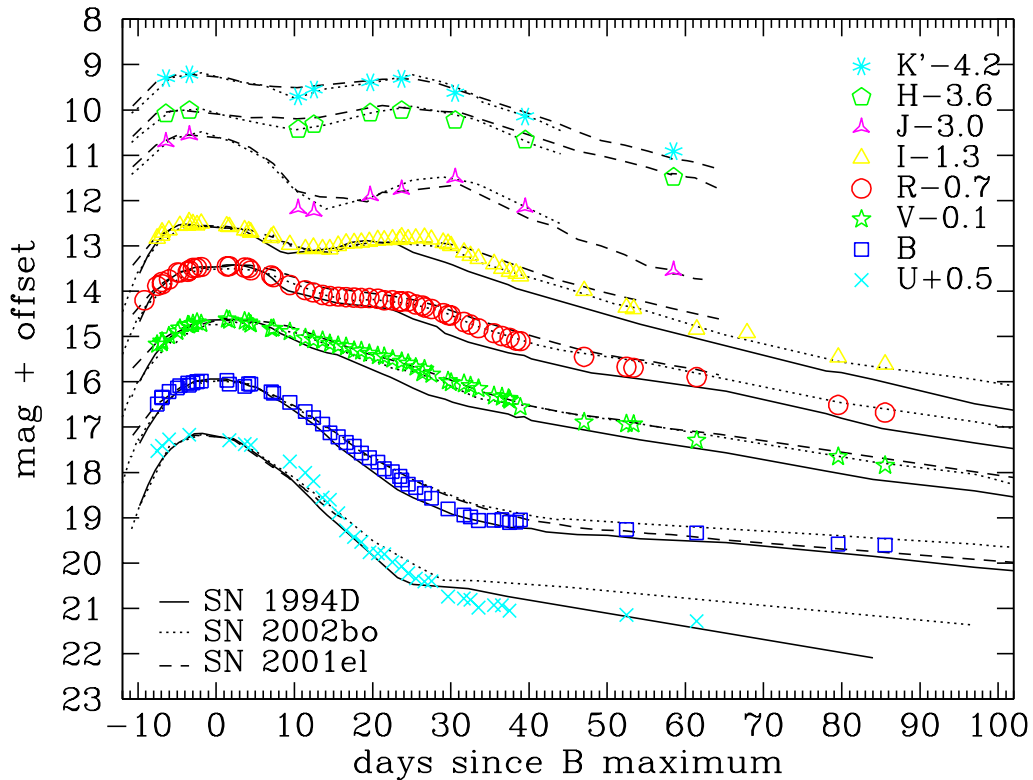


Figure 2.2.: Colour light curves of SN 2003cg compared to the ‘normal’ SNe Ia SN 1994D, SN 2002bo, and SN 2001el (Elias-Rosa et al. 2004, in prep.).

Recent summaries of SNe Ia light curves can be found in Leibundgut (2000) and Meikle (2000, for the infrared light curves). We give a brief introduction to this topic. SNe Ia light curves are characterised by a fast rise, on a timescale of about 20 days. Riess et al. (1999a) suggest an average rise time of 19.5 d. Therefore it is challenging to catch them long before peak brightness and only very few objects have been observed before day -14 (relative to B maximum). One of the major goals in the campaigns of the ESC is to observe SNe Ia as early as possible, since the early epochs contain the most important information about the progenitor and the explosion mechanism. The maximum phase begins at about 5 days before peak luminosity when the light curve becomes noticeably flatter. The maximum is reached first at near-infrared (NIR) wavelengths (Contardo et al. 2000, Meikle 2000) followed by the optical maximum a few days later. While the blue light curves decrease monotonically after their maximum, the NIR bands I , J , H , and K show a prominent secondary maximum after about

20 days (Elias et al. 1981, Meikle 2000). This behaviour can also be seen in the NIR light curves of the ESC SNe (Fig. 2.2). Only the peculiar faint objects like SN 1991bg lack these secondary maxima. The delay of the NIR maxima with respect to the optical ones causes a significant change in colour towards the red. Although it is very difficult to achieve accurate measurements of this effect, the colour shift is often used to determine the reddening towards the object, since the intrinsic colours of SNe Ia seem to be rather uniform (Phillips et al. 1999).

Most of the emerging radiation is emitted in the optical and NIR wavebands, while the UV part is largely optically thick. Indeed the V band light curve is usually very similar to the combined bolometric light curve, especially after maximum. Thus pseudo-bolometric light curves – the combination of $UBVRIJHK$ filter passbands – contain up to 80% of all energy that is emitted outside the γ -ray region. They can provide important insights into the complicated processes of the hydrodynamics and the radiation transport in the SN ejecta. SNe Ia reach a maximum absolute brightness of $M_B \approx M_V \approx -19.3$ mag (Riess et al. 1999b) and a bolometric luminosity of $\log L_{bol} \approx 10^{43}$ erg s $^{-1}$ (Contardo et al. 2000). Additionally, bolometric light curves deliver a good estimate for the total amount of radioactive nuclei that are produced in the explosion and stored in the ejecta.

2.1.2. Spectra

Classes of SNe are defined by the different spectral features of the objects. As already mentioned in Chapter 1 the major criterion for distinction is the appearance or absence of H lines. Usually, the classification is done at a time near maximum light. But also at very early epochs or in the nebular phase, each species of SNe shows typical line features, except for some peculiar objects especially among the type I SNe. Despite these peculiarities of some objects, it was tried to perform a standard spectral sequence SNe Ia. This shows a “first-order” homogeneity in the spectral evolution as it is seen in the light curve shapes (Canarias Type Ia Supernova Archive, Gómez & López 1998). The homogeneity is much less pronounced in spectra and it is sometimes difficult to separate peculiar SNe Ia from other classes, e.g. SN 2002cx (Li et al. 2003) or SN 2002ic (Wang et al. 2004, Kotak et al. 2004). We give a more general overview of spectral properties of all kinds of SNe with emphasis on SNe Ia. Details of the spectral features are discussed in the analysis parts (Sect. 5.3, 6.3, 7.1, 8.3.1, and 8.3.2).

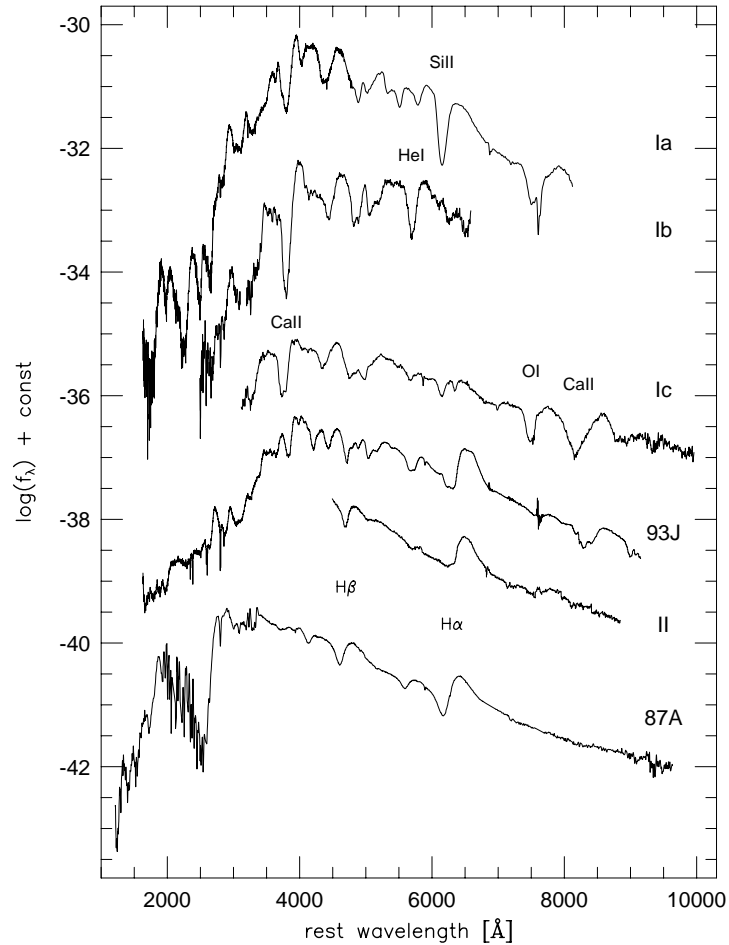


Figure 2.3.: Representative spectra near maximum light of different types of supernovae (Wheeler & Benetti 2000).

A more detailed review of optical spectra of SNe can be found in Filippenko (1997), infrared spectra are discussed in Garnavich (1995) as well as in Marion et al. (2003), but concentrated on NIR spectra of SNe Ia.

Looking at snapshots of spectra at various epochs, all SNe I have broad lines at early epochs that indicate high expansion velocities and high kinetic energy. The lines typically show prominent P-Cygni profiles due to resonant scattering above the photosphere (Fig. 2.3). Photons that are absorbed or emitted directly in the line of sight of the observer are registered at bluer wavelengths relative to their rest wavelength. Whereas photons that are radiated by an atom escaping perpendicular to this line reach the telescope at their rest wavelength.

The striking spectral feature of SNe Ia is their deep absorption trough near 6350 Å attributed to Si II at 6347, 6371 Å hereafter called Si II 6350 Å. Type Ib SNe do not exhibit the Si II line but they show instead an absorption due to He I at 5876 Å. The Si II line is rather weak in SNe Ic compared to SNe Ia and the He I feature is absent in the early time spectra. The unambiguous difference between Ic and Ia is the S II doublet near 5500 Å. The type II SNe are characterised by prominent H Balmer lines that are present already at the phase around maximum light, although their intrinsic variety is much larger than in SNe I.

The nebular phase is reached a few months after peak luminosity. At that time the spectra of SNe Ia are dominated by blends of dozens of Fe emission lines and some Co lines, whereas SNe Ib/c show unblended lines of intermediate-mass elements (IME) like O or Ca. The line features that dominate the late time spectra of SNe II are strong H emission lines.

The UV part of the various types of SNe differs significantly from each other. All SNe I lack flux in this wavelength region due to line blanketing mostly from Fe II and Co II lines. In SNe Ia but not in type Ib/c the flux is also depressed in the infrared part of the spectra, whereas the continuum flux of most SNe II resembles almost perfectly a black body distribution. The famous SN 1987A is an exceptional case in this sense.

We have already mentioned the homogeneity of SNe Ia spectra, which also means a similar evolution. The early spectra show broad valleys and peaks over all wavelengths. The absorption troughs are mostly caused by singly ionised lines of IME. The major contributors are oxygen (O), silicon (Si), sulfur (S), calcium (Ca), and magnesium (Mg). Additionally, lines of iron (Fe) and cobalt (Co) are detected. Si II 6350 Å, Ca II H&K, and the Ca II IR-triplet are the strongest features in this phase. Convincing evidence for the detection of He or H, that does not come from any kind of interaction but is part of the SN ejecta, has never been shown. Figure 2.4 shows the maximum light spectra of normal and peculiar SNe Ia.

As the photosphere recedes, the lines of the Fe group elements become stronger. This means that SNe Ia consist of an iron-rich core, but still with significant contributions of IME to the spectral line features. After several months the nebular phase is reached and the spectra are dominated by forbidden Fe and Co lines (Axelrod 1980). The Co content decreases with the radioactive decay to stable ^{56}Fe .

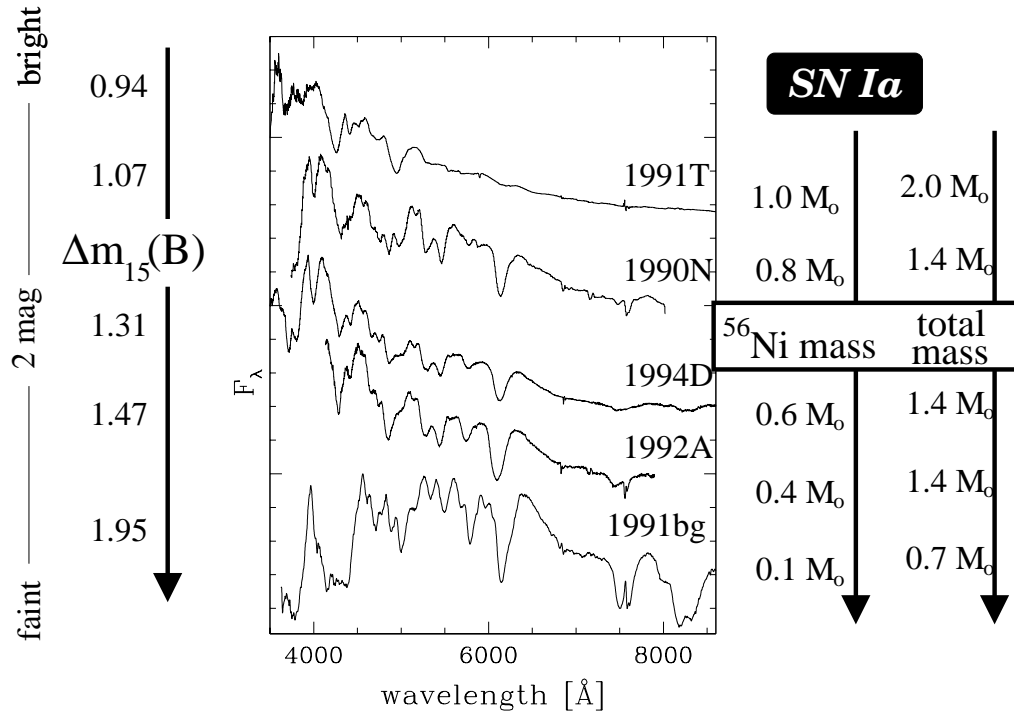


Figure 2.4: Comparison of the maximum light spectra of SNe Ia with different decline rates (left), and hence luminosities. The right panel shows the ^{56}Ni and total masses suggested by light curve and spectral synthesis models (Cappellaro & Turatto 2001).

SNe Ia show rather high line velocities ($\gtrsim 10,000 \text{ km s}^{-1}$), especially in the early time when radiation from the outer layers of the ejecta is observed. Different elements are expelled at different velocities. Thus, Ca often shows a velocity that is several thousand kilometers per second higher than the Si one. As a rule of thumb they all decrease rapidly in the first three weeks after the explosion. Benetti et al. (2004a) analyse the line velocities of a set of SNe Ia and find correlations between the line velocities and other properties, e.g. Δm_{15} .

Not only the light curves of SNe Ia but also the spectra are homogenous at least to a certain level and it is useful to collect template spectra at various epochs. However, there are also differences and heterogeneity seen, such as line strengths, line ratios, and line velocities. This dispersion can be used to derive information about the diversity of SNe Ia as a whole, as will be demonstrated in the Chapters 5–8.

2.1.3. Supernova Ia rates

Knowing about SN rates is of great importance, because they are mostly responsible for the enrichment of galaxies with higher elements. However, it is very difficult to derive reliable values for SN rates due to their rarity. This is even more true if they are separated into different classes and the various species are associated to the different types of galaxies. Most of the bins contain only a handful of objects or less and the statistics is simply too low. Moreover, it is not easy to find a suitable unit in which these values can be given. The most common unit is the number of events per 100 years per blue unit luminosity ($10^{10} L_{B_{\odot}}$). The blue luminosity is taken, because supernovae are thought to be linked to the stellar population which dominates the light of galaxies. This assumption is only true if the age and initial-mass function of the SNe are the same as those of the dominant stellar population. Given the presumably long evolution time of the SNe Ia progenitors, they are expected to occur more frequently in old stellar populations. Cappellaro et al. (1997), on the other hand, found that SNe Ia are more often observed in spiral galaxies than in ellipticals and S0. Moreover, SNe Ia are often found in spiral arms, i.e. star forming regions, or their vicinity. This makes the assumption questionable that the B luminosity correlates with the SNe Ia rates.

Cappellaro et al. (1997) and Reiss (1999) determine a rate of nearby SNe Ia of about 1 event every 500 to 600 years for a galaxy with $10^{10} L_{B_{\odot}}$, using a Hubble constant of $65 \text{ km s}^{-1} \text{ Mpc}^{-1}$. Two studies on more distant objects ($z > 0.3$) predict an even lower rate (Pain et al. 1996, Reiss 1999). This is not surprising since the search for SNe at higher redshifts becomes extremely difficult and very often these objects cannot be assigned unambiguously to a given class.

2.2. Progenitor scenarios

The quest for the true progenitor scenario of SNe Ia is still in full activity. Differences in the progenitors may be the key to understand the diversity of type Ia explosions (e.g. Nomoto et al. 2003, Röpke & Hillebrandt 2004b). The main problem in the determination of the correct scenario – if there is a single scenario at all – is the rarity of SNe Ia (Sect. 2.1.3) and the faintness and long evolution time (several Gyrs) of the WDs, the most likely progenitors of SNe Ia. Therefore

it is very difficult to solve this problem by means of observations and we have to rely on indirect measurements or traces of the progenitor in spectra and light curves. For more extended reviews we refer to Nomoto et al. (2000), Branch et al. (1995), and Livio (2000).

Identifying the SNe Ia progenitors is important for many reasons. In particular it is necessary to know about initial conditions of the ignition in order to calculate realistic models and to understand the explosions.

Supernovae Ia occur rather frequently in elliptical galaxies, suggesting that they are correlated with old stellar populations (Sect. 2.1.3). This excludes massive stars ($\gtrsim 8 M_{\odot}$) as possible progenitors which are found in young stellar populations. Single low-mass stars tend to end up as planetary nebulae when they blow away their envelopes through strong winds and leave behind a WD that can only cool down. Attempts to detect X-ray emission from compact SNe Ia remnants have failed, disfavoring a connection with a neutron star or a black hole. The lack of H and He lines in the spectra of SNe Ia gives a strong hint that the progenitor star lost most of its envelope prior to the explosion. This leaves us with a compact object in a binary system, most likely an accreting white dwarf (WD).

Three possible compositions are discussed for the WD. (1) He WDs have masses $\lesssim 0.45 M_{\odot}$ and are ignited when they have reached $\approx 0.7 M_{\odot}$. The disruption of a He WD produces only ^{56}Ni , its decay products, and some unburned He with no IME, contradicting the observations (Nomoto & Sugimoto 1977). (2) Considering WDs composed of O-Ne-Mg as a potential progenitor, there are two main objections. First, the rate of these objects is too low for them to serve as the major channel of SNe Ia. Second, these objects are expected to collapse rather than explode, leaving a neutron star behind (Saio & Nomoto 1985, 1998). (3) The most likely candidate is a C+O WD exploding after it has reached the Chandrasekhar mass limit ($\approx 1.4 M_{\odot}$) releasing of the order of 10^{51} ergs of kinetic energy.

The Chandrasekhar mass (M_{Ch}) of the ejecta in this scenario has long been regarded as the key to the homogeneity of SNe Ia. Variations on this basic scheme may also account for the peculiar events (Höflich et al. 1995). Sub-Chandrasekhar mass models are not yet ruled out. At least they could possibly explain some of the peculiar events like SN 2000cx (Nomoto et al. 2003). In sub-Chandrasekhar mass models the WD well below M_{Ch} accretes He from its

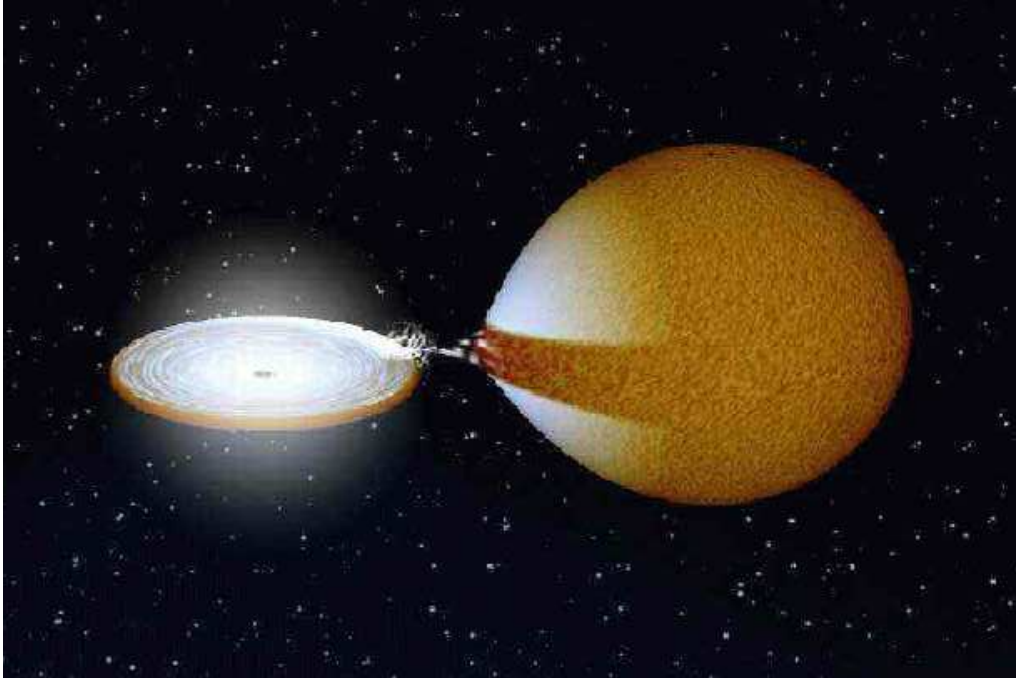


Figure 2.5.: Possible scenario for a progenitor system of a SN Ia. A white dwarf accretes material from its close companion by Roche lobe overflow. (Image from: Höflich et al. 2003).

companion until it has accumulated a He shell of $\sim 0.1 - 0.3 M_{\odot}$ on top of the C+O core. The He layer is then ignited off-center (Nomoto 1982b) and two waves – the He detonation wave in outward direction and the shockwave in inward direction through the C+O layer to ignite C-detonation in the center – blaze a trail through the WD (e.g. Arnett 1996). Indeed, synthetic spectra calculated on the basis of these models are much too blue compared to the observations (Höflich & Khokhlov 1996, Nugent et al. 1997).

Two possible configurations are usually discussed to describe the progenitor system with a M_{Ch} C+O WD. In the double degenerate scenario, two low-mass WDs in a close binary system lose angular momentum due to gravitational radiation (Iben & Tutukov 1984, Webbink 1984). The less massive star is torn into a disk around the companion, which finally leads to the merging of the two objects, exceeding the Chandrasekhar mass (Benz et al. 1990, Mochkovitch et al. 1997). A thermonuclear reaction front propagates from the disk inwards to the core and converts the star into O-Ne-Mg (Nomoto & Iben 1985), which finally

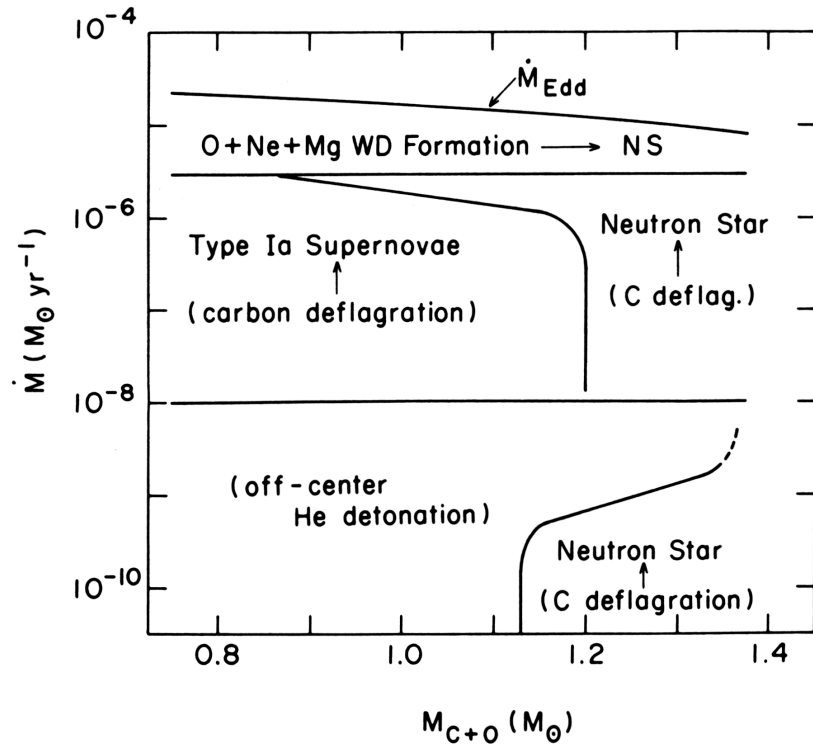


Figure 2.6.: Final fate of an accreting C+O WD depending on its initial mass $M_{\text{C+O}}$ and the accretion rate \dot{M} (Nomoto & Kondo 1991).

collapses to a neutron star. It is very doubtful that this model describes correctly the event of a SN Ia.

In the single degenerate scenario, the most widely accepted model for the main channel of SNe Ia, the WD accretes mass from a main-sequence star or a slightly evolved sub-giant until it comes close to the Chandrasekhar limit (Hachisu et al. 1999a, Fig. 2.5). During that phase the donor star has filled its Roche lobe and transfers H-rich material onto the WD. The evolution of the WD depends on the accretion rate \dot{M} , the composition of the transferred matter, and the initial mass of the WD (Nomoto 1982a, Nomoto & Kondo 1991). Only in a small range $10^{-8} \lesssim \dot{M} \lesssim 4 \times 10^{-6} M_{\odot} \text{ yr}^{-1}$ and $M_{\text{C+O}} < M_{\odot}$ the H and He burn steadily or with weak flashes and the mass of the WD grows (Fig. 2.6). If the accretion rate exceeds $4 \times 10^{-6} M_{\odot} \text{ yr}^{-1}$, the WD blows off a strong wind that reduces the \dot{M} to an effective rate below $10^{-6} M_{\odot} \text{ yr}^{-1}$ and no extended envelope around the accreting WD is formed (Hachisu et al. 1999a,b). When

M_{Ch} is reached after several thousand years of quiet burning, carbon burning is triggered by compressional heating near the centre of the WD evolving into a thermonuclear runaway that eventually disrupts the complete star (Whelan & Iben 1973, Nomoto 1982a,b, Han & Podsiadlowski 2004). The biggest uncertainty of this scenario is the narrow region for the values of \dot{M} and the initial mass of the WD (see, however, Hachisu et al. 1999a,b).

Late-breaking heavy support for this progenitor scenario is given by the recent identification of the companion star of Tycho's supernova SN 1572 (Ruiz-Lapuente et al. 2004). However, despite all these advantages of this model the final answer for the true progenitor system of SNe Ia remains open.

Potential progenitor systems for both types, single-degenerate and double-degenerate binary system, have been detected but their number is far too low to explain the frequency of occurrence of SNe Ia (Cappellaro et al. 1999).

2.3. Explosion mechanism

The explosion is the only part in the chain of SNe Ia evolution that can never be observed directly. Numerical simulations, using the input from different progenitor models, are needed to provide the density, temperature, composition, and velocity fields of the SN ejecta. The results serve as input for synthetic spectra and light curve calculations, and can thereby be tested against observations. To be more precise, the explosion models have to fulfill the following requirements given by the observations: (1) The composition and the velocity have to reproduce spectral features and light curves. (2) The homogeneity of SNe Ia requires a high level of robustness of the numerical models, so that they do not depend on the fine-tuning of model parameters. (3) Despite the robustness models should also account for the variability in the explosion strength. (4) Explosion models must be closely connected with the physics of the progenitor system. Even though in this field large progress has been made in the last decade (Hillebrandt & Niemeyer 2000), there are still many open questions waiting to be answered.

Since the prompt detonation mechanism (Arnett 1969) has been ruled out long ago, because it fails to produce sufficient amounts of IME and is therefore agreed to be inconsistent with SNe Ia spectra, alternative explanations had to be

considered. In any case ignition occurs near the centre of the WD at a critical density $\rho_c \sim 1.3 - 2.5 \times 10^9 \text{ g cm}^{-3}$ and a temperature $T_c \sim 8 \times 10^8 \text{ K}$. A subsonic (deflagration) wave, often called a “flame”, travels outwards burning parts of the WD to nuclear statistical equilibrium (NSE). Unlike detonations, the subsonic speed of the deflagration front prevents the WD from being burnt to NSE entirely. Partial burning of C/O material allows the production of IME like Si, S, Mg and Ca (Nomoto et al. 1976, 1984). These species dominate the spectra of SNe Ia in the early phase.

The main difficulty in modelling SN explosions is the huge range of length scales, covering more than 10 orders of magnitude. Due to the lack of computational power until the mid-1990s most studies of SNe Ia explosion models were carried out in 1-D, spherically symmetric configurations. These approaches naturally neglect important aspects of multidimensional thermonuclear burning, e.g. off-center ignition, flame instabilities, and turbulence. Further developments first included the dynamics in a second dimension (Livne 1993, Niemeyer & Hillebrandt 1995b, Reinecke et al. 1999a) and later even 3-D calculations (Khokhlov 1994, 1995, Benz 1997). Finally, it became possible to understand and to simulate the relevant burning and diffusion scales of microscopic flame instabilities and flame-turbulence interactions in 3-D (Niemeyer & Hillebrandt 1995a, Khokhlov 1995, Niemeyer et al. 1999).

There is still no agreement about whether the explosion happens as a pure subsonic deflagration that becomes strongly turbulent (Nomoto et al. 1984, Woosley et al. 1984, Niemeyer & Hillebrandt 1995a, Reinecke et al. 2002) or there is a transition from that regime to a supersonic detonation (often called Deflagration Detonation Transition (DDT), Khokhlov 1991, Woosley & Weaver 1994) at a certain density ρ_{DDT} . Recent 3-D deflagration models leave a significant amount of unburned material in the outer regions of the ejecta and at low velocities (Gamezo et al. 2003, Reinecke et al. 1999b, Travaglio et al. 2004). Furthermore, the models may produce slightly too little radioactive ^{56}Ni which powers the light curve of SNe Ia through the energy released in the decay chain via ^{56}Co to stable ^{56}Fe . However, great progress has been made recently and we are almost ready to use the density structure of deflagration models as direct input for synthetic spectra calculations. It is then also possible to probe the nucleosynthesis predictions of these models and to give valuable feedback in order to improve the explosion model. The great success of deflagration models is now the un-

derstanding of all the physics on all length scales (Röpke & Hillebrandt 2004a). Delayed detonation models, on the other hand, describe better the abundances of Fe group elements and IME at high velocities since in the detonation phase the burning process is boosted and outer regions of the envelope are partially or even completely burned to heavier elements (Höflich & Khokhlov 1996, Iwamoto et al. 1999). These models also have the flexibility to produce different amounts of ^{56}Ni and IME, but this depends on the ad-hoc assumption of the time and position of occurrence of the transition from a deflagration to a detonation.

Hence, there is still need for a more complete understanding of the explosion mechanism. The debate whether there is a transition from a deflagration to a detonation at some point or not continuous, but the solution may not be far coming.

3. Radiation transfer methods

Synthetic spectra are necessary for coupling the interior physics of an exploding WD to what is finally observed and to test potential progenitor and explosion models. High energy particles are deposited in the SN envelope, where they are degraded into photons of UV, optical, and IR wavelengths. These photons then interact with matter before they escape the ejecta. When the material interacts with the photons, it leaves its fingerprint on the radiation field, which gives rise to the specific spectrum. In order to reproduce the observations by means of spectral synthesis, the radiative transfer in the SN envelope must be simulated. From the purely physical point of view, the equations to be solved to treat radiative transfer are well known. However, unlike stellar atmospheres, SNe ejecta are blown off at very high velocities, and the problem becomes non-local. This increases the effort to solve the relevant equations, and therefore the numerical costs are enormous and the codes are difficult to handle even in times of powerful computers.

This Chapter gives a basic framework for the problem of radiative transfer calculations in Section 3.1 and describes the specific case of SN ejecta in Section 3.2. Different approaches are discussed in Section 3.3.

3.1. The radiative transfer equation

The basic physics of radiation transport in stellar atmospheres that also basically applies to SNe is described in detail in Mihalas (1978).

The fundamental quantity in every problem involving radiation, although not measurable directly, is the *specific intensity* $I_\nu(\vec{r}, \hat{n}, t)$. It is defined at position \vec{r} , travelling in direction \hat{n} at time t , as the amount of energy dE , per unit frequency interval $d\nu$, passing through a unit area dA oriented normal to the beam, into a

solid angle $d\Omega$, in a time interval between t and $t + dt$:

$$dE = I_\nu(\vec{r}, \hat{n}, t) dA \cos \theta d\nu d\Omega t \quad (3.1)$$

Here, the angle between the normal of the reference surface dA and the direction \hat{n} is denoted as $\cos \theta$. The units of specific intensity are $\text{ergs s}^{-1} \text{ Hz}^{-1} \text{ cm}^{-2} \text{ sterad}^{-1}$.

Spectra show features, because radiation interacts with matter. There are two ways by which matter can influence a beam of radiation. Emission of radiation is described by the *emission coefficient* j_ν ($\text{ergs s}^{-1} \text{ cm}^{-3} \text{ Hz}^{-1} \text{ sterad}^{-1}$), while the *absorption coefficient*

$$k_\nu = \kappa_\nu + \sigma_\nu \quad (3.2)$$

gives the loss of radiation due to absorption κ_ν and scattering out of the beam σ_ν , and is therefore a measure of the overall attenuation of the radiation.

If we combine the changes in intensity of a radiation beam along the path ds , we obtain the *radiative transfer equation* for radiation of frequency ν :

$$\frac{\partial I_\nu(\vec{r}, \hat{n})}{\partial s} = -k_\nu I_\nu + j_\nu \quad (3.3)$$

It can be seen from the equation that the extinction, the absorption and the scattering coefficients have the dimensions of reciprocal length [cm^{-1}]. The coefficients depend on the frequency ν as well as on the type and state of the material (chemical composition, temperature, pressure).

If the beam passes through a non-emitting layer ($j_\nu = 0$), the intensity I_ν after traversing the layer of thickness s is related to the incident radiation by:

$$I_\nu = I_{\nu,0} \cdot e^{-\tau_\nu} , \quad (3.4)$$

where the dimensionless quantity

$$\tau_\nu = \int_0^s k_\nu ds \quad (3.5)$$

is termed the *optical depth* of the transmitting layer. Using the optical depth the radiation transfer equation can be rewritten in the form:

$$\frac{\partial I_\nu(\vec{r}, \hat{n})}{\partial \tau_\nu} = -I_\nu + \frac{j_\nu}{k_\nu} = -I_\nu + S_\nu \quad (3.6)$$

where we have introduced the *source function* as the ratio of emission to absorption coefficients.

In an atmosphere that is in *thermodynamic equilibrium* the source function is a universal function of ν depending only on the local temperature T , and is described by the Planck radiation formula or black body function:

$$S_\nu = B_\nu(T) = \frac{2h\nu^3}{c^2} \frac{1}{e^{h\nu/kT} - 1} \quad (\text{Kirchhoff's Law}) \quad (3.7)$$

However, thinking of a purely scattering atmosphere the source function becomes equal to the mean intensity J_ν , which is the integrated intensity over all incident directions.

$$J_\nu(\vec{r}) = \frac{1}{4\pi} \oint I_\nu(\vec{r}, \hat{n}) d\Omega \quad (3.8)$$

In this case the source function depends not on the local temperature but on distant points where the radiation originally was emitted, which shows the difficulty in solving the simple looking Equation 3.6. Even in the simple case of pure scattering the equation couples different directions \hat{n} together and becomes a nonlocal problem. In the more general case, both S_ν and τ_ν depend on I_ν in a very complicated way, including detailed knowledge about the excitation and ionisation state of the gas. Thus, the radiative transfer equation is coupled to the equations of statistical equilibrium (Mihalas 1978).

Usually, Equation 3.6 is numerically solved. The solution of the radiative transfer equation for several different beams through the atmosphere is obtained. Then, I_ν is integrated over the stellar surface, which finally gives the observed flux for a specific frequency ν .

3.2. Radiative transfer in SN ejecta

Radiation transport in SN ejecta differs significantly from that in stellar atmospheres or even stellar winds, which are closer to the situation of SNe. At the time of the explosion physical scales are relatively small in SNe, but shortly thereafter the ejected matter expands freely and attains large distances owing to the high velocities (up to a few percent of the speed of light). Every point in the envelope moves at a constant velocity and therefore all structures scale linearly with time t_{exp} since the explosion. Homologous expansion has important advantages:

1. The radial velocity v is a convenient coordinate in the co-moving frame giving the actual radius as $r = v t_{exp}$.
2. The density at a co-moving point just scales with t_{exp}^{-3} .
3. If two matter elements have a velocity difference of Δv , the redshift of a photon $\Delta\lambda = \lambda(\Delta v/c)$ is time-independent.

However, because of the large velocities (up to $\sim 30,000 \text{ km s}^{-1}$) in SNe Ia ejecta a single continuum photon can interact with many spectral lines on its path through the atmosphere due to its progressive redshift in the co-moving frame of the expanding envelope. The Doppler overlapping of lines couples different regions of the envelope and makes the radiation transfer equation extremely difficult to solve.

On the other hand, the large velocity gradient justifies using the *Sobolev approximation*. This means that the intrinsic absorption coefficients for line interaction can be described as delta functions in wavelength, because the Doppler profile dominates. Thus, a photon with specific redshift at a specific radial position can only be absorbed by a single line with which it is in resonance. This assumption is particularly sound in SN envelopes, where the velocities are so large that the resonance region of a line is very small compared to the length scale over which physical properties change. The Sobolev approximation must not be confused with the line overlapping discussed before.

When synthetic spectra of SNe are calculated, two phases must be distinguished. The early phase, which lasts from the explosion until a few days after maximum light, is characterised by a photosphere that emits continuum radiation. It is consequentially called the *photospheric phase*. The photosphere can be idealised as an infinitely thin layer, above which no continuum is formed. In the case of SNe Ia, continuum opacities are small compared to the effect of line blanketing (Pauldrach et al. 2001), and so we can talk of a line-dominated pseudo photosphere. This justifies the assumption of the Schuster-Schwarzschild approximation. Above the photosphere, line opacity can be very large as mentioned before. This results in the typical early SNe Ia spectrum with deep and broad P-Cygni lines superimposed on the photospheric continuum. As expansion proceeds, the photosphere and the region of line formation recede deeper into the ejecta decreasing the P-Cygni line profile blueshift with time.

A couple of months after the explosion the *nebular phase* is reached, and the ejecta become optically thin in all wavelength regions. At this time there is no photosphere, and therefore no continuum flux to be scattered. Hence, we no longer observe P-Cygni line profiles but rather nebular emission lines that peak near their rest wavelength, since the average velocity of the SN nebula is zero. Thus, non-local radiative transfer effects tend to be negligible. This physical situation demands a different treatment of the radiation transfer with respect to the photospheric phase, which is not discussed in more detail here. For an overview of different techniques see Branch et al. (2003a) and references therein. Although these phases illustrate two quite different physical situations, there is a transition time in which both phases play a role.

3.3. Numerical approaches to the problem

We give here a brief presentation of the various methods to calculate radiation transport in the ejecta of SNe Ia. Each of these approaches has advantages but also shortcomings and the choice which one to take depends on one's needs.

As already mentioned above, the main challenge in calculating synthetic spectra is the complexity that is introduced by the interdependence of the various aspects that have to be considered. Although Equation 3.6 looks rather simple, the radiative transfer equation is eventually a time-dependent, frequency-dependent problem that is strongly coupled to the calculation of the occupation numbers of the energy levels and in the case of SNe the energy deposition from the radioactive decay has to be taken into account. This situation makes it impossible to deal with the whole problem numerically, simply because it is too time consuming and computationally too expensive even in the simplest configuration, which is a spherically symmetric one, using modern computer systems. Therefore, further approximations of various kinds have been introduced to reduce the calculation to a feasible level. Several 1-D codes at different levels of complexity have been established (Eastman & Pinto 1993, Höflich 1995, Pauldrach et al. 1996, Hauschildt & Baron 1999) or are under development (Sauer; priv. comm.). They have the advantage that they could calculate synthetic spectra from first principles, meaning they could be a consistent continuation of progenitor and explosion models. However, these codes themselves are either

highly parametrised (e.g. SYNOW; Fisher 2000) or they are rather inefficient due to their sophisticated numerical algorithms. Moreover, they do not yet reproduce observations sufficiently well, failing to meet their most important requirement.

Unlike the traditional approaches, the Monte Carlo (MC) method allows a straightforward treatment of the multiline transfer of radiation. Moreover, they do not incorporate such computationally expensive and complex numerics. This also makes MC codes more robust and they are easier to develop. Since the MC method is a probabilistic way of treating the radiation transfer problem, a very large number of MC experiments have to be carried out in order to suppress random noise in the results. Hence, MC codes had to fight the same shortcoming as the traditional approaches, the lack of sufficient computer power. Nowadays even rather complex versions of MC codes can be run on a single workstation or on multiprocessor machines because they can easily be parallelised.

Monte Carlo codes are especially suited to treat radiative transfer in SNe Ia with their strong overlap of lines. Because it follows individual photons or energy packets through the ejecta, the MC method deals naturally with this problem and does not explicitly have to take into account a huge number of lines simultaneously caused by the line blocking effects (Pauldrach et al. 2001).

Kasen (2004) uses these advantages and the fact that MC codes do not rely on a specific symmetry in the problem to calculate 3-D spectra including polarisation.

Our MC code sets its emphasis on efficiency and robustness being a powerful tool to analyse many spectra of different objects shortly after they have been observed and the data have been reduced. It is very suitable for parameter studies and analyses of large data samples from which information about diversity and systematics can be derived. It makes use of the advantages of both MC induced speed and accuracy by calculating the level populations in approximated NLTE. The emergent spectrum is achieved not simply by binning the escaping photons to their frequencies but a formal integral solution calculation is carried out at the end of the MC experiment (Chapt. 4).

4. The Monte Carlo code

Model calculations in the photospheric epoch presented in this work are based on a MC code originally developed by Abbott & Lucy (1985) to treat multiline radiation transfer in stellar winds. The code was then adapted and improved in several steps to treat the physics of SNe (Mazzali & Lucy 1993, Lucy 1999a,b, Mazzali 2000).

In this Chapter the basic structure and the numerical method of the MC code are explained, as well as its specific advantages with respect to the solution of the physical problems inherent to computing synthetic SN spectra. New improvements and modifications to this work are described together with applications on real data in the next Chapters.

4.1. Model supernova envelope

One of the basic assumptions used when computing synthetic SN spectra is that the physical conditions remain constant during one calculation. In principle the problem is time-dependent (Pinto & Eastman 2000), because photons that are emitted deep in the ejecta have a larger diffusion time than the characteristic time of the physical conditions. Also the energy input from the radioactive decay of ^{56}Ni and ^{56}Co changes with time, owing to their different half life. However, our MC code deals only with photons that travel above the dense photosphere through the envelope, where the diffusion time is short, and our assumption of time independency is therefore justified.

The density structure is different for the various types of SNe. The density decreases with time due to the fast expansion of the ejecta. In general the density drops rather quickly with radius, with a typical behaviour $\rho \propto r^{-7}$ (due to the homologous expansion), except in the innermost part which is flatter. The photosphere moves inwards in velocity space as the envelope expands, but stays roughly speaking at a constant density. Therefore the density structure $\rho(v)$ can

be rescaled to the actual epoch of the calculation assuming free and homologous expansion of the ejecta. For the case of SNe Ia, and therefore in all calculations presented in this work, the density profile from the standard explosion model W7 (Nomoto et al. 1984) is used.

The effect of the homologous expansion on the photons can be compared to the Hubble flow. The Hubble flow denotes the region beyond the Local Group, where peculiar velocities due to gravitational interaction are negligible compared to the expansion of the Universe. At each point in the Hubble flow one sees everything else drifting away. Thus, all arriving light signals from distant sources are redshifted proportionally to their distance which can be interpreted as a Doppler effect. Since homologous expansion means that each particle in the SN ejecta moves at a constant velocity in Lagrangian coordinates with the velocity increasing proportionally to the radius, an outwards travelling photon becomes more and more redshifted relative to its surrounding material.

4.1.1. Temperature stratification

Since the SN envelope emits energy and includes backwarming, the temperature structure is non-isothermal. Performing occupation number calculations requires knowledge of the temperature. Here a simplified method to calculate radiative equilibrium and to derive the radiation temperature $T_R(r)$ is adopted.

The mean energy of a photon in a black body radiation field is given by

$$\bar{x} = \frac{h\bar{\nu}}{kT} \quad (4.1)$$

with $\bar{x} = 3.832$ (Mazzali & Lucy 1993). The radiation temperature is computed from this equation after the frequency moment is known from

$$\bar{\nu} = \frac{\int_0^\infty \nu J_\nu d\nu}{\int_0^\infty J_\nu d\nu} \quad (4.2)$$

Iterating between the occupation numbers of the energy levels of the ions and the radiation field using the most recent value of T_R gives the temperature structure in the SN ejecta. The electron temperature is defined to be

$$T_e(r) = 0.9 T_R(r) \quad (4.3)$$

to simulate very approximately the radiative control of the electron temperature (Klein & Castor 1978). The starting point for the iteration is $T_R(r) = T_{\text{eff}}$ where the effective temperature T_{eff} is given by the photospheric radius R_{ph} and the luminosity L via the relation $L = 4 \pi R_{ph}^2 \sigma T_{\text{eff}}^4$.

The effect of viewing a finite photosphere and of the progressive degradation of the radiation upon its interaction with the envelope matter is such that $J(r)$ falls below $B(T_R(r))$. This allows us to compute an equivalent dilution factor W through (Mihalas 1978):

$$J = W B(T_{\text{eff}}) = W \frac{\sigma}{\pi} T_R^4 \quad (4.4)$$

4.1.2. Method of radiative transfer

The MC code adopts a purely scattering envelope with respect to interactions with electrons. Line absorption is treated differently, but nevertheless no continuum opacity is assumed. In order to account for this environment a sharply defined photosphere is needed where all radiation is emitted (*Schuster-Schwarzschild approximation*). If a photon is absorbed by a line, all possible transitions from the upper level down to lower levels $u \rightarrow \ell$ are considered. These rates are computed and each transition is assigned a weight proportional to its effective downward rate, i.e. correcting for photon trapping. This will be explained in detail in Section 4.2.4. One of the transitions is chosen randomly but according to its assigned weight. Once the photon is re-emitted in a random direction the MC procedure starts again as it is described in Section 4.2.4.

The intensity

$$I_\nu(s) = I_\nu(0) \exp [-(\tau_e + \tau_L)] \quad (4.5)$$

shows the attenuation of a beam of radiation along a distance s . Here, τ_e is the integrated electron (Thomson) scattering optical depth, and τ_L is the integrated line optical depth. The treatment of line interaction makes use of the Sobolev approximation (Mihalas 1978), so that a photon with rest frequency ν interacts with lines of progressively lower frequency when it travels through the ejecta, as explained in Section 4.1.

We also mentioned before that in the SN envelope $v \propto r$, and therefore $dv/dr \equiv v/r$. Hence, the optical depth of a single line is given by (Abbott & Lucy 1985):

$$\tau_\ell = \kappa \rho \lambda \frac{r}{v} \quad (4.6)$$

with

$$\kappa \rho = \frac{\pi e^2}{m_e c} n_\ell f_{\ell u} \quad (4.7)$$

where e is the electron charge, m_e is the electron rest mass, n_ℓ denotes the population of the lower level of the line transition, and $f_{\ell u}$ is the oscillator strength of the transition.

Section 4.2.4 describes how the interactions with electrons and lines are implemented in the MC procedure.

4.1.3. Ionisation and excitation

In order to compute the line optical depths it is necessary to know the level occupation numbers of the atoms. In principle this would mean to solve simultaneously the coupled equation of radiative transfer and statistical equilibrium. This is particularly complex in a SN envelope with many different ions and species. Therefore a more simplified approach is used, namely a modified nebular approximation. The level populations are taken from Lucy (1999b), Abbott & Lucy (1985), Castor (1970), and Lucy (1971). The assumption is justified by the low densities in the SN ejecta. Using Equation 4.4, i.e. a diluted radiation field and considering ionisation from excited levels as well as from the ground state leads to an ionisation equation of:

$$\frac{n_{j+1}n_e}{n_j} = W[\zeta + W(1 - \zeta)] \left(\frac{T_e}{T_R}\right)^{1/2} \left(\frac{n_{j+1}n_e}{n_j}\right)_{T_R}^* \quad (4.8)$$

where W is the dilution factor, ζ is the fraction of recombinations going directly to the ground state, $W^2(1 - \zeta)$ represents photoionisation from excited levels, and the starred terms mean LTE.

However, this is not sufficient to account for the situation of ionisation in SNe. As we know from observations there are two wavelength regimes that have to be treated differently with respect to our procedure. The UV part of the spectrum, where most of the ionisation edges occur, is optically thick whereas the region of

longer wavelengths turns out to be optically thin. Thus, the spectrum is divided into two regions, where the radiation field has different forms assuming that the border between the two regimes lies at the first major ionisation edge with energy $\chi_0 = h\nu_0$:

$$J_\nu = W B_\nu(T_R) \quad \text{for } \nu < \nu_0 \quad (4.9)$$

and

$$J_\nu = b_1^{-1} B_\nu(T_e) \quad \text{for } \nu \geq \nu_0 \quad (4.10)$$

where b_1 is a weighted mean departure coefficient for the ground states of the ions at high frequencies. Hence, the optically thin region is described by a diluted black body at the local radiation temperature, while in the optically thick continuum the radiation field has the form of a locally emitted black body ($W = 1$) determined by T_e .

This assumption has consequences on the ionisation equation. Equation 4.8 still holds for the optically thin regime, whereas it has to be modified for $\nu \geq \nu_0$. Additionally it is assumed that photoionisations from excited levels only occur in the region of the optically thin continuum. Introducing a correction factor δ Equation 4.8 can be rewritten as

$$\frac{n_{j+1}n_e}{n_j} = W[\delta\zeta + W(1 - \zeta)] \left(\frac{T_e}{T_R}\right)^{1/2} \left(\frac{n_{j+1}n_e}{n_j}\right)_{T_R}^* \quad (4.11)$$

If the ionisation threshold χ_T of a specific ion lies above χ_0 and we are in the optically thick region, the constraint for δ to recover the Saha equation gives

$$\delta = \frac{T_e}{b_1 W T_R} \exp\left(\frac{\chi_T}{k T_R} - \frac{\chi_T}{k T_e}\right) \quad (4.12)$$

and the ionisation equation becomes

$$\frac{n_{j+1}n_e}{n_j} = \zeta \left(\frac{n_{j+1}n_e}{n_j}\right)_{T_e}^* + W^2(1 - \zeta) \left(\frac{T_e}{T_R}\right)^{1/2} \left(\frac{n_{j+1}n_e}{n_j}\right)_{T_R}^* \quad (4.13)$$

In the second case, where $\chi_T < \chi_0$, there are two possibilities for the energy of the photon. If $h\nu \geq \chi_0 > \chi_T$, it lies in the optically thick continuum. On the other hand it belongs to the optically thin region if $\chi_0 > h\nu \geq \chi_T$.

The photoionisation rate is then split in two parts:

$$R_{ik} = 4\pi \int_{\nu_T}^{\nu_0} \alpha_\nu \frac{WB_\nu(T_R)}{h\nu} d\nu + 4\pi \int_{\nu_0}^{\infty} \alpha_\nu \frac{B_\nu(T_e)}{b_1 h\nu} d\nu \quad (4.14)$$

The subscript κ denotes processes involving the continuum and α_ν stands for the photoionisation cross section. Assuming $\alpha_\nu = \alpha_T(\nu_T/\nu)^2$, where α_T is the photoionisation cross section at the threshold, and taking the Wien limit $h\nu \gg kT_e$ for B_ν the photoionisation rate becomes

$$\begin{aligned} R_{ik} &= \frac{8\pi}{c^2} \alpha_T \nu_T^2 \left[W \int_{\nu_T}^{\nu_0} \exp\left(-\frac{h\nu}{kT_R}\right) d\nu + \frac{1}{b_1} \int_{\nu_0}^{\infty} \exp\left(-\frac{h\nu}{kT_e}\right) d\nu \right] \\ &= \frac{8\pi}{c^2} \alpha_T \nu_T^2 \left\{ W \frac{kT_R}{h} \left[\exp\left(-\frac{h\nu_T}{kT_R}\right) - \exp\left(-\frac{h\nu_0}{kT_R}\right) \right] + \frac{kT_e}{b_1 h} \exp\left(-\frac{h\nu_0}{kT_e}\right) \right\} \end{aligned} \quad (4.15)$$

If we compare this with the result of the nebular approximation from (Abbott & Lucy 1985),

$$R_{ik} = \frac{8\pi}{c^2} \alpha_T \nu_T^2 W \frac{kT_R}{h} \exp\left(-\frac{h\nu_T}{kT_R}\right) \quad (4.16)$$

we see that the correction factor δ for ground state ionisation is:

$$\delta = 1 - \exp\left(\frac{h\nu_T}{kT_R} - \frac{h\nu_0}{kT_R}\right) + \frac{T_e}{b_1 W T_R} \exp\left(\frac{h\nu_T}{kT_R} - \frac{h\nu_0}{kT_e}\right) \quad (4.17)$$

Since $T_e \sim T_R$ throughout the envelope (Sect. 4.1.1), it is a sound approximation to use a departure coefficient $b_1 = W^{-1}$. For the case of SNe Ia we set $\lambda_0 = 1050 \text{ \AA}$, including the Ca II which is the redmost of the important ionisation edges.

4.2. Numerical technique

In this section the numerical technique to calculate synthetic spectra with the MC method is presented.

4.2.1. Input data

The setup requires several input parameters. The density (versus velocity) is given by the underlying explosion model. The emergent luminosity L , the

epoch t_{exp} (time since explosion), and the estimated velocity of the photosphere v_{ph} , together with the chemical composition complete the set of adjustable quantities. The new treatment of the composition is explained in Section 5.2. The code divides the SN envelope into a number of shells (typically ~ 20). Their thickness increases as a function of radius. All physical properties – except for the velocity – are assumed to be constant in a particular shell and are set to the value at the mid-point of the shell. We adopt homologous expansion of the ejecta and therefore the velocity v is a continuous function of radius: $v = r/t$.

4.2.2. Line selection

The MC code makes use of the line list of Kurucz & Bell (1995) and is extended with the gf values for C II from Wiese et al. (1996). After eliminating weak lines a final set of transitions is generated that contains some 500,000 lines. The data are compacted in two files. One is a list of levels and the corresponding J -values for each ion. The second file contains a reference to the upper and lower levels of each transition plus their gf values. Due to the different treatment of excited and metastable states for the excitation the latter are marked with a minus symbol ($-E_i, -\ell$) and are easily recognised during the computation.

From this line list an appropriate set of lines is selected during the first temperature iteration according to the actual abundances and temperature in the SN ejecta. Such a working line list typically includes 50,000-100,000 lines. Again the list is organised into two files. The first one includes all lines ordered by frequency $\nu_{k+1} > \nu_k$, while in the other the lines are grouped to ions and then according to the index u of the upper levels of the transitions. This is a big advantage for the final calculations increasing the speed and the efficiency of the code. Since the SN envelope expands, the co-moving frequency of a photon decreases as it travels through the ejecta. The next possible line that may absorb the photon is always the redder one, which is the next entry in the list. After a photon has been absorbed all allowed downward transitions can be found quickly in the second list.

4.2.3. Determination of the temperature structure

In order to calculate the occupation numbers and the line optical depths, we need to know the temperature structure in the envelope. The temperature structure is

determined iteratively by running a series of small MC experiments starting with a constant value for $T_R = T_{\text{eff}}$ and $T_e = 0.9 T_R$. Usually six iterations are sufficient to achieve convergence to the approximate radiative equilibrium carried out as described in Section 4.1.1.

Not only $T_R(r)$ is calculated with this method, but also the temperature of the black body T_B necessary to produce the required luminosity L . After several interactions with lines and electrons photons may eventually re-enter the photosphere increasing the black body temperature. This effect is known as *backwarming* which leads to a higher value of T_B compared to T_{eff} , as well as to a larger temperature gradient at and right above the photosphere.

Since the MC code uses branching for the downward transitions of the photons, backwarming and computation time are reduced compared to a purely scattering envelope. This can be explained as follows: In the SN envelope lines efficiently block broad regions of the spectrum and photons can only escape if they reach a ‘line-free’ spectral window. In the case of scattering the next available window is always the next one to the red in the co-moving frequency of the photon. In order to reach this window the photon has eventually to undergo many scattering events and the probability of being re-absorbed in the photosphere is rather high. On the other hand, branching allows the photons to make big ‘jumps’ in frequency during one single event. Since it is more likely that the photon is shifted from the blue to the red, it can reach a line-free region in the spectrum where it can escape much more easily. Moreover, the diffusion time of the photons is reduced significantly and so is the computation time.

4.2.4. Radiative transfer

After all the input data are gathered, the appropriate line list has been built, and the temperature structure has been determined, the real MC calculation can begin. The event histories of a number of energy packets are followed adopting the Sobolev approximation. The photospheric luminosity L_{ph} is divided evenly among N packets, so that each packet has the same initial energy $\epsilon_0 = L_{ph}/N$ in the rest frame of the WD. Each packet contains a number of photons n_ν , where $n_\nu h\nu = \epsilon$. Using energy packets rather than photons leads to a more accurate sampling of the radiation field at the wavelengths where the bulk of the energy emerges and avoids following an unnecessarily large number of IR photons. All

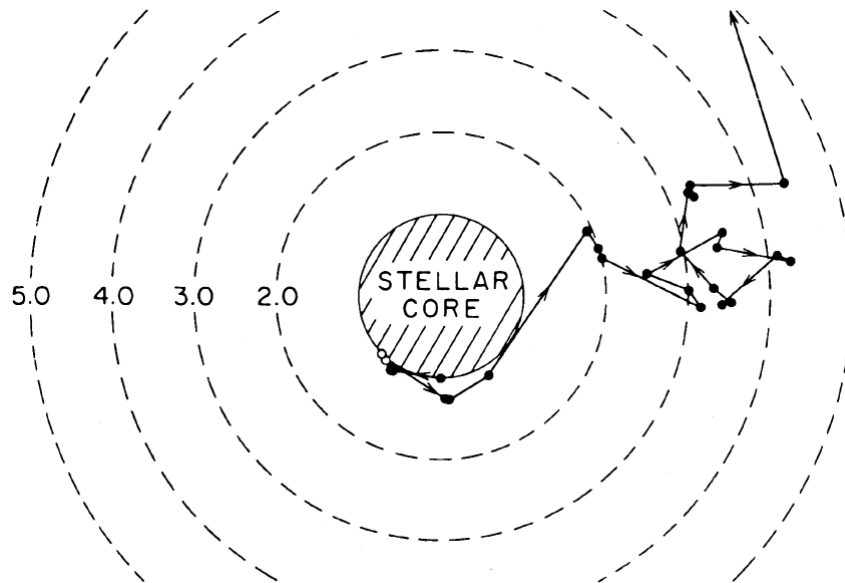


Figure 4.1.: Random walk of a photon through the SN ejecta (Abbott & Lucy 1985). Filled circles indicate interactions with lines, while open circles indicate electron scattering.

processes involved in the computation preserve the energy ϵ in the co-moving frame of the packets. Even in the case of branching after a line absorption the energy is conserved, only the number of photons in the packet changes. The distribution of the packets with frequency is determined by sampling the Planck function $B_\nu(T_{\text{eff}})$ each bin containing an integer number of packets.

Monte Carlo experiments

A randomly chosen frequency in the specific bin and a random direction cosine are assigned to each packet. Then the event history of each packet is followed as it travels through the envelope. A schematic diagram of such a random walk is shown in Fig. 4.1. There are two possibilities for the fate of a packet. Either it is scattered back into the photosphere, or it escapes the envelope possibly after undergoing line interaction or electron scattering.

The main task of the MC calculation is to determine whether a packet encounters a line or scattering event before it can cross the border to the next shell where the physical conditions change. First, a random “event” optical depth is selected

as $\tau_R = -\ln(1 - z)$, where z is a random number $0 \leq z < 1$. Electron scattering is a linear function of distance, whereas line interactions are restricted to certain points in the ejecta where the co-moving frequency is in resonance with a spectral line. The photon (or energy packet) encounters an electron scattering optical depth τ_e during its flight and the length of the path s_e has to be calculated before τ_e becomes equal to τ_R . Here, $\tau_R = \sigma_T n_e(i) s_e$, where σ_T is the Thomson electron cross section and $n_e(i)$ denotes the electron density in the i th shell. If s_e is less than the distance for the photon to leave the shell, the packet may suffer electron scattering. In the next step the distance to the next line encounter s_ℓ is compared to s_e by simply calculating the photon's co-moving frequency $\nu' = \nu [1 - \mu (v/c)]$.

Finally, both s_e and s_ℓ have to be compared to the distance to the edge of the shell s_{sh} . The smallest of these three values decides what happens next to the photon.

1. If the photon is closest to the shell's edge, it enters the next shell with new physical conditions and a new optical depth calculation must begin.
2. If electron scattering occurs next, a new random direction is assigned to the packet and the MC experiment starts again.
3. Finally, if the photon encounters a line event, the actual downward transition has to be chosen. In this case the probability of each transition from level u is computed through the effective downward rate $A_{u\ell}\beta_{u\ell}$, where $A_{u\ell}$ is the Einstein coefficient for spontaneous emission, and

$$\beta_{u\ell} = \frac{1}{\tau_{u\ell}} (1 - e^{-\tau_{u\ell}}) \quad (4.18)$$

is the escape probability (Lucy 1999b). Finally, $\tau_{u\ell}$ denotes the Sobolev optical depth:

$$\tau_{u\ell} = h\nu_{u\ell} (B_{\ell u}n_\ell - B_{u\ell}n_u) \frac{\lambda_{u\ell}t}{4\pi} \quad (4.19)$$

The probability of spontaneous decay from level u to level ℓ after absorption is given by:

$$p_{u\ell} = \frac{A_{u\ell} \beta_{u\ell} h\nu_{u\ell}}{\sum_\ell A_{u\ell} \beta_{u\ell} h\nu_{u\ell}} \quad (4.20)$$

The factor $h\nu_{u\ell}$ has to be introduced, since we consider energy packets rather than individual photons.

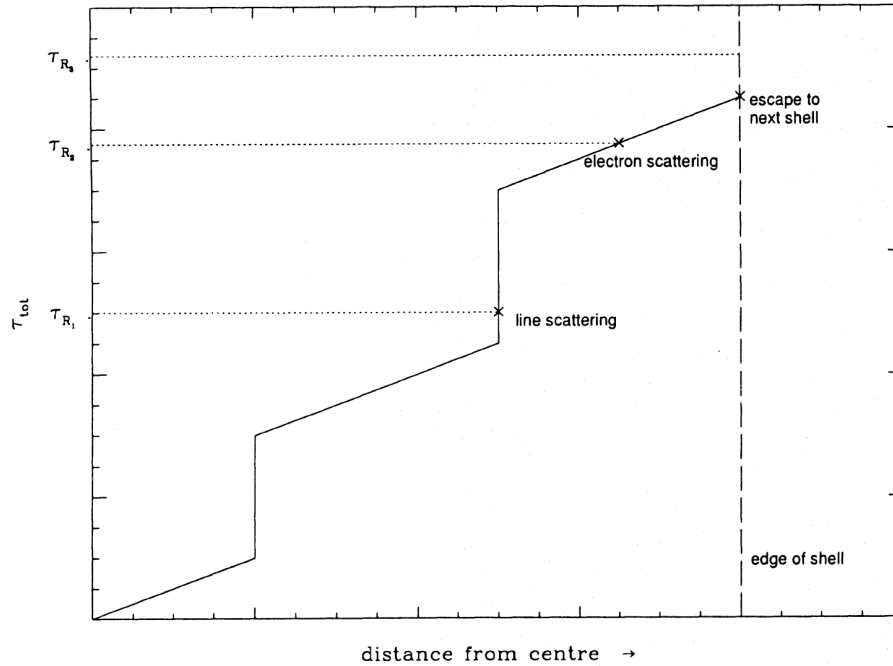


Figure 4.2.: Photon encounters line and scattering events during its flight through a model shell (Mazzali & Lucy 1993).

Figure 4.2 sketches the MC procedure showing the sum of all τ_i as the packet travels through a shell, encounters a sample line event, and is scattered by an electron before it escapes the shell.

If the number of packets used is sufficiently large, the distribution of the re-emitted packets in the various lines becomes rather accurate. Again, since the packet's energy in the co-moving frame is conserved so is the total luminosity during the modelling procedure.

Following the event history of about 10,000 packets is usually sufficient to avoid random noise and to converge the radiation field iteration.

Line absorption rate

In order to calculate the emergent spectrum via the formal integral solution we need to know the line absorption rate from the radiation field.

After a line has absorbed an energy packet and the ion is in an excited state u , $4\pi j_k$ denotes the effective emissivity of the k th transition of all permitted decays

$u \rightarrow i$. Then the fraction of energy emitted by level u that escapes via the k th branch is

$$q_k = j_k / \sum_m j_m \quad (4.21)$$

Since the entire energy ϵ in the co-moving frame of a packet is absorbed by a line, we can give an estimate for the rate per unit volume at which energy is removed from the radiation field by excitations $\ell \rightarrow u$:

$$\dot{E}_{\ell u} = \frac{\epsilon_0}{\Delta t} \frac{1}{V} \sum \frac{\epsilon}{\epsilon_0} \quad (4.22)$$

where *only* these packets contribute to the summation which are actually interacting with this particular line in volume element V . The statistical accuracy can be increased by modifying the estimator:

$$\dot{E}_{\ell u} = \frac{\epsilon_0}{\Delta t} \frac{1}{V} (1 - e^{-\tau_{\ell u}}) \sum \frac{\epsilon}{\epsilon_0} \quad (4.23)$$

The term $(1 - e^{-\tau_{\ell u}})$ denotes the probability that a photon redshifted to frequency $\nu_{u\ell}$ is absorbed by the line, where $\tau_{\ell u}$ is the Sobolev optical depth. In this case the summation extends over *all* packets in V which encounter the frequency $\nu_{u\ell}$ at some time during the MC experiment. Therefore, $\dot{E}_{\ell u} > 0$ even if no packet is absorbed or emitted by this line at any time in the calculation.

4.2.5. Emergent spectrum

The last step is to calculate the emergent spectrum. This is done by solving the formal integral for the emergent intensity but using line and continuum source functions derived from the MC experiment.

Noise-free SN spectra can be computed by incorporating Sobolev theory into a formal integral calculation of the luminosity density L_ν (e.g. Lucy 1991). For this purpose the source functions or equivalently the level populations have to be known. In fact, if we treat the level populations in NLTE, the formal integral solution is preferable to the MC approach. One could even think of eliminating the MC calculation completely and instead of simply computing the emergent spectrum from the formal integral using the source function obtained from the modified nebular approximation described in Section 4.1.3. However,

the resulting spectrum differs significantly from the corresponding MC spectrum and it is further from the real spectrum than the MC experiment.

To be more precise, we know that for some ions a normal level u can be overpopulated. In the above hypothetical formal integral calculation the error increases emissivities for all transitions $u \rightarrow \ell$ resulting in emission bumps in the emergent spectrum. On the other hand, in the MC procedure emissions $u \rightarrow \ell$ only occur if level u is excited by an absorption from the ground-state or other low-lying (mostly metastable) levels. The populations of the levels are typically much more reliably known.

Line source function

The general expression for the line source function after the level populations are determined in NLTE is (Mihalas 1978):

$$S_{u\ell} = \frac{A_{u\ell} n_u}{B_{\ell u} n_\ell - B_{u\ell} n_u} \quad (4.24)$$

Since our calculation is not carried out in NLTE, we use first the line's effective emissivity in the Sobolev approximation:

$$4\pi j_{u\ell} = A_{u\ell} n_u h\nu_{u\ell} \beta_{u\ell} \quad (4.25)$$

where the escape probability $\beta_{u\ell}$ is defined in Equation 4.18. The line emissivity in a SN envelope follows immediately from Equations 4.24 and 4.25, together with the Sobolev optical depth $\tau_{u\ell}$ (Eq. 4.19):

$$4\pi j_{u\ell} = \frac{4\pi}{\lambda_{u\ell} t} (1 - e^{-\tau_{u\ell}}) S_{u\ell} \quad (4.26)$$

The line source function can then be computed via the following steps:

1. The total rate per unit volume at which energy is absorbed in exciting level u using Equation 4.23 is given by:

$$\dot{E}_u = \sum_{i < u} \dot{E}_{iu} \quad (4.27)$$

2. A fraction $q_{u\ell}$ of this absorbed energy escapes via the branch $u \rightarrow \ell$, and the effective line emissivity becomes:

$$4\pi j_{u\ell} = q_{u\ell} \dot{E}_u \quad (4.28)$$

3. Finally, the line source function $S_{u\ell}$ is obtained by substituting this value of $4\pi j_{u\ell}$ into Equation 4.26.

Continuum source function

In order to calculate the formal integral line transitions and electron scattering must be considered. Hence the corresponding source function for electron scattering, which is the mean intensity in the co-moving frame, must be derived. The co-moving mean intensity of the incident radiation in the far blue wing of the transition $\ell \rightarrow u$ is $J_{\ell u}^b$. Thus, $\beta_{\ell u} J_{\ell u}^b$ is given as the mean intensity of the partially attenuated incident radiation averaged over the line profile. The rate at which energy is removed from the radiation field is:

$$\dot{E}_{\ell u} = (B_{\ell u} n_{\ell} - B_{u\ell} n_u) \beta_{\ell u} J_{\ell u}^b h\nu_{\ell u} \quad (4.29)$$

If this formula is combined with Equations 4.24 and 4.25 and since the values of $\dot{E}_{\ell u}$ are given by Equation 4.23, $J_{\ell u}^b$ can be computed from:

$$\dot{E}_{\ell u} = \frac{4\pi}{\lambda_{u\ell}} (1 - e^{-\tau_{\ell u}}) J_{\ell u}^b \quad (4.30)$$

Given the velocity law in the SN envelope $v = r/t$, Lucy (1971) showed that $J_{\ell u}^r$, which is the corresponding quantity in the extreme red wing of the transition, can be derived from Sobolev theory via the formula:

$$J_{\ell u}^r = J_{\ell u}^b e^{-\tau_{\ell u}} + S_{u\ell} (1 - e^{-\tau_{\ell u}}) \quad (4.31)$$

Therefore, the mean intensities in the blue and red wings of every line in the line list can be derived. They have non-zero values if at least one packet came into resonance with the line at any time during the calculation, even though it is not necessary that any excitation $\ell \rightarrow u$ actually occurs.

Formal integral

A line of sight intersects the SN envelope with impact parameter p . If $I_\nu(p)$ is the limiting specific intensity at rest frequency ν on that line of sight, then the luminosity density is given by:

$$L_\nu = 8 \pi^2 \int_0^\infty I_\nu(p) p dp \quad (4.32)$$

The beam intensity can be incremented either by line interaction or by electron scattering between two consecutive resonances. Both contributions have to be known in order to compute I_ν . According to Equation 4.31, the line formation increment at resonance frequency ν_k is given by:

$$I_k^r = I_k^b e^{-\tau_k} + S_k (1 - e^{-\tau_k}) \quad (4.33)$$

with the same notation and superscripts as before.

Electron scattering contributes between the k and $(k + 1)$ th resonance with:

$$I_{k+1}^b = I_k^r + \Delta\tau_e (J_{k,k+1} - I_k^r) \quad (4.34)$$

where $\Delta\tau_e (\ll 1)$ is the electron scattering optical depth along that segment and $J_{k,k+1}$ denotes the average co-moving mean intensity along the same way. $J_{k,k+1}$ is approximated by:

$$J_{k,k+1} = \frac{1}{2} (J_k^r + J_{k+1}^b) \quad (4.35)$$

with the quantities in parentheses derived from Equation 4.31.

The following initial conditions are required to solve Equations 4.33 and 4.34 recursively: I_1^b if $p > R$ and $I_m^b = B_\nu(T_B)$ if $p < R$, where m is the first transition in the line list with its resonance point sitting above the lower boundary $r = R$.

That procedure results in a much more realistic and noise-free spectrum than we would obtain by simply binning the escaped photons according to their frequency unless we used a very large number of packets. Before that spectrum can be compared with observations, a suitable reddening law has to be applied and we must correct for the attenuation due to the distance of the SN.

4.3. The modelling procedure

The new internal procedure to handle the abundance distribution in the MC calculation is explained in detail in Section 5.2. Here we focus on the general approach of calculating synthetic spectra of SNe Ia with the MC code.

The density profile is taken from the W7 model (Nomoto et al. 1984) scaled to the given epoch. The remaining input parameters are either given by the observations or need to be fixed iteratively during the computational runs. The number of free parameters changes depending on the available information about a specific SN. For a given SN distance, epoch and reddening $E(B - V)$ are often known observationally. In a first iteration the photospheric radius is set to reproduce the line velocities in the spectrum and the luminosity to fit the total flux of the observation. In a second iteration the abundance distribution is modified, the starting point of which is usually the W7 distribution. The chemical composition for each model is adapted iteratively to the particular spectrum.

With this input synthetic spectra are calculated individually and independently to fit the observed spectra. However, if the observed spectra were taken in rapid succession (every 2 days or less) spectral synthesis models are connected and later epochs are constrained by earlier ones because the input parameters v_{ph} and L_{ph} must evolve smoothly. The abundances, which are derived from each spectrum above its photosphere, are constrained in a more natural manner. As explained in detail in Section 5.2 the abundances at the velocities right above the photosphere of each epoch are fixed. This limits the freedom for the abundances in the following epochs to regions of lower velocity than the previous photosphere.

5. Abundance Tomography of Type Ia Supernovae

We see how we may determine their forms, their distances, their bulk, their motions, but we can never know anything of their chemical or mineralogical structure. ... We must keep carefully apart the idea of the solar system and that of the universe, and be always assured that our only true interest is with the former. ... The stars serve us scientifically only as providing positions.

*Auguste Comte (1798-1857),
Course of Positive Philosophy*

After the discussion of the structure of the MC code in the previous Chapter, we now introduce a new method of analysing SNe Ia spectra called “*Abundance Tomography*”. The Chapter is organised in two main parts. First the importance of the method and its realisation within the MC code are explained. Then this method is applied to a complete spectral analysis of the normal SN Ia 2002bo. For this purpose, we not only compute models for the early phase but also include spectral synthesis models of the nebular phase. Therefore, we can derive the abundance distribution in the whole ejecta of that object.

5.1. Stratified abundances in supernovae

Thermonuclear burning and nucleosynthesis in SNe Ia depend on many properties defining the physical conditions in the ejecta. The most important quantities are the temperature and the density at the burning front, the electron fraction Y_e ,

and the composition of the fuel (C/O ratio). Since the conditions vary between different points in the ejecta due to asymmetries in the configuration, but also because of time-dependent changes due to the fast expansion of the SN envelope, the burning process and therefore the abundances of the synthesised elements differ significantly with spacial coordinates. It is very unlikely to think of a fully mixed SN ejecta, where the abundances are distributed homogenously throughout the envelope. Since the main parameters like temperature and density to first order change with the radius, the main macroscopic variance is expected to be seen with increasing distance to the centre. Despite significant differences in the final distribution of the elements, all explosion models predict a somewhat layered structure after the SN has reached the state of homologous expansion a few seconds after the explosion (e.g. Iwamoto et al. 1999).

All these models have in common that they predict three main zones with respect to the radius, each of them dominated by certain chemical species. Near the center, where temperature and density are highest, all C and O is burned to NSE leading to a core that consists only of Fe group elements, mainly ^{56}Ni or stable Fe isotopes. This zone extends to about 8000 km s^{-1} depending on the object. The exact ratios depend on the electron fraction at the time of the burning, because that constrains the neutron excess in the synthesised nuclei due to electron capture. As regions of lower densities are reached, the burning is incomplete and the abundances are dominated by intermediate mass elements, mostly Si, S, Mg, and Ca. Depending on the power of the explosion, a thinner or thicker layer of unburned material (C and O) is left over in the outer regions of the SN ejecta. These predictions of the explosion models have not yet been confirmed spectroscopically, since spectral synthesis analyses used homogenous abundance distributions so far.

Apart from this general behaviour we might see effects arising from asymmetries like rotation or off-center ignition, which lead to blobs or bubbles of different abundances (e.g. Kasen et al. 2003).

Whether different abundance distributions, caused by different initial conditions of the explosion or by asymmetries, completely explain the diversity of SNe Ia is not yet clear, but they certainly play a key role in the understanding of the SNe Ia phenomenon. The access to the answer of that question is provided by the analysis of the spectra using stratified abundances in the SN envelope.

5.2. Abundance Tomography

Several analyses proved the ability of the MC code to deal with the physics of different kinds of SNe Ia (e.g. SN 1990N, Mazzali et al. 1993; SN 1991T, Mazzali et al. 1995). Nevertheless, there are some shortcomings. For example, the approximation that the inner boundary is the photospheric radius becomes less valid as the SN expands and it fails at epochs later than ≈ 10 d after maximum light. Another shortcoming of the MC code as explained in Chapter 4 is the use of homogenous abundances.

In addition to the discussion in Section 5.1 about the importance of stratified abundances from the physical point of view, a homogenous distribution also causes problems in calculating synthetic spectra. Lines are formed throughout the entire ejecta. However, most of the line formation occurs in a rather narrow region ($\approx 2000 \text{ km s}^{-1}$) just above the photospheric radius. Because of the steep decline of the density with increasing radius ($\rho \propto v^{-7}$ for the W7 model, Nomoto et al. 1984), shells further out do not contain enough material to absorb radiation significantly. But density is not the only factor that controls line formation. Temperature has strong influence on the ionisation structure and therefore on the line absorption. This has significant impact on the MC calculation. Since the temperature is higher in the inner part of the SN envelope, more highly ionised species dominate the composition. Strong lines of e.g. Si III or Fe III are the consequences, if the abundances of these species are enhanced in the model in order to reproduce the typically deep absorption features of Si II and Fe II. These lines from doubly ionised species are usually rather weak or even completely absent in the observed spectra.

In order to address these issues, a stratified abundance distribution has been implemented in the MC code. An additional shell structure is set up where the shell boundaries are given by the photospheric radii of the observed spectra. Therefore, the size of the shells is not fixed a priori but is set during the model calculations. As explained in Section 4.3 this radius is an input parameter which is adapted to the actual situation. The earliest spectrum is always the starting point. A homogenous abundance distribution above this first photosphere is assumed, or a number of supplementary shells (typically ≤ 3) may be introduced at higher velocities. An optimal model is then computed and its chemical composition as well as the velocities of the boundaries of the abundance shells

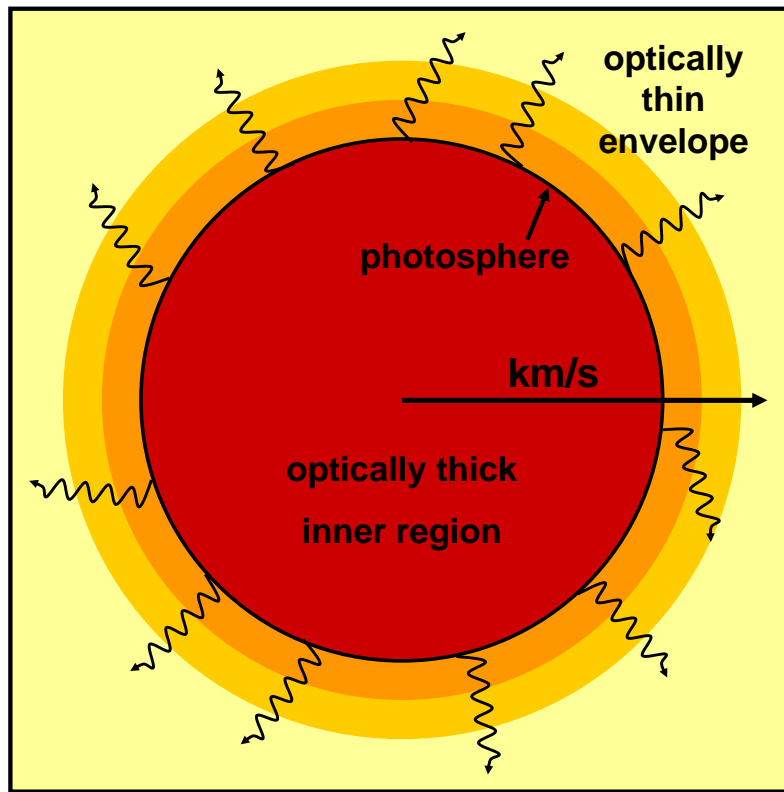


Figure 5.1.: Schematic plot of the concept of Abundance Tomography. The outer shells (orange and light yellow) are defined by consecutive spectra in the time series for which the abundances are determined (s. text).

are stored. At the epoch of the next spectrum in the time series of the object the photospheric velocity has decreased. The SN envelope has expanded, the density has become lower between the two epochs at a fixed velocity and therefore light is detected that had been emitted from deeper in the ejecta. Although the physical conditions (density, temperature, etc.) have changed in our previously considered shells, the relative abundances are unchanged, except for the radioactive elements ^{56}Ni and ^{56}Co and the stable end product ^{56}Fe , for which the intervening decay is taken into account. Consequently, only one new abundance shell is introduced, with boundaries given by the two photospheric velocities of the previous and the present model. The abundances in the new shell are set so as to achieve the best fit for the new spectrum, while the previously determined abundances in the outer shells are retained. Figure 5.1 sketches this procedure.

The optical thick region (red) in the inner region does not influence the spectrum. Each shell above the photosphere (orange to light yellow) represents an abundance layer that is determined by the photospheres of two consecutive spectra in the time sequence.

This procedure is carried out until all photospheric-phase spectra are modelled, yielding an abundance profile of the object. The details and the amount of information that can be derived from such an “Abundance Tomography” clearly depend on the number of spectra that are available and on the size of the time steps between each of them. Physical conditions in the first 8 – 10 days after the explosion change very rapidly compared to later epochs and information about the progenitor and possible interaction with circumstellar environment is contained in the outermost layers of the SN ejecta. Therefore, high-quality Abundance Tomography can be achieved if many very early observations are available, while a high frequency of observations near maximum light is less necessary.

5.3. Abundance Tomography: The case of SN 2002bo

In this Section we analyse the spectra and light curve of SN 2002bo in some detail. The analysis is based on data that were obtained by the European Research Training Network (RTN) on “The Physics of Type Ia Supernova Explosions”, also called the European Supernova Collaboration (ESC). This collaboration has the aim to study a sample of very nearby supernovae by means of very good time series of multi-wavelength observations and detailed models. SN 2002bo was our first target (Benetti et al. 2004b).

In Section 5.3.1 the observational campaign of SN 2002bo is presented with focus on the early time spectra that are analysed in this work. A brief analysis of the early IR spectrum at day -8.5 is given in Section 5.3.2. The results can be used to set an upper limit on the C content of SN 2002bo (Section 5.3.3). Detailed information about the modelling of the photospheric epoch spectra are given in Section 5.3.4, whereas Section 5.3.5 treats the nebular spectra modelling. With this knowledge the abundance distribution of SN 2002bo from the centre out to velocities of about $40,000 \text{ km s}^{-1}$ is discussed in Section 5.3.6. A comparison of line velocities with other objects is made in Section 5.3.7. Finally,

in Section 5.3.8 the synthetic light curve calculated on the basis of the derived abundance distribution is presented and discussed.

5.3.1. Observations

SN 2002bo was discovered independently by Cacella and Hirose (Cacella et al. 2002) on March 9.08 UT and March 9.505. It is located in NGC 3190 at a distance modulus $\mu = 31.67$ ($H_0 = 65 \text{ km s}^{-1} \text{ Mpc}^{-1}$). 13 different telescopes and instruments of the ESC were involved in the photometric and spectral observations between ~ 13 days prior to the estimated epoch of B maximum and 368 days after. It was rather complicated to combine the measurements from so many various instruments to achieve a consistent picture of the spectral evolution of SN 2002bo. Nevertheless, observations provide us with an excellent set of 21 optical spectra, 13 of which also include near-infrared wavelengths, as well as 11 infrared spectra throughout the entire photospheric period until well into the nebular phase (see Fig. 5.2). Table 5.1 summarises the optical and near-infrared spectra actually used for modelling. At some epochs multiple observations were carried out and the best one is picked as explained in Section 5.3.4.

Benetti et al. (2004b) quote a value for the extinction $E(B - V)_{obs} = 0.43 \pm 0.10$. However, a parameter study carried out with synthetic spectra and also presented in Benetti et al. (2004b) indicates a lower value for the reddening. The highest value that is acceptable from the parameter study is $E(B - V)_{mod} = 0.38$ which is used for the calculations in this work. This value lies well within the error range of $E(B - V)_{obs}$. Observations suggested a B band rise time of 17.9 ± 0.5 d, a decline rate $\Delta m_{15}(B) = 1.13 \pm 0.05$, and a dereddened $M_B = -19.41 \pm 0.42$, making SN 2002bo a typical “Branch normal” type Ia supernova (Branch et al. 1993). However, comparison with other SNe Ia reveals peculiarities of SN 2002bo e.g. with respect to line velocities. These topics are addressed later in this Section. Table 5.2 summarises the main parameter values of SN 2002bo obtained from the observations. Further details about all observational details are presented in Benetti et al. (2004b).

5.3.2. Model of the early IR-spectrum at day -8.5

The modelling of the early IR-spectrum originates from an earlier analysis, published in Benetti et al. (2004b). At that time we used the non-stratified version of

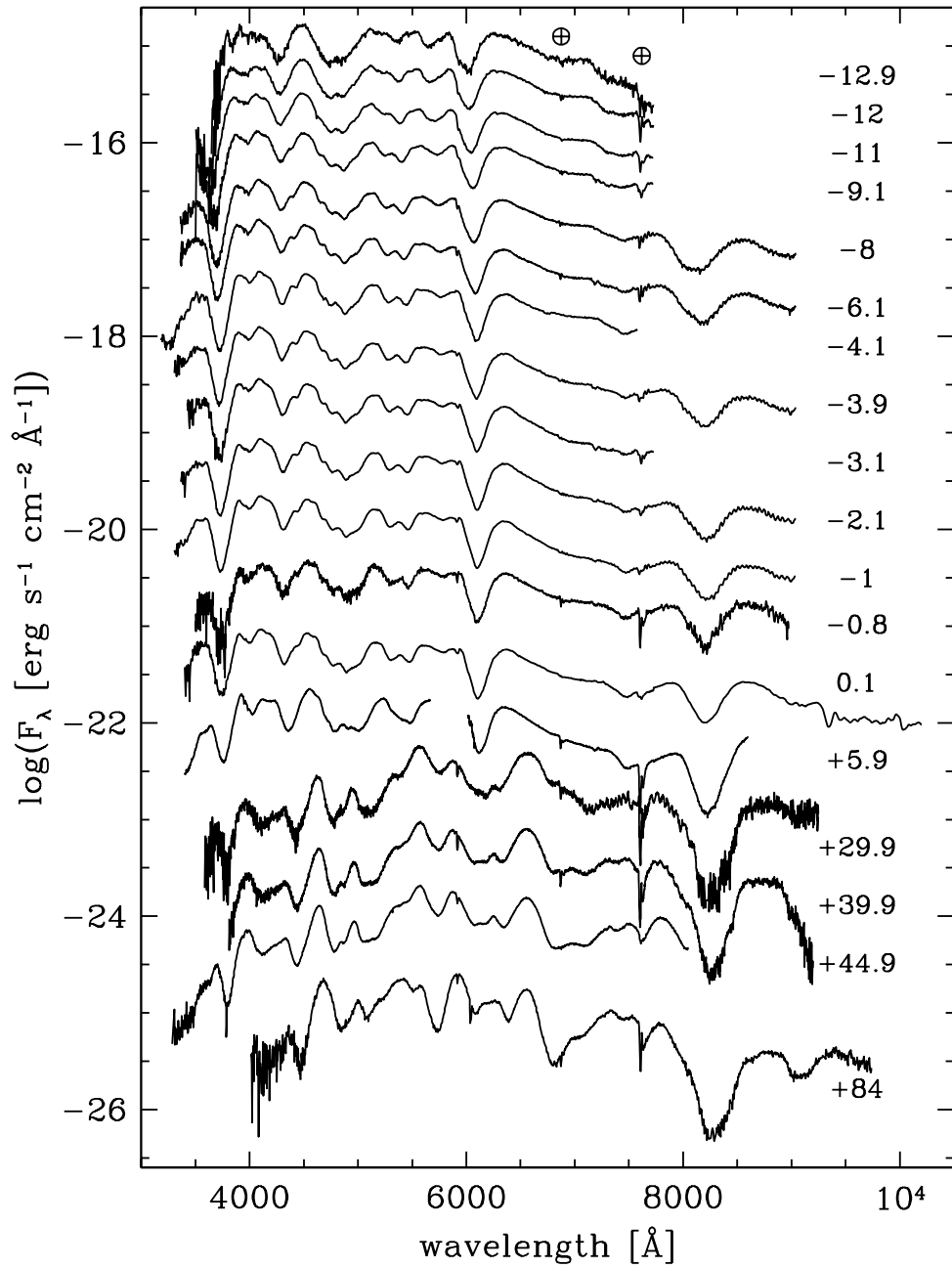


Figure 5.2.: Spectral evolution of SN 2002bo. Wavelength is given in the observer frame. The ordinate refers to the first spectrum and the others have been shifted downwards. Epochs are shown to the right of each spectrum. The \oplus symbols mark the main telluric features.

Table 5.1.: Spectroscopic observations of SN 2002bo used for model calculations

Date	M.J.D.	Epoch* (days)	Range (Å)	Tel.	Res. (Å)
10/03/02	52343.06	-12.9	3600-7700	A1.82	25
10/03/02	52343.99	-12.0	3600-7700	A1.82	25
11/03/02	52344.99	-11.0	3400-7700	A1.82	25
13/03/02	52346.91	-9.1	3400-7700	A1.82	25
15/03/02	52348.04	-8.0	3400-9050	NOT	14
16/03/02	52349.93	-6.1	3400-9050	NOT	14
18/03/02	52351.85	-4.1	3200-7550	WHT	2
19/03/02	52352.02	-4.0	3400-7700	A1.82	25
19/03/02	52352.05	-3.9	3400-9050	NOT	14
19/03/02	52352.94	-3.1	3400-7700	A1.82	25
20/03/02	52353.90	-2.1	3400-9050	NOT	22
21/03/02	52354.96	-1.0	3400-9050	NOT	22
23/03/02	52356.08	+0.1	3400-10350	A1.82	25
28/03/03	52361.94	+5.9	3100-8800	WHT	12
11/12/02	52619.34	+263	3350-7400	E3.6	14
26/03/03	52724.10	+368	3600-8600	VLT	11

* - relative to the estimated epoch of B maximum (MJD=52356.0)

A1.82 = Asiago 1.82m Telescope + AFOSC

NOT = Nordic Optical Telescope + ALFOSC

WHT = William Herschel Telescope + ISIS

E3.6 = ESO 3.6m Telescope + EFOSC2

VLT = ESO-VLT-U1 Telescope + FORS1

the code. Nevertheless, the results are still valid, since the main purpose of the analysis was to test the outer ejecta on its C content. The stratified model could only reduce our upper limit presented in the following Section.

We have carried out a comparison of model spectra with the observations in the infrared region. Unfortunately there are no infrared observations available at day -12.9 , when the spectral model is more applicable at such long wavelengths. The earliest IR-spectrum is from day -8.5 . Therefore, in order to examine the $8000 - 25,000 \text{ \AA}$ region, we scaled the flux of the -12.9 d model by $\times 1.4$ to bring it to the flux level of the observed spectrum from day -8.5 . The IR spectrum is shown in Figure 5.3, together with the model spectra for two values of the carbon abundance (see Sect. 5.3.3). In general there is reasonable agreement between the models and the observations with respect to the overall shape of the IR

Table 5.2.: Main parameter values of SN 2002bo and its host galaxy

Parent galaxy	NGC 3190
Galaxy type	SA(s)a pec sp LINER [†]
RA (2000)	10 ^h 18 ^m 06 ^s .51
Dec (2000)	+21°49′41″.7
Recession velocity [km s ⁻¹]	1405 [‡]
Distance modulus (H ₀ = 65)	31.67
E(B – V)	0.43 ± 0.10
Offset from nucleus	11″.6E 14″.2S
Explosion epoch (MJD)	52338.1 ± 0.5 (Mar 05, 2002)
Date of B maximum (MJD)	52356.0 ± 0.5 (Mar 23, 2002)
Magnitude at max	B = 14.04 ± 0.10, V = 13.58 ± 0.10, R = 13.49 ± 0.10, I = 13.52 ± 0.10
Δm ₁₅ (B)	1.13 ± 0.05

[†] NED

[‡]LEDA, corrected for LG infall (208 km s⁻¹)

spectra. In the 8000 – 13000 Å window we identify features due to the Mg II 9217,9243 Å doublet and the 10914,10915,10952 Å triplet. Additionally there is a Si II feature of minor importance at 9413 Å. In the 15,000 – 18,000 Å window we attribute the broad absorption at 16,000 Å in the figure to a blend of Si II 16,906 Å, 16,977 Å, 17,183 Å and Mg II 16,760 Å, 16,800 Å, with the Si II feature dominating. Thus, at this early epoch we confirm the IR identifications proposed by Marion et al. (2003) for their spectra of other SNe Ia. Marion et al. (2003) point out that the Mg II IR features are valuable for placing limits on the mass of unburned material. In the 20,000 – 25,000 Å line region no strong features were observed in the spectrum nor were predicted by the model. There is only a shallow, broad P-Cygni feature at ~20800 Å which we attribute to Si II. Marion et al. (2003) did not cover this spectral region.

5.3.3. Is there carbon in SN 2002bo?

One reason that early-time spectra are of particular interest is because, via the strength of C II lines in the red part of the spectrum, they can provide interesting limits on the amount of carbon present, and how far into the outer layers the burning penetrated. The carbon abundance at extremely early times may even

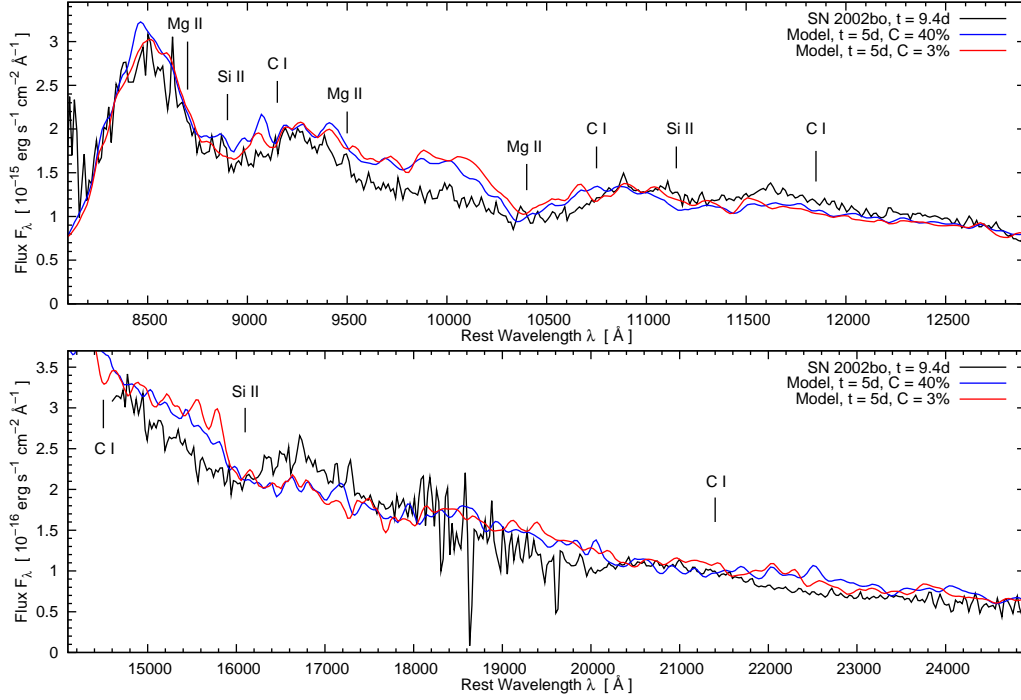


Figure 5.3.: Near-infrared spectrum of SN 2002bo. The -12.9 d model has been scaled to the flux level of the observations at day -8.5 before B_{max} . Also shown are two spectral models with carbon abundances of 3% and 40% respectively (see text).

reveal the properties of the progenitor white dwarf. Fisher et al. (1997) suggested that the entire ‘Si II’ 6150 Å absorption feature in the -14 d spectrum of SN 1990N was actually C II 6578,83 Å at high velocity. However, Mazzali (2001) showed that this line could, at most, be responsible for only the red side of the 6150 Å feature, as indicated by its presence as a weak absorption at lower velocities sitting on top of the P-Cygni emission of the Si II line, and by the weakness of the corresponding C II 7231,36 Å line. Branch et al. (2003b) identified absorption features due to C II 6578,83 Å and C II 7231,36 Å in the -9 d spectrum of SN 1998aq. They are also clearly visible in the -10 d spectrum of SN 1994D (Patat et al. 1996, Hernandez et al. 2000), although by -8 d they had almost disappeared. However, in SN 2002bo there is no trace of these features, even in the earliest spectra. In order to place limits on the abundance of high velocity C implied by this negative observation, we increased the 7% carbon relative abundance specified by W7, to 40% throughout the envelope. This produced very strong

C II 6578,83 Å features which were not present in the observed spectrum. We then decreased the carbon abundance until the C II 6578,83 Å features became fully undetectable in the synthetic spectrum. This occurred for a C abundance of 3%.

As a check, we extended the modelling to 25,000 Å where C I and C II lines are found in the model line list. These include multiplets around 9,100 Å, 10,680 Å, 11,750 Å, 14,400 Å and 21,200 Å plus several single lines distributed throughout the 8000 – 25,000 Å region. Figure 5.3 shows the IR spectrum plus the 40% carbon and 3% carbon models. It can be seen that even with a 40% carbon abundance, the carbon features are barely discernable. However, the observed spectrum shows no sign whatever of the predicted carbon features confirming that the carbon abundance is less than 40%. Reducing the carbon abundance to 3% causes the lines in the 8000 – 25,000 Å region to become too weak or too blended with other lines (mostly Si II or Mg II) to be detectable. We conclude that the IR spectrum is consistent with a 3% carbon abundance, although the actual limit here is less stringent than in the optical region. We note that, aside from the low abundance, the weakness of the C I lines is due to the temperature of the SN ejecta which leads to an almost complete ionisation to C II.

5.3.4. Spectral Analysis

Observations of SN 2002bo provide us with an excellent set of 17 optical spectra, 8 of which extend to the near-infrared, and 2 infrared spectra, covering the period from –12.9 d until +5.9 d relative to *B* maximum. Therefore, both conditions for the optimal application of the “Abundance Tomography” procedure, a closely meshed spectral sequence and very early epochs, are fulfilled.

The early infrared spectrum was already discussed in Section 5.3.2 and is not included here. For three of the epochs, multiple observations at different telescopes were carried out. On day –4 there are even three spectra available. Two of these (–4.1 and –3.9) are analysed, while the observation at –4.0 days was not, for reasons discussed in Section 5.3.4. For day –2 and day –1 the spectrum with larger wavelength coverage and better resolution is included. In this Section the analysis of each individual spectrum that was modelled is presented in chronological order.

General parameters that apply for all spectra are the distance, $\mu = 31.67$, the

Table 5.3.: Input parameters and converged T_{BB} of photospheric models.

Epoch* (d)	Epoch** t_{exp} (d)	Radius v_{ph} (km s ⁻¹)	Bol. Lum. $\log_{10}L$ (erg s ⁻¹)	Temp. T_{BB} (K)
-12.9	5.1	15,800	42.04	9430
-12.0	6.0	15,500	42.31	9950
-11.0	7.0	15,100	42.54	10,930
-9.1	8.9	13,900	42.77	11,850
-8.0	10.1	12,900	42.84	12,330
-6.1	11.9	11,450	42.97	13,070
-4.1	13.9	10,400	43.04	13,310
-3.9	14.1	10,200	43.05	13,480
-3.1	15.0	9900	43.08	13,420
-2.1	15.9	9200	43.09	13,820
-1.0	17.0	8600	43.10	13,940
+0.1	18.1	8100	43.09	13,750
+5.9	24.0	7600	43.08	10,940

* relative to the estimated epoch of B maximum (MJD=52356.0)

** days after the explosion.

epoch, which we derived from a bolometric rise time of 18 d, and the reddening, $E(B - V) = 0.38$ as discussed in Section 5.3.1. Table 5.3 summarises the individual input parameters and the effective temperature T_{eff} obtained from the analysis for each spectrum, respectively.

a) Day -12.9

The first spectrum in the sequence was taken 12.9 days before maximum light, which corresponds to an epoch of $t_{exp} = 5.1$ d. This is one of the earliest SNe Ia spectra ever taken. The luminosity that is radiated at the photosphere is $\log_{10}L = 42.04$ (erg s⁻¹) at a photospheric radius $v_{ph} = 15,800$ km s⁻¹. Such a high velocity is necessary in order to achieve a low effective temperature. Fig. 5.4 shows the observed spectrum together with the best fit model.

The most prominent lines are labelled. (All lines are labelled with their rest wavelength.) Several deep absorptions dominate the spectrum. Most of them are present throughout the entire photospheric phase. These are marked and identified in the spectra. The bluest feature, near 3700 Å, is the Ca II H&K doublet (3934 Å & 3968 Å) followed near 4200 Å by Mg II 4481 Å. The next absorption

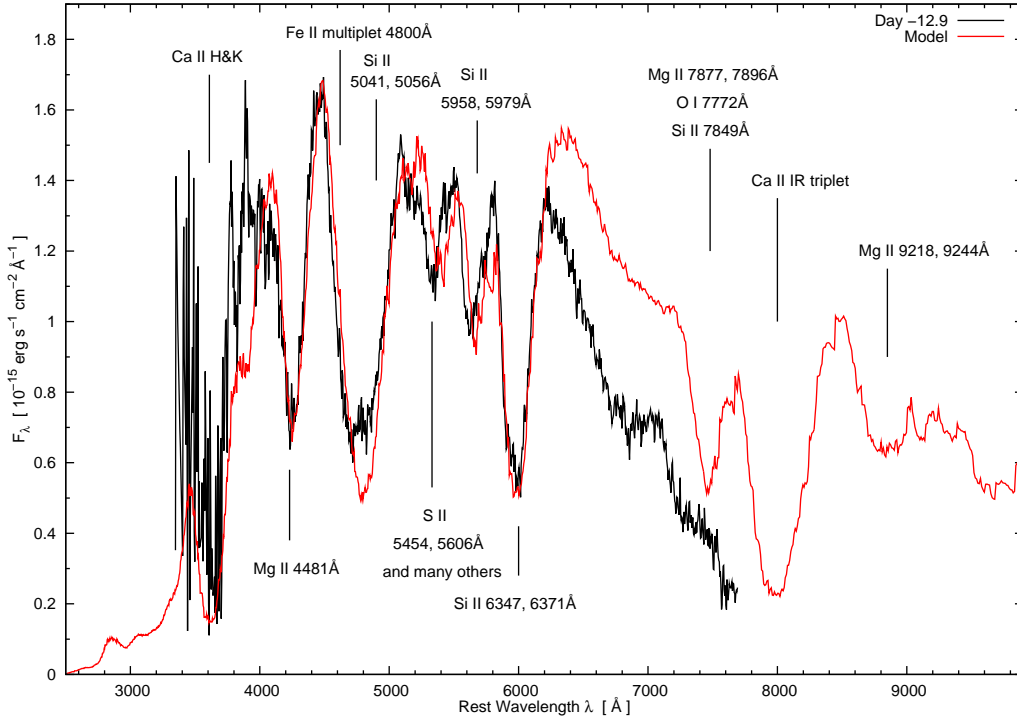


Figure 5.4. Observed spectrum and corresponding model of SN 2002bo at day -12.9 using $E(B - V) = 0.38$, $\mu = 31.67$, $t_{exp} = 5.1$ d.

feature to the red (~ 5000 Å) is a combination of several Fe II lines (4924 Å, 5018 Å, 5169 Å) and two Si II lines (5041 Å & 5056 Å). Next, at ~ 5300 Å, is the S II complex (most prominent are 5454, 5606 Å), followed at ~ 5700 Å by the weaker Si II feature (5958, 5979 Å) and by the stronger Si II lines (6347, 6371 Å) at ~ 6000 Å. The near-infrared (NIR) region is dominated by a composed feature of O I (7774 Å), Si II (7849 Å) and Mg II (7877 Å & 7896 Å) near 7500 Å, and by the Ca II IR triplet (8498 Å, 8542 Å, 8662 Å) at ~ 8000 Å. Further to red another strong Mg II feature (9218, 9244 Å) is detected. Since there is only one optical spectrum that extends to these wavelengths (day +0.1) lines beyond the Ca II IR triplet are subject of the infrared analysis and are not followed here. One immediately notices the flat overall shape of the spectrum, which is indicative of a low temperature, and the steep fall of the flux redwards of the Si II line at ~ 6371 Å.

There are two line signatures that restrict the temperature to the regime of ~ 7500 K. First the depth of the absorption at around 5640 Å which is due to a

blend of S II lines. These lines disappear if the photospheric velocity is decreased because if the temperature rises S is ionised to S III. Secondly, the ratio of the two Si II lines at 5970 Å and 6355 Å is a reliable temperature indicator. The smaller the ratio the hotter the environment (Nugent et al. 1995b). SN 2002bo shows a large ratio at this epoch, which indicates a low temperature. This is not surprising, since the SN is still relatively dim at this epoch, and the ejecta are dense, leading to a high photospheric velocity and consequently a low temperature, which will increase with time. Comparing the model with the observations may suggest an even lower temperature since the synthetic spectrum under reproduces the 5970 Å line but over reproduces the 6355 Å line. However, trying to achieve this by further increasing the radius causes other problems. First, a lower temperature leads to an additional shift of the flux to the NIR region, which is not seen in the data. Second, the density drops rapidly below a critical value at higher velocities and there is not enough material above the photosphere to produce the observed lines.

The deep absorption near 4800 Å is a mixture of mostly Fe II and Si II lines, where the Si lines are concentrated in the blue part (5041 Å and 5056 Å) and the Fe lines are distributed all over the feature (4924 Å, 5018 Å and the strongest one at 5169 Å). In order to reproduce this feature two “patches” had to be implemented. An additional shell was introduced above 22,700 km s⁻¹. This shell occupies the complete outer region of the SN ejecta and contains enhanced abundances of Si and Ca at the expense of O. Namely there is 55% of Si and 5.5% of Ca by mass. These abundances are necessary to reproduce the blue wings of the lines of these elements. The shell between 15,800 km s⁻¹ and 22,700 km s⁻¹ contains remarkably high abundances of IME and Fe group elements. Both shells contain 1.5% stable Fe, 1.13% of radioactive components (⁵⁶Ni, ⁵⁶Co, ⁵⁶Fe) and 0.02% of Ti and Cr. The S abundance remains constant at 6% in both shells while Si decreases to 30% and Ca to 0.32% in the inner shell.

The feature at ~ 4200 Å is mostly Mg at this epoch and requires a high abundance of this element. Both outer shells consist of 30% Mg in order to give the Mg II line at 4481 Å the correct strength. At shorter wavelengths than the Mg feature the observations reach a regime of low signal-to-noise and cannot be trusted completely. Nevertheless, it is important to note that owing to the high abundance of Fe group elements the flux in this region is suppressed almost totally and is transferred to redder wavelengths. The model shows Ca II H&K,

with a strength which is not in contradiction with the data.

SN 2002bo shows no sign of C, even at high velocities. In Section 5.3.2 the early IR spectrum was modelled and analysed by looking for C lines in Section 5.3.3. From this analysis we can set an upper limit for the C abundance of 3% restricted to velocities $> 25,000 \text{ km s}^{-1}$. Since no C is found at later epochs, which would be expected if C was mixed with IME during the burning process and therefore moved to deeper layers, we can conclude that all the C (but not the O) from the WD was burned to IME during the explosion phase.

The main shortcoming of the model is the overestimate of the flux beyond the deep Si II absorption at 6355 \AA . Since the epoch of this spectrum is so early that the assumption of a photospheric radius should be essentially correct, it is possible that data calibration may be the reason for the mismatch of the flux. One can see from the figure that the relevant region ($6200 \text{ \AA} - 7700 \text{ \AA}$) is close to the edge of the observation. This makes it usually difficult in the data reduction when aligning the different wavebands to each other. Since models of other SNe Ia at this early phase do not suffer from this problem, but are less reddened than SN 2002bo, one may be tempted to blame the high extinction. A lower reddening would mean that a lower luminosity has to be applied in order to reproduce the peaks in the optical and UV part of the spectrum, because these regions are mostly affected by extinction. However, observational results clearly indicate that $E(B - V) > 0.33$, which is still too large to solve the problem. A value $E(B - V) \lesssim 0.25$ is needed to improve the situation significantly. Furthermore, such a low value would have a large impact on the entire physical conditions and would lead to a better model only at this particular epoch, at the expense of consistency while calculating models at later times. Hence, this alternative explanation can also be rejected.

b) Day -12.0

The following spectrum was taken just one night after the first one at an epoch of $t_{exp} = 6.0 \text{ d}$. The best fit model is shown in Fig. 5.5a. The photosphere moved inwards in velocity space by 300 km s^{-1} with respect to the previous epoch and is now located at $v_{ph} = 15,500 \text{ km s}^{-1}$. The luminosity is $\log_{10} L = 42.31 \text{ (erg s}^{-1}\text{)}$, bringing T_{eff} to 8150 K . Although the evolution is quite minor it can be seen that the overall shape of the observed spectrum becomes somewhat steeper, i.e. the

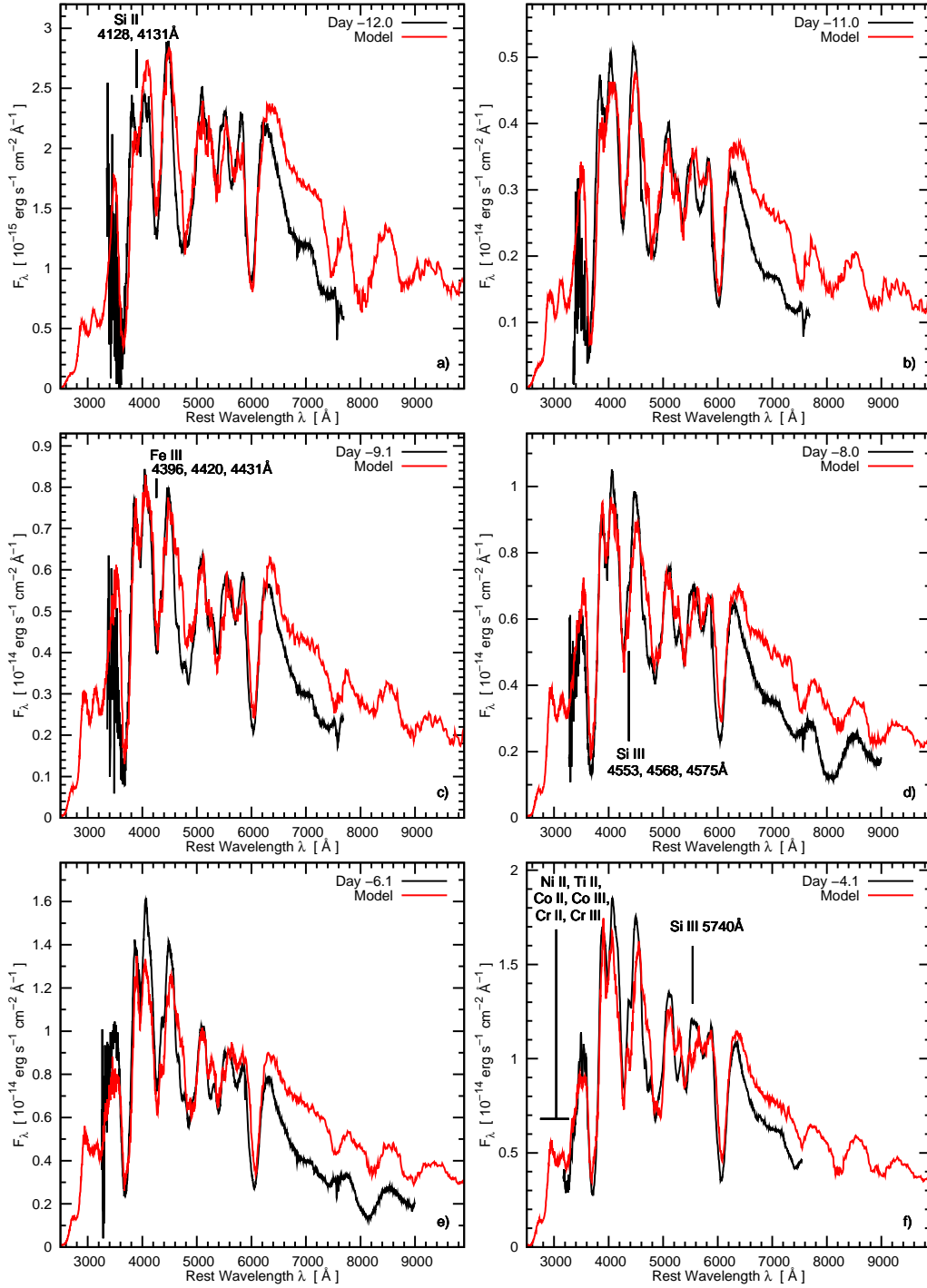


Figure 5.5: Observed spectra and corresponding models of SN 2002bo. Input values are: $E(B - V) = 0.38$, $\mu = 31.67$, a) $t_{exp} = 6.0$ d, b) $t_{exp} = 7.0$ d, c) $t_{exp} = 8.9$ d, d) $t_{exp} = 10.1$ d, e) $t_{exp} = 11.9$ d, f) $t_{exp} = 13.9$ d.

peaks in the U - and V -bands are higher with respect to those in the V - and I -bands. The temperature of the spectrum, as indicated by the Si II line ratio, has changed only marginally, whereas the model temperature has increased by ~ 500 K. This leads to a smaller Si II line ratio in the model. The somewhat less absorption in Si II 4130 Å with respect to the observation is due to the strong re-emission of the Ca II H&K line that interferes with the Si II line.

Almost every synthetic line lacks some blue-wing absorption. This is best seen in the Si II lines as well as in Ca II H&K, Mg II and Fe II. The most prominent effect in this context is shown by the Fe II–Si II feature at ~ 4600 Å, but it is also seen in Si II 6355 and 5970 Å, and Mg II 4481 Å. Although the Si abundance in the outer regions is enhanced (s. 5.3.4a) and has an unusually high level near the photosphere (30% by mass), this is still not sufficient to fit the blue wing of this line. The line velocity required to account for the blue absorption is $\gtrsim 20,000$ km s $^{-1}$. Because of the fast expansion of the ejecta density and therefore also the mass dropped by almost a factor of 2 in this high velocity region since the previous spectrum. Hence, the contribution of this region to the line formation is of minor importance and cannot account for the deep absorption seen in the observation.

There is still a discrepancy in flux at red wavelengths between model and observation. However, the difference is much smaller compared to the previous model, which supports the comments made in Section 5.3.4a.

c) Day –11.0

The next spectrum of SN 2002bo was observed one day later ($t_{exp} = 7.0$ d). The luminosity increases by almost a factor of 2 with respect to the previous epoch to $\log_{10}L = 42.54$ (erg s $^{-1}$). A high luminosity is necessary to get enough flux in the blue part of the spectrum, also because of the high reddening. Temperature rises to $T_{eff} = 8750$ K. The photosphere recedes inwards by 400 km s $^{-1}$ to $v_{ph} = 15,100$ km s $^{-1}$. A jump in velocity of ~ 500 km s $^{-1}$ d $^{-1}$ compensates for the expansion of the SN envelope and keeps the effective radius at a roughly constant value. The two effects combine to increase the temperature and the ionisation. T_{eff} increases from 8150 K to 8750 K between day –12.0 and day –11.0, as shown by the spectrum in Fig. 5.5b. Modelling this spectrum requires a large amount of IME, especially Si, in order to reproduce the deep absorption lines.

However, from the photosphere up to $\sim 20,000 \text{ km s}^{-1}$ more than 99.9% of Si is doubly ionised. Thus, increasing the Si abundance results in Si III lines appearing which are not seen in the observations, while Si II lines are saturated near the photosphere and do not become stronger. Outer regions do not contribute since the density is too low. This problem will become more serious at later epochs.

d) Day -9.1

Figure 5.5c shows the spectrum at day -9.1 corresponding to an epoch of $t_{exp} = 8.9 \text{ d}$. The photosphere is located at $13,900 \text{ km s}^{-1}$ and the emergent luminosity is $\log_{10}L = 42.77 \text{ (erg s}^{-1}\text{)}$. The temperature in the model is $T_{eff} = 9230 \text{ K}$. If we consider the Si II line ratio as our temperature indicator, this must be close to the true value since the two relevant Si II lines fit the observation very well. The very good match between model and observations in the Si II line at 4130 \AA confirms this statement.

The feature at $\sim 4200 \text{ \AA}$, which was purely made of Mg II in previous epochs, now contains a remarkable fraction of Fe III 4420 \AA . Not only in the 4200 \AA line is Fe III taking over, but Fe is now doubly ionised over almost the entire envelope. In contrast, the broad absorption feature near 4800 \AA appears too weak in the model. The increase of Si III and Fe III at the expense of the singly ionised species leads to insufficient line strengths of Fe II and Si II.

The shape of the synthetic Ca II H&K line suggests a lack of high velocity Ca. The depth of both absorption and emission of this feature is correctly reproduced. However, some absorption in the blue wing is missing. Also the strong Si II line at 6355 \AA obviously lacks some high velocity absorption. The abundances cannot be increased without exceeding reasonable values and they are constrained anyway by the previous epochs. New ideas have to be invoked to overcome this problem. An increased density in the outermost regions of the SN ejecta is a possible solution. This enhancement could be explained by circumstellar interaction. We will come back to this later in the discussion of the results in Section 5.3.9.

e) Day -8.0

At day -8.0 ($t_{exp} = 10.1 \text{ d}$, see Fig. 5.5d) the photosphere has reached a velocity of $12,900 \text{ km s}^{-1}$. The effective temperature stays almost constant compared

to the previous model ($T_{\text{eff}} = 9390 \text{ K}$), the luminosity is increased to $\log_{10}L = 42.84 \text{ (erg s}^{-1}\text{)}$. This spectrum is of special interest, because it is the first one in the sequence that covers the Ca II IR triplet at $\sim 8000 \text{ \AA}$. This makes the lack of blue absorption more evident. The line appears overall somewhat weaker in the model, but the most obvious difference can be recognized in the blue wing. Again, this problem cannot be overcome by increasing the Ca abundance near the photosphere suggesting an increased density at high velocities. A similar behaviour can be seen in the deep absorption at $\sim 7400 \text{ \AA}$. This is a combination of strong Mg II lines (7877 \AA & 7896 \AA) and weaker O I (7772 \AA) and Si II (7849 \AA) lines. The Mg part may be a little bit overestimated whilst the left wing of the line is missing. This is partially due to the low O abundance, but also to the weakness of the high velocity Si absorption. The same effect is seen, less dramatically, with time in the Si II lines at 6355 \AA , 5970 \AA and 5056 \AA .

The Si III line at $\sim 4567 \text{ \AA}$, which was already visible in the model at day -11 , starts to appear in the observations. This suggests a rise in temperature and a higher fraction of doubly ionised species.

f) Day -6.1

Day -6.1 ($t_{\text{exp}} = 11.9 \text{ d}$) is shown in Fig. 5.5e. A luminosity of $\log_{10}L = 42.97 \text{ (erg s}^{-1}\text{)}$ is reached and $v_{\text{ph}} = 11,450 \text{ km s}^{-1}$ resulting in $T_{\text{eff}} = 9860 \text{ K}$, 470 K higher than in the previous epoch. This affects the ionisation and leads to a higher fraction of doubly ionised species. Therefore the Si III feature at $\sim 4565 \text{ \AA}$ is stronger and the line Si II line at 5970 \AA is weaker. Several S II lines are present between 5000 \AA and 5400 \AA . The absorption near 5300 \AA is weaker in the model than in the observations. This is a known problem from previous analyses of SNe Ia. It may arise from a shortcoming in the atomic line list containing some insufficiently explored gf -values of the S II lines.

At about this epoch first signs of the inadequacy of the Schuster-Schwarzschild approximation become evident. The energy input is delivered by thermalised γ -rays originating from the radioactive decay chain $^{56}\text{Ni} \rightarrow ^{56}\text{Co} \rightarrow ^{56}\text{Fe}$. Since most of ^{56}Ni is located deep in the SN ejecta it is safe to state in the very early phase that all the energy is produced well below the model photosphere. However, as time goes on and the photosphere penetrates deeper into the envelope, the transition region from the optically thin to the optically thick regime becomes

more and more diffuse. Therefore, some of the energy comes from layers above the photospheric radius. Consequently, some model blue photons are emitted too deep compared to reality, and tend to doubly ionise elements resulting for example in rather strong Si III lines. The opposite happens for red photons, many of which are emitted too far out, at a low temperature, and with too much flux. In reality, they originate from much deeper layers than assumed, but escape easily because of the low opacity in the red. This leads to an overestimated flux in the red part of the model spectrum.

g) Day -4.1

The spectrum at day -4.1 (Fig. 5.5f) was taken 13.9 d after the explosion. This observation extends well to short wavelengths down to 3200 Å. The absorption at the blue edge of the spectrum is a combination of a large number of Ni II, Co II, Co III, Ti II, Cr II and Cr III lines which cannot be distinguished unambiguously. The model was computed with $\log_{10}L = 43.04$ (erg s^{-1}), $v_{ph} = 10,400$ km s^{-1} , and it reaches $T_{\text{eff}} = 10,040$ K.

The model matches the observation very well in this region. This shows the ability of the MC method to treat line blanketing. Deviations of the model from the observation in other regions of the spectrum are due to (1) rather strong lines of Si III (~ 4600 and 5740 Å). This suggests that the temperature may be a bit on the high side. (2) Missing opacity at high velocities ($v \gtrsim 18,000$ km s^{-1}) leads to insufficient absorption in the blue wings of several lines, most prominently Si II at 6355 Å and the Mg II dominated feature at ~ 7400 Å. (3) The problem with S II was already discussed in Section 5.3.4f.

h) Day -4.0 and day -3.9

The two spectra at day -4.0 and day -3.9 were observed with a time difference of only 45 minutes at two different telescopes. Since the later spectrum, taken with the Nordic Optical Telescope (NOT), has better resolution ($R_{\text{NOT}} = 14$ Å) than the Asiago one ($R_{\text{A1.82}} = 25$ Å) and extends to longer wavelengths only the NOT spectrum is shown in Fig. 5.6a. This model has an epoch of $t_{\text{exp}} = 14.1$ d, photospheric radius $v_{ph} = 10,200$ km s^{-1} , luminosity $\log_{10}L = 43.05$ (erg s^{-1}) and $T_{\text{eff}} = 10,080$ K.

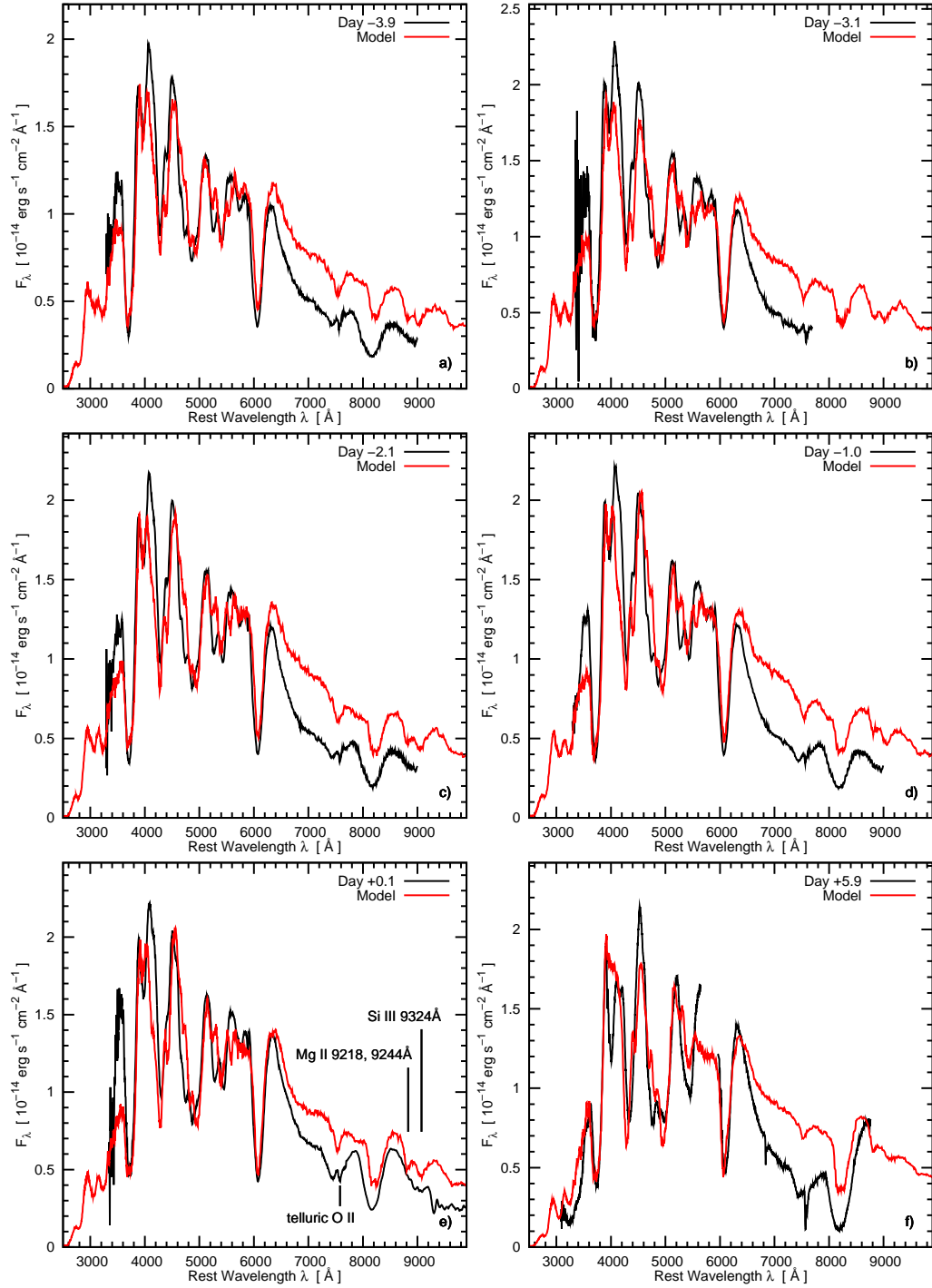


Figure 5.6.: Observed spectra and corresponding models of SN 2002bo. Input values are: $E(B - V) = 0.38$, $\mu = 31.67$, a) $t_{exp} = 14.1$ d, b) $t_{exp} = 15.0$ d, c) $t_{exp} = 15.9$ d, d) $t_{exp} = 17.0$ d, e) $t_{exp} = 18.1$ d, f) $t_{exp} = 24.0$ d.

Although this spectrum was observed shortly after the one on day -4.1 ($\Delta t = 4.8$ h) the day -3.9 spectrum is significantly bluer than the previous one. This may be due to a calibration effect since the two spectra were observed with different telescopes. The exact value of the colour evolution $\Delta(B - V)$ cannot be stated here because no photometry is available for the WHT spectrum and only a B -band measurement for the Asiago one. The models for both spectra have the same chemical composition and differ only marginally in luminosity ($\Delta \log_{10} L = 0.01$ (erg s^{-1})) and photospheric radius ($\Delta v_{ph} = 200$ km s^{-1}). Both models fail to reproduce the bright blue peaks. This may be due to the black body distribution placing too much flux in the red (Sect. 5.3.4f). The very rapid colour evolution may also indicate inconsistencies in the flux calibration. The 7896 \AA Mg II-dominated line exhibits too much low-velocity absorption, and so does the Ca II IR triplet. However, the high velocity blue wing of the absorption is missing. This made it difficult to homogenise the spectra because of individual filter functions, response functions of the CCD chips, etc. As mentioned in Section 5.3.1 many different telescopes contributed to the data set. The relative flux in the core of the Si II line varies with respect to the red part, confirming this. Another difficulty is the photospheric approximation that becomes more and more questionable.

i) Day -3.1

The model of day -3.1 (i.e. $t_{exp} = 15.0$ d) is shown in Fig. 5.6b. The luminosity $\log_{10} L = 43.08$ (erg s^{-1}) increases in slower steps compared to very early epochs since the light curve approaches its peak, and so does the radius ($v_{ph} = 9900$ km s^{-1}). Consequently, the temperature at the photosphere ($T_{\text{eff}} = 10,090$ K) rises only slightly since the previous epoch.

The SN has brightened by $\sim 10\%$ in the near-UV part of the spectrum over ~ 0.9 d while the red part remained almost constant. In order to fit the depth of the absorption line of the 6355 \AA Si II feature a high Si abundance is necessary. This however leads to an overshoot of the re-emission of this line, which may also be affected by the lower boundary. The high temperature makes the Si II line ratio too small and Si III line absorptions too strong.

j) Day -2.1

The spectrum at day -2.1, shown in Fig. 5.6c, was taken at an epoch of $t_{exp} = 15.9$ d. The luminosity ($\log_{10}L = 43.09$ (erg s^{-1})) increased only slightly with respect to the previous epoch ($\Delta \log_{10}L = 0.01$ (erg s^{-1})). The photospheric radius receded to 9200 km s^{-1} . Constant luminosity but decreasing radius means a higher temperature, $T_{\text{eff}} = 10,210$ K. This increase in temperature promotes deep Si III absorptions while the 4129 \AA Si II line becomes weaker. However, the observed spectrum becomes hotter, too. The Si II line ratio is small at this epoch and can be reproduced very well by the model. The relative depth of the Mg II line near 7500 \AA is now correctly reproduced, but Ca II IR triplet is too strong. Both lines lack blue absorption.

k) Day -1.0

The last spectrum before maximum light was taken at an epoch of $t_{exp} = 17.0$ d (Fig. 5.6d). The photospheric velocity v_{ph} recedes to 8600 km s^{-1} . The bolometric luminosity reaches its maximum at this epoch, $\log_{10}L = 43.10$ (erg s^{-1}) one day before the epoch of B maximum. The temperature also reaches its maximum, at a value of $10,250$ K. Both the day -2.1 and the day -1.0 spectra look qualitatively very similar, but the latter is slightly bluer if we consider the two peaks with shortest wavelengths. Unfortunately, only B -band photometry is available. A blend of Co III, Fe III and some weaker S III lines produce the deep absorption feature near 4200 \AA . The abundances of these elements may be slightly too high but cannot be reduced without negative influence on the overall shape of the model.

l) Day +0.1

The maximum light spectrum is shown in Fig. 5.6e. An epoch of 18.1 days is assumed for this spectrum, which is the only one that extends beyond 9000 \AA . The photospheric velocity has decreased to 8100 km s^{-1} , and the bolometric luminosity has already begun to decline at $\log_{10}L = 43.09$ (erg s^{-1}). The expansion and the declining luminosity reduce the temperature to $T_{\text{eff}} = 10,200$ K.

A weak absorption near 9100 \AA is possibly Si III 9324 \AA . The depth of the Ca II IR triplet relative to the continuum is reproduced very well, and only the blue

wing of the line is missing. The 7877, 7896 Å Mg II feature is blended by a telluric O₂ line. Si II lines are reproduced very accurately at this epoch. However, the high temperature leads to significant Si III lines at various places in the spectrum. The observed spectrum exhibits a much stronger peak ~ 3600 Å than the previous one. The somewhat erratic relative behaviour of the blue and the red part of the spectrum suggests that, although there certainly are weaknesses in the code owing to the black body approximation, there are also inconsistencies in the data calibration.

m) Day +5.9

The last model in the sequence of early time spectra that can be treated with the pre-maximum MC code is from day +5.9 corresponding to an epoch of 24.0 d. The photospheric radius is $v_{ph} = 7600 \text{ km s}^{-1}$. Although the epoch is several days after maximum, the luminosity has decreased only slightly ($\log_{10}L = 43.08 \text{ (erg s}^{-1}\text{)}$) while the temperature has dropped significantly ($T_{\text{eff}} = 9100 \text{ K}$) as a consequence of the expansion of the SN ejecta. This spectrum explores sufficiently deep layers that the derived abundance distribution overlaps with that from the models of the nebular phase (Sect. 5.3.5).

The observed spectrum consists of two distinct parts, as can be seen in Fig. 5.6f. This cuts into the Si II feature, which appears to be blended, making it difficult to tell whether the high emission near 5500 Å is real and whether the relative flux level of the two parts is correct. Despite the inadequacy of the photospheric assumption at this epoch the model delivers the correct overall flux distribution and almost all lines.

5.3.5. Nebular phase

The photospheric epoch coverage of SN 2002bo ends at day +6. This is only ~ 24 days after the explosion, and the photosphere at this epoch has receded to $\sim 7600 \text{ km s}^{-1}$. It is therefore not possible to extend the tomography experiment to lower velocities using the MC code. In any case, the code becomes less and less applicable at advanced post-maximum epochs, as the photospheric approximation becomes rapidly inadequate. There is however an alternative approach that makes it possible to investigate the properties of the inner part of the ejecta. That is modelling the spectra in the so-called nebular phase, when

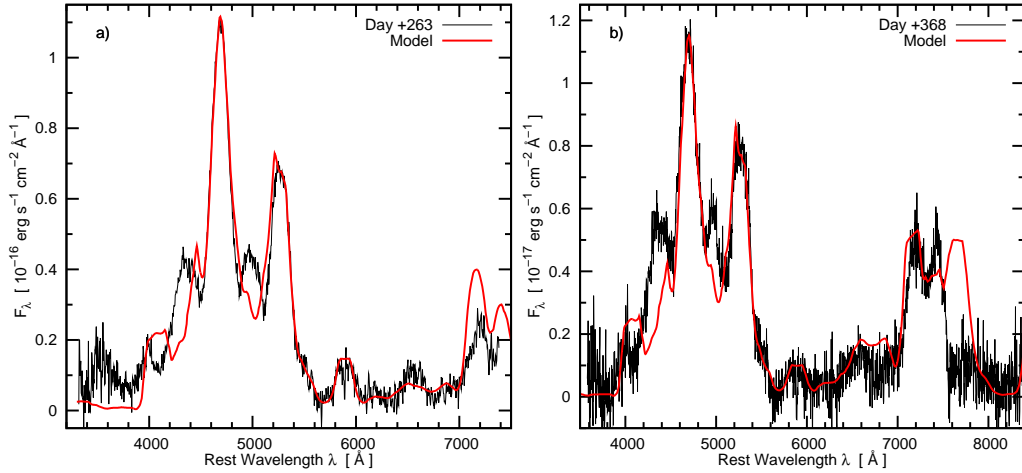


Figure 5.7.: Observed spectra and corresponding models of SN 2002bo in the nebular phase. Input values are: $E(B - V) = 0.38$, $\mu = 31.67$, a) $t_{exp} = 282$ d, b) $t_{exp} = 386$ d.

the ejecta are completely transparent. Models applicable to this epoch have been developed, and applied to various types of SNe (e.g. Mazzali et al. 2001b). These models follow the energy deposition and heating by the γ -rays and the positrons from the radioactive decay of ^{56}Ni and ^{56}Co , and the ensuing cooling via forbidden line emission. We have extended our previous, one-zone model also to treat abundance stratification in one dimension. The γ -ray deposition is treated in a Monte Carlo approach (Cappellaro et al. 1997), while the nebular emission is computed in NLTE. A code that treats stratified abundances can be used to obtain accurate modelling of the emission line profiles, and hence to derive the abundance distribution in the SN ejecta.

We have available also two nebular spectra taken on (Tab. 5.1) Dec. 11th, 2002 and March 26th, 2003 (e.g. 282 and 386 days after the estimated explosion epoch, respectively). The spectra were reduced following standard IRAF[†] (Image Reduction and Analysis Facility) routines. Extractions were weighted by the variance based on the data values and a Poisson/CCD model using the gain and read noise parameters. The background to either side of the SN signal was fitted with a low order polynomial and then subtracted. Fluxing was done by means of spectrophotometric standard stars.

[†]IRAF is distributed by the National Optical Astronomy Observatory, which is operated by AURA, Inc., under a cooperative agreement with the National Science Foundation.

We have adopted a W7 density profile, and fixed the abundances in the outer part of the ejecta according to the result of the photospheric epoch study above. In modelling the nebular spectra we then only had the freedom to choose the abundances below 7600 km s^{-1} .

We computed a model for the day +263 spectrum, which is shown in Fig. 5.7a. The total ^{56}Ni mass derived is $0.50 M_{\odot}$. This makes SN 2002bo an average SN Ia. The model reproduces the observed spectrum very well if the abundance of ^{56}Ni at velocities below 7600 km s^{-1} is increased above the values estimated from the photospheric epoch study at higher velocities. However, the ^{56}Ni abundance does not exceed 0.62 by mass in regions between 4000 and 7000 km s^{-1} . This is due to the significant mixing out of ^{58}Ni necessary to reproduce the early-time spectra. Further inwards, the ^{56}Ni abundance decreases, as expected. If it contains mostly ^{56}Ni the Fe line emission becomes too strong. There is however Fe emission at the lowest velocities, indicating the presence of significant amounts of stable Fe ($\sim 0.30 M_{\odot}$ at $v < 5000 \text{ km s}^{-1}$). Stable Fe must be excited by (mostly) γ -rays and (almost negligibly) positrons emitted locally in the regions where both ^{56}Ni and ^{56}Fe are present, and at higher velocity layers and propagating inwards for the central Fe. Spectroscopically, we are unable to distinguish between ^{54}Fe and ^{56}Fe . Both isotopes are the result of burning to NSE, but under slightly different densities. The abundance distribution is plotted later.

Our results imply that a total $\sim 0.80 M_{\odot}$ are burned to NSE. The ^{58}Ni abundance is low. Synthetic spectra for the later epoch (day +368) computed using the same abundance distribution nicely confirm these results (Fig. 5.7b).

We do not see any significant change of the line profiles or width over time, neither in the data nor in the models.

5.3.6. Abundance Tomography of SN 2002bo

Modelling of all spectra, both of the photospheric and the nebular phase, delivers the abundance distribution of the entire ejecta. The relative abundances by mass of each element that could be detected in the spectra as a function of radius in velocity space are shown in Fig. 5.8. The velocity of each step above 7600 km s^{-1} is determined as the photospheric radius of the particular spectrum. Therefore, the distance between two abundance shells is determined by the time gap between two consecutive spectra. An additional shell above $22,700 \text{ km s}^{-1}$ is inserted

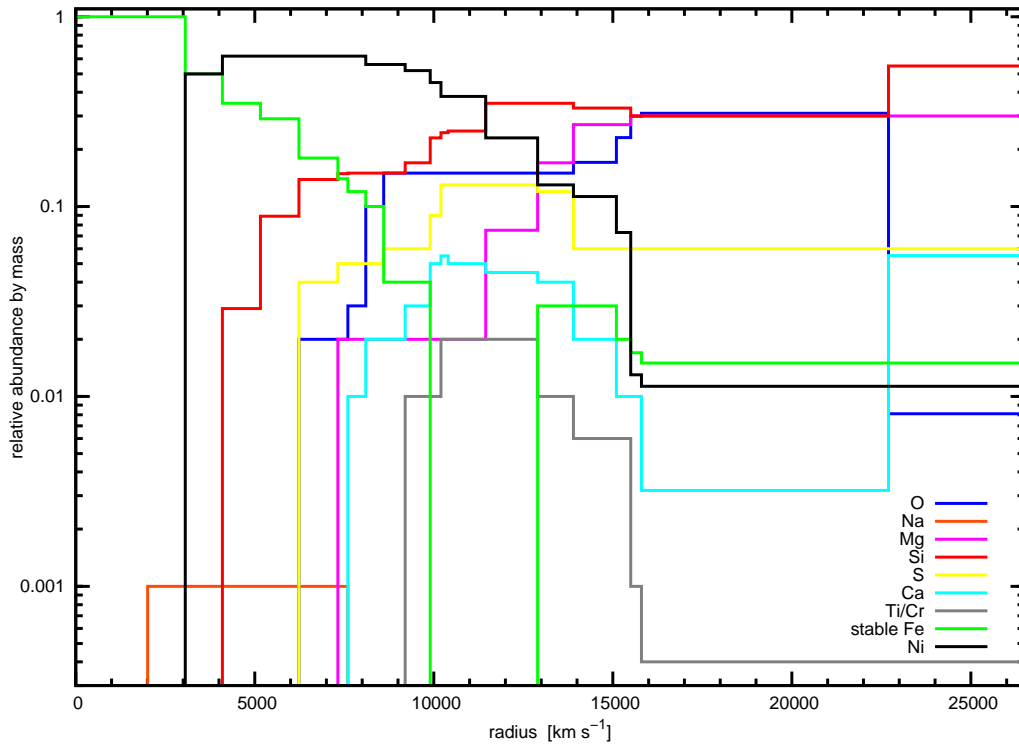


Figure 5.8.: The abundance distribution in the ejecta of SN 2002bo.

in order to account for high velocity material. Below 7600 km s^{-1} , where the abundances are derived from the nebular spectra, the radii of the shells are given by the density shells of the underlying W7 model. It is impossible to distinguish spectroscopically between different isotopes. Hence, the total sum of all possible isotopes is meant when discussing numbers in this paper unless an isotope is explicitly addressed. Since the abundance tomography covers the entire SN envelope the total mass of each element can be calculated. These values are listed in Table 5.4.

Since the WD is composed of C and O these two elements represent the unburned material in the SN ejecta. Their abundances indicate how far the burning process penetrated into the outer layers. Interestingly, no sign of C can be confirmed by the spectral analysis of SN 2002bo. The most prominent C lines in the optical and NIR wavelength bands are C II 6579 \AA and C II 7231 \AA . Both lines cannot be detected neither at early times and therefore high velocities nor at later epochs. In Benetti et al. (2004b) models of the optical spectra suggest

Table 5.4.: Total mass of elements in the ejecta of SN 2002bo spectroscopically confirmed by the Abundance Tomography and nucleosynthesis products of different SN Ia explosion models

Species	Ejected (Synthesized) Mass (M_{\odot})			
	SN 2002bo	W7 ^a	WDD1 ^b	b30_3d_768 ^c
C	$\lesssim 1.6\text{E-}03$	4.83E-02	5.42E-03	2.78E-01
O	1.10E-01	1.43E-01	8.82E-02	3.39E-01
Na	5.95E-04	6.32E-05	8.77E-05	8.65E-04
Mg	7.87E-02	8.58E-03	7.69E-03	8.22E-03
Si	2.21E-01	1.57E-01	2.74E-01	5.53E-02
S	6.66E-02	8.70E-02	1.63E-01	2.74E-02
Ca	2.14E-02	1.19E-02	3.10E-02	3.61E-03
Ti	3.20E-03	3.43E-04	1.13E-03	8.98E-05
Cr	3.20E-03	8.48E-03	2.05E-02	3.19E-03
Fe*	3.59E-01	1.63E-01	1.08E-01	1.13E-01
Ni**	5.19E-01	5.86E-01	5.64E-01	4.18E-01

*Stable isotopes except for ^{56}Fe from ^{56}Co decay

**Isotopes from the $^{56}\text{Ni} \rightarrow ^{56}\text{Co} \rightarrow ^{56}\text{Fe}$ decay chain

^a Nomoto et al. (1984)

^b Iwamoto et al. (1999)

^c Travaglio et al. (2004)

an upper limit of 3% on the C abundance at epoch of -12.9 d. An additional check was then performed by looking for C I lines in the IR. Since this new work confirms the previous result for the outer region and no evidence for C lines is found at later times, the upper limit of C is set to 3% above $15,800 \text{ km s}^{-1}$ which corresponds to a total mass of $\lesssim 1.6 \times 10^{-3} M_{\odot}$.

The other unburned element is O. Therefore rather high abundance in the outer layers and decreasing abundance towards lower velocities is expected to be found. Indeed, O dominates the zone between $15,800 \text{ km s}^{-1}$ and $22,700 \text{ km s}^{-1}$. Going deeper the abundance first decreases and then stays constant at a value of 15% until day -1.0 ($v_{ph} = 8600 \text{ km s}^{-1}$). Shortly after maximum light the O abundance drops and no O can be found below 6230 km s^{-1} . Altogether we find $0.11 M_{\odot}$ of O in SN 2002bo. Si dominates over O in the outermost regions due to the high Si abundance that can only be achieved on the expense of another element. We will come back to this issue later in this Section.

The group of partially burned species involves Na, Mg, Si, S and Ca. Except for Na, they all show rather high abundances at high velocities. Na itself is located above the Fe core and extends to $\sim 8500 \text{ km s}^{-1}$ which corresponds to the typical photospheric radius near maximum light. In this object the five shells between 3060 km s^{-1} and 7600 km s^{-1} contain 0.1% of Na, respectively. The total mass is $6.0 \times 10^{-4} M_{\odot}$.

Mg is one of the enhanced IME in SN 2002bo. A total mass of $0.079 M_{\odot}$ is derived from the abundance tomography. The bulk of it is concentrated on high velocities above $\sim 15,000 \text{ km s}^{-1}$ which corresponds to a relative abundance by mass between 23% and 30%. This is necessary in order to fit the deep absorption feature in the early phase at 4481 \AA as discussed in Section 5.3.4. Below $\sim 15,000 \text{ km s}^{-1}$ the Mg abundance decreases steadily and no Mg is detected below 7320 km s^{-1} .

The Si abundance exhibits a similar behaviour as Mg. However, the high velocity component is even more pronounced. The outermost shell above $22,700 \text{ km s}^{-1}$ contains 52% of Si in order to account for the blue wing absorption of the various Si II features. Since all abundances of each shell have to sum up to 100% individually, the increase of Si is done on the expense of another element. In the case of SN 2002bo not only C is burned completely to heavier elements but also a significant fraction of O. Therefore, higher Si abundance in the outer layers means reduced O abundance. Between $22,700 \text{ km s}^{-1}$ and $11,450 \text{ km s}^{-1}$ the abundance shells contain $\sim 30\%$ which is a typical value at these epochs although still on the high side. Deeper in the ejecta Si stays at $\sim 15\%$ down to 6230 km s^{-1} and then it drops rapidly until it disappears below 4100 km s^{-1} . Integrating over the entire range a total mass of $0.022 M_{\odot}$ is derived.

The S abundance goes with the Si but on a lower level and it does not exhibit the rise in the outermost shell. Following the S abundance distribution from outside in it starts at 6%, increases to $\sim 13\%$ at intermediate velocities ($12,900 - 10,200 \text{ km s}^{-1}$), decreases to $\sim 6\%$ before it disappears at 6230 km s^{-1} . The total mass is $0.067 M_{\odot}$.

Ca completes the set of IME that can be detected in SN 2002bo. This element is the best to study high velocity components. As already discussed in Section 5.3.4 the Ca II IR triplet misses significant absorption in its blue wing. We tried to account for this by using up to 20% of Ca at intermediate and especially at high velocities. However, even with 100% Ca in the outermost layers it is impossible

to fit the blue part of the line. Moreover, the synthetic spectra of the nebular phases do not work with such a high Ca abundance ($\approx 0.058 M_{\odot}$). Why is the over estimate of the Ca abundance not seen in the photospheric spectra? First of all, only a few spectra in the early phase extend to wavelengths above 7500 Å while the others do not show the Ca II IR triplet. The Ca II H&K line, which is visible in all spectra, is saturated and therefore rather insensitive to changes in the Ca abundance. Second, the nebular spectra exhibit a strong Ca emission feature due to Ca II 7291 Å and 7324 Å which constrain very well the Ca abundance up to $\sim 10,000 \text{ km s}^{-1}$. Therefore a second iteration of the modelling of the early time spectra using a significant lower value for the Ca abundance was investigated. The final result gives a high Ca abundance above $22,700 \text{ km s}^{-1}$ (5.5%), 0.3% in the next deeper shell and 1% – 5.5% in the range between 15,800 and 7500 km s^{-1} . No Ca is found below this velocity. In the final version $0.021 M_{\odot}$ of Ca is calculated. The problem with the high velocity absorptions cannot be solved by a simple enhancement of the abundances but scenarios like an increased density in the outer regions of the SN ejecta due to circumstellar interaction may explain reality much better.

For Ti and Cr, which go together with abundance, a total mass of $6.4 \times 10^{-3} M_{\odot}$ is derived. Even in the outer shells a small but observable fraction of these elements (0.04%) is seen. This value increases to 2% at around $10,500 \text{ km s}^{-1}$ and then drops to 1% before it disappears below 9200 km s^{-1} . Although no separated lines of the species can be detected in the spectra Ti and Cr are inevitable to block the photons in the UV and blue part and to shift the flux into regions with longer wavelengths (s. Chapt. 8).

Stable Fe is meant to be the sum of all non radioactive Fe species (^{54}Fe , ^{56}Fe , ^{57}Fe , ^{58}Fe) but not ^{56}Fe that is produced in the decay of ^{56}Co . The value for Ni includes all isotopes (radioactive and stable) from the decay chain $^{56}\text{Ni} \rightarrow ^{56}\text{Co} \rightarrow ^{56}\text{Fe}$. The Fe core of SN 2002bo extends basically to 3060 km s^{-1} with a small Na contribution of 0.1% above 2010 km s^{-1} . Further out Fe decreases steadily and there is no evidence for Fe in the velocity range from 9900 to $12,900 \text{ km s}^{-1}$. Above this void region there is 3% to 1.5% of Fe found that extends to highest velocities and was most likely mixed out during the explosive burning phase. Altogether a total mass of $0.36 M_{\odot}$ of stable Fe is measured. The Ni dominated shells sit on top of the Fe core with an abundance of $\lesssim 62\%$ out to 9900 km s^{-1} . Beyond this it decreases constantly to $\lesssim 1.3\%$ above $15,500 \text{ km s}^{-1}$ but also

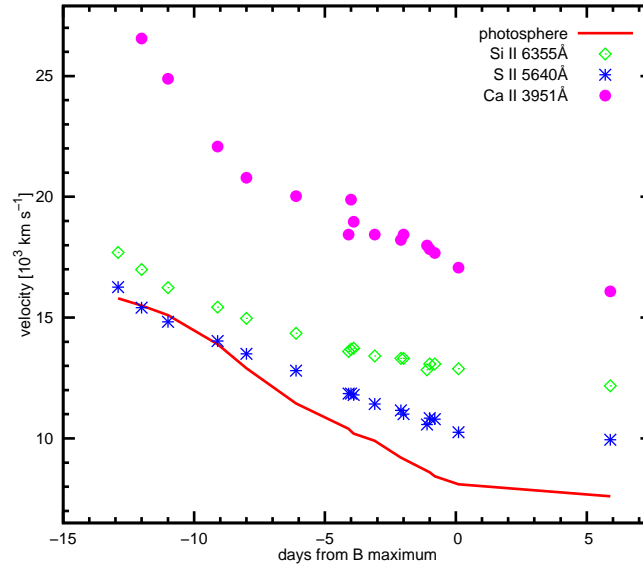


Figure 5.9.: Evolution of the expansion velocities deduced from the minima of the Si II 6355 Å, S II 5640 Å, Ca II H&K absorptions and the photospheric radius of the synthetic spectra.

extends to the outermost layers. Since Ni is the fuel that powers the light curve it is of great interest to achieve the total Ni mass produced. From the abundance tomography we derive a value of $0.52 M_{\odot}$. In Section 5.3.8 an alternative method to calculate the Ni mass is presented and the results of the two measurements are discussed.

5.3.7. Expansion velocities

The fact that the velocities of IME line in SN 2002bo are peculiarly high has been mentioned several times. Therefore, it is interesting to see how the velocities of the observed lines compare to the model calculations. Since the line-forming region is located close to the photosphere, the photospheric radius is a good estimate for the expansion velocities of the model line features. The evolution of the photospheric velocity is compared to the expansion velocities of Si II 6355 Å, S II 5640 Å, and Ca II H&K line as measured from their minima (Benetti et al. 2004b). The comparison of the velocities as a function of time is shown in Fig. 5.9.

A decline of the photospheric velocity in the early phases by $\approx 500 \text{ km s}^{-1} \text{ d}^{-1}$ was deduced from previous analyses (Mazzali et al. 1993) and is taken as a reference value. The photosphere of SN 2002bo recedes only by $700 \text{ km s}^{-1} \text{ d}^{-1}$ between day -12.9 and day -11.0 . The flat decline accounts for the high velocity absorption features, since the photospheric radius is set to fit the blue wings of the lines. After day -11.0 , the decline is steeper ($590 \text{ km s}^{-1} \text{ d}^{-1}$). The shape of the curve becomes significantly flatter after maximum light. The three lines shown in Fig. 5.9 exhibit a slightly different behaviour than the photosphere. Their velocities decrease more rapidly until day ~ 8 and at a slower rate afterwards. After maximum light the gradient is very similar to the photospheric one.

The S II line has the lowest expansion velocity. On day -12.0 and -11.0 it is actually lower than the photospheric velocity. Especially on day -11.0 it can be seen that the model absorption is blueshifted with respect to the observation (see Fig. 5.5a). After day -9.1 the line velocity lies well above the photosphere.

The Si II expansion velocity shows a very similar behaviour in the early phase. However, it declines at a slower rate than the S II line between day -6.1 and maximum light. It is always significantly faster than the photospheric velocity. The observed discrepancy is caused by the strength of the Si II line, which is formed well above the photosphere. The line is highly saturated near the photosphere and the sensitive region for the line formation lies at higher velocities than the photosphere.

Line velocities of $\sim 25,000 \text{ km s}^{-1}$ and beyond which are measured for the Ca II line tell from an even more extreme case. Already at very early epochs the line is almost completely saturated and only the high velocity components contribute to the varying line formation. This means, that Ca II is clearly detached from the photosphere and alternative explanations have to be considered and taken into account.

5.3.8. Bolometric light curve

In order to check the validity of our results in an independent manner, we have taken the abundance distribution determined with the tomography experiment, and computed a synthetic bolometric light curve for SN 2002bo, assuming that the density is as given by W7 and using the MC light curve model developed by P.A. Mazzali and presented in Cappellaro et al. (1997) and Mazzali et al. (2001a).

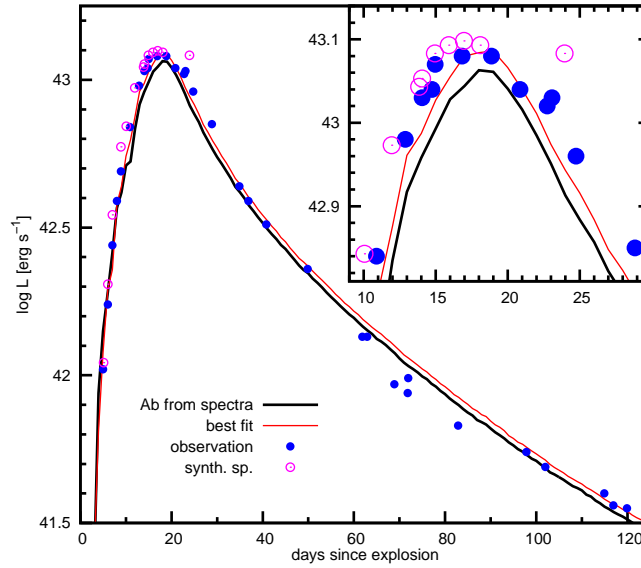


Figure 5.10.: The uvoir light curve of SN 2002bo. The black dots represent the observed photometric points, the circles are the bolometric luminosity deduced from the synthetic spectra. Two models of the MC light curve code are shown using only abundances from the spectral analysis (—) and with increased ^{56}Ni mass (—).

We have compared the results with the bolometric light curve of SN 2002bo presented in Benetti et al. (2004b). The results are shown in Fig. 5.10.

Using the abundance distribution determined with the tomography experiment, we obtain a very good description of the light curve, and in particular of the rising branch. In fact, the early light curve rise depends mostly on the mixing out of ^{56}Ni . The success of the light curve modelling shows that abundance tomography is a very effective way to explore the properties of the ejecta, especially in the outer layers.

The model is less successful near the peak of the light curve. A slight modification of the abundances, with ^{56}Ni increasing to about $0.56 M_{\odot}$ and stable Fe decreasing accordingly, yields a better fit of this period. This is a small change, which does not affect the essence of our results.

5.3.9. Conclusions

The method of Abundance Tomography was presented in this Chapter and applied to the normal SN Ia 2002bo. Modelling a time series of spectra allows us to

derive accurately the distribution of abundances in the SN ejecta, from the lowest to the highest velocities, which is an important element in our understanding of the nature of the explosion and the progenitor.

Synthetic spectra for SN 2002bo were computed for 13 spectra during the photospheric phase and 2 in the nebular phase. In the case of SNe Ia, the chemical composition determines essentially all of the observables (spectra and light curve). Thus, knowledge of the abundances and their distributions of many SNe Ia may be able to explain some of the diversities among these objects.

SN 2002bo is a typical “Branch normal” SN Ia in many respects (Benetti et al. 2004b). In spite of this normality, the abundance distribution of SN 2002bo exhibits somewhat unusual behaviours. The complete absence of C in the entire ejecta combined with the presence of high-velocity IME may suggest that the Si burning front must have been penetrating far into outer regions. Simple mixing out of IME to high velocities implies the existence of unburned C and O at lower velocities. However, neither is an increased O abundance found deeper in the ejecta, nor is C detected above an upper limit of $1.6 \times 10^{-3} M_{\odot}$.

One possibility to produce a situation like that observed in SN 2002bo are multi-dimensional effects. Bubbles of burned material may rise to outer regions while fingers of unburned material sink to deeper layers. Unlike the case of global mixing, the direction from which the observer looks at the SN may be important. In the case of SN 2002bo one of these partially burned bubbles reaching out to high velocities may be in the line of sight, delivering the spectra and abundance distribution we observe. If we had looked from another position we may possibly have seen the missing C and less or no high-velocity components in the lines of IME (e.g. Kasen et al. 2004).

In this context it would be interesting to verify whether multi-dimensional effects can account for the observed diversity in SNe Ia beyond the brightness-decline rate relation. Abundance tomography can contribute significantly to this effort if it is applied to more well-observed objects.

Another possibility is a scenario where the configuration prior to the explosion affects the spectra. If we saw the interaction of the SN ejecta with circumstellar

material, an increased density may give rise to the high velocity components as the result of swept up material far out. More investigations and calculations on possible progenitor systems and their configuration after the explosion, as well as the analysis of more objects, have to be carried out to verify this scenario. Several SNe Ia are analysed on high velocity line features in Chapter 7 of this work.

6. The incident radiation field

The spectral analysis of SN 2002bo showed that there is a discrepancy between the models and the observations in the red part of the spectrum. In the case of SN 2002bo we suspect that difficulties in the flux calibration might be responsible for that phenomenon. In this Chapter an alternative solution for this problem is presented. The real flux distribution in the SN envelope may be inadequately described by a black body radiation field that is used in the MC technique so far. In Section 6.1, the flux distribution that results from the ^{56}Ni decay in the SN ejecta is described and the consequential requirements for synthetic spectra calculations are given. The modifications of the MC procedure for a better treatment of the incident radiation field are discussed in Section 6.2, before the new method is tested by calculating synthetic spectra of SN 2002er in Section 6.3.

6.1. The flux distribution in the supernova envelope

The power source of SNe Ia is the radioactive decay of ^{56}Ni that is formed in the core of the SN progenitor during its collapse, when the stellar core is burned to NSE. The emitted γ -rays are degraded into UV, optical and IR photons by their interaction with the ejecta giving rise to the observed spectra. Pinto & Eastman (2000) showed that the different half life of ^{56}Ni and ^{56}Co together with the fact that the photons emitted deep in the ejecta have a larger diffusion time than the characteristic time of the main physical conditions lead to a strong time dependence of the spectrum formation and to the typical shape of the light curves (s. Sect. 2.1.1). Moreover, since the radioactive material is not distributed homogeneously throughout the SN envelope, the energy input is also non-isotropic. It is therefore necessary to calculate the entire process of energy deposition and ensuing thermalisation of the photons to longer wavelengths in order to achieve a consistent treatment of the problem.

The early and later phases of the light curve and spectrum formation must be differentiated. During the first few weeks after the explosion, when the expansion is only little advanced, the SN envelope is dense enough that the optical depth reaches unity within the envelope itself. The many thousands of lines – especially those from the Fe group elements – essentially block all the flux and the photons are re-absorbed immediately after they have been emitted by a line. This also affects the thermalisation of the γ -rays from the radioactive decay. Their mean free path is even shorter than for optical photons and so they are degraded very rapidly. Therefore, the energy deposition occurs locally where the γ -rays are produced. If we finally consider that most of the radioactive material is located near the core of the ejecta, the assumption of a well defined effective photosphere that emits a pseudo continuum radiation can be justified in the early phase (Schuster-Schwarzschild approximation).

The incident radiation field at the photosphere can to first order be approximated with a black body distribution. However, from Section 4.1.3 it can be seen that we must differentiate between the UV part of the spectrum and longer wavelengths. Even at very early epochs there is less radiation emitted in the red part of the spectrum ($\lambda \gtrsim \text{Si II } 6350 \text{ \AA}$) than one would expect from a black body distribution. This is due to the lack of line opacity in this wavelength region. Most of the flux arises from downgraded photons of blue and UV lines rather than from lines which are absorbing in the red. Therefore, a modified Planck function, emitting more radiation at short wavelengths, leads to higher accuracy of the synthetic spectra calculation and is closer to the physics of the SN event. The new approach is presented in the following Section.

6.2. The incident radiation field in the Monte Carlo procedure

In the present version of the MC code the photospheric luminosity is assumed to be a black body radiation field. At the beginning of each MC iteration a subroutine is called that samples the Planck function $B_\nu(T_{\text{eff}})$ with a number of frequency bins according to the effective temperature at the photosphere. Each bin is constrained to contain the same integer number of equal energy packets. Hence, each bin has the same energy and the width in frequency increases for

lower frequencies (s. Sect. 4.2.4). This technique is called *stratified sampling* and damps Poisson fluctuations. For SNe it gives a smooth continuum.

The basic method remains unchanged in the new approach but a redistribution of the incident flux is applied to account better for the real physical conditions described in the previous Section. This is done by shifting flux from the red part of the spectrum to the blue, keeping the total luminosity fixed. Two new parameters are introduced: (1) λ_c marks the wavelength redwards of which the flux is redistributed. (2) f_F gives the flux fraction relative to the black body function that is cut in the region $\lambda \geq \lambda_c$. Both parameters are adopted to the actual spectrum.

Next, the excessive energy in terms of the number of energy packets of each red wavelength bin is calculated. If each bin originally contains n_0 packets, k is the total number of wavelength bins, and λ_c lies in the i th bin, then the number of packets that have to be removed is:

$$N_r = \lceil f_F \cdot n_0 (k - i) \rceil, \quad (6.1)$$

i.e. the smallest integer not less than the real part of the expression on the right. Hence, we subtract $n_r = N_r / (k - i)$ packets from each red bin.

These N_r packets are then shifted to the blue. Each bin in the wavelength region $\lambda < \lambda_c$ gains $n_a = \lceil N_r / i \rceil$ packets. The remaining packets are finally distributed randomly among the blue bins. Figure 6.1 shows schematically the redistribution procedure for a Planck function at a typical temperature of 10,000 K.

The redistribution procedure is only applied in the last iteration of the radiation field, when the temperature structure and the radiation field are already converged. If it was done in every iteration, the convergence would be hampered and the spectrum would become noisy, because the excessive packets are distributed randomly among the blue wavelength bins. Moreover, the convergence could fail completely if f_F is sufficiently large. Suppose we use $f_F = 0.5$, as in Fig. 6.1 and the procedure is carried out in every calculation cycle. That means that in every step half of the red flux is shifted to the blue. This leads to an increase of the radiation temperature because of the strong line blanketing at short wavelengths. Therefore, it is adequate to apply the redistribution only in the very last iteration when the physical conditions in the MC experiment are set up.

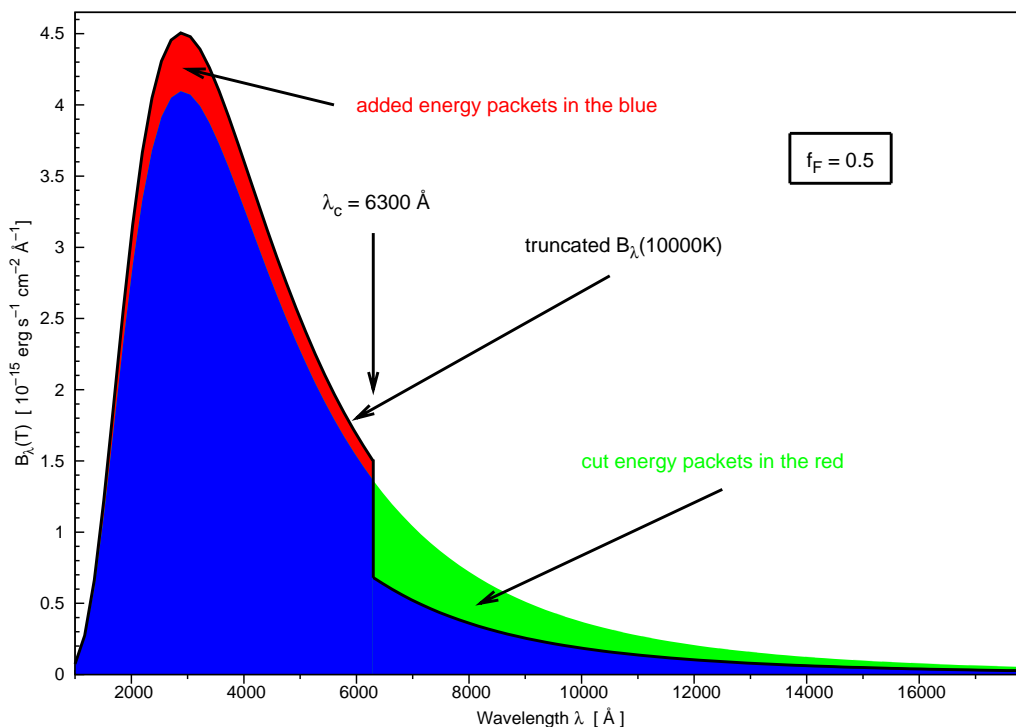


Figure 6.1.: Modified photospheric radiation field with $f_F = 0.5$ and $\lambda_c = 6300 \text{ \AA}$.

Owing to the branching routine, the blue lines emit sufficiently many photons in the red during one MC calculation, as it can be seen in Section 6.3, where the new procedure is applied to and tested with synthetic spectra of SN 2002er. The main advantage of this new approach is that the total luminosity is conserved and so is the overall energy of the modified black body radiation emitted at the photosphere. This is necessary to calculate the temperature stratification in the SN envelope.

6.3. Synthetic spectra of SN 2002er

Our test object for the modified photospheric radiation field is the normal SN Ia 2002er. The SN was discovered on 2002 August 23.2 UT in the spiral galaxy UGC 10743 by Wood-Vasey et al. (2002) and was spectroscopically confirmed to be a SN Ia three days later by Smartt et al. (2002); comparison with SN 1994D suggested that it was discovered at an early phase (about -10 d before maximum

Table 6.1.: Parameters of SN 2002er and its host galaxy (Pignata et al. 2004).

Host galaxy	UGC 10743
Galaxy type	Sa [†]
RA (2000)	17 ^h 11 ^m 29 ^s .88
Dec (2000)	+07°59′44″.8
Recession velocity [km s ⁻¹]	2652 ± 33 [‡]
Distance modulus (H ₀ = 71)	32.9 ± 0.2
E(B - V)	0.36 ± 0.05
Offset from nucleus	12." .3W 4" .7N
Date of B maximum (MJD)	52524.2 ± 0.5
Magnitude at max	U = 14.72 ± 0.04, B = 14.89 ± 0.03, V = 14.59 ± 0.03, R = 14.43 ± 0.03, I = 14.49 ± 0.05
$\Delta m_{15}(B)$	1.33 ± 0.04

[†] NED

[‡]LEDA, corrected for LG infall (208 km s⁻¹)

light) and that it was significantly redder. Considering the early epoch of the discovery and the proximity of the host galaxy, target of opportunity observations were immediately triggered at all available telescopes of the ESC. Mainly thanks to the contribution of the Calar Alto Observatory, almost daily coverage over the first month could be secured for both photometry and spectroscopy. The photometric results from 7 d before to over 619 d past maximum light, including the analysis of the bolometric light curve are published in Pignata et al. (2004). Spectroscopic observations will be presented in a separate paper (Kotak et al., in prep.). Table 6.1 summarises the main parameters of SN 2002er.

We calculated two models for SN 2002er, one for the earliest epoch at -11.3 d and one for an epoch near maximum light (day -2.4). Given the fact that there are significant difficulties with the flux calibration, we have to concentrate on deducing the correct parameters instead of studying peculiarities and special spectral features of the object. The comparison between spectra and photometry leaves significant uncertainties in the absolute flux of the spectra as well as in the relative flux of the different wavebands. Since the spectra are calibrated with respect to the V band, we primarily aimed at matching the flux in this band. Nevertheless, our main goal is to test the new method for which we are not strongly dependent on a precise flux calibration.

6.3.1. Day -2.4

In the first iteration of the day -2.4 spectrum we adapted a typical value for the photospheric velocity at this epoch of 9500 km s^{-1} . The distance ($\mu = 32.9$) and the reddening ($E(B - V) = 0.36$) were taken from Pignata et al. (2004). However, this set of parameters turned out to be not to yield a model that is comparable to the observational spectrum. The main problem is the temperature. In order to achieve the desired V flux the intrinsic luminosity has to be of the order of $\log_{10}L \approx 43.1 \text{ (erg s}^{-1}\text{)}$. This luminosity leads to a very high temperature at the photosphere ($T_{BB} \approx 13,000 \text{ K}$) and therefore to almost complete doubly ionisation of the elements. Especially the strong Si III lines that appear at this temperature are barely seen in the spectrum. Instead the spectrum exhibits strong Si II lines. Moreover, the large line ratio of Si II 5970 Å to Si II 6350 Å indicates a rather low temperature of the spectrum. Nugent et al. (1995b) derived a temperature of $\sim 9000 \text{ K}$ for a similar line ratio as in SN 2002er.

The temperature problem is the most obvious reason to doubt the initial choice of the various parameters, but there are other indications as well. According to the Phillips relation (Phillips 1993) an absolute brightness of $M_B^{max} = -19.5$ is very unlikely for SN 2002er with $\Delta m_{15} = 1.33$. The SN would then be brighter than SN 2002bo ($M_B^{max} = -19.41$), which has $\Delta m_{15} = 1.13$ (Benetti et al. 2004b, and Section 5.3.1). Furthermore, there is a problem with the $(B - V)$ colour derived from the observations. From the photometry measurement one gets $(B - V) = 0.17$ at day -2.4. Although the width of the Na I D line suggest an even higher value for $E(B - V)$ than 0.36, using this reddening leads to a very blue intrinsic colour.

We therefore tried to estimate the luminosity of the spectrum to be consistent with the Phillips relation. This value is $\approx 0.5 \text{ mag}$ dimmer than initially assumed. Indeed, using $\log_{10}L = 42.9 \text{ (erg s}^{-1}\text{)}$ leads to a very good model, reproducing all line features with the correct absorption depth. However, the luminosity of the model is $\approx 25\%$ lower than the observed. In order to overcome this discrepancy the two parameters reddening and distance can be modified. We explored the parameter space in distance between $\mu = 32.9$ and $\mu = 32.4$. Adopting a shorter distance clearly improves the match between the model and the observation significantly. However, the difference in $B - V$ remains and even for a distance of $\mu = 32.4$ it is not sufficient to account for it. But reducing the reddening could

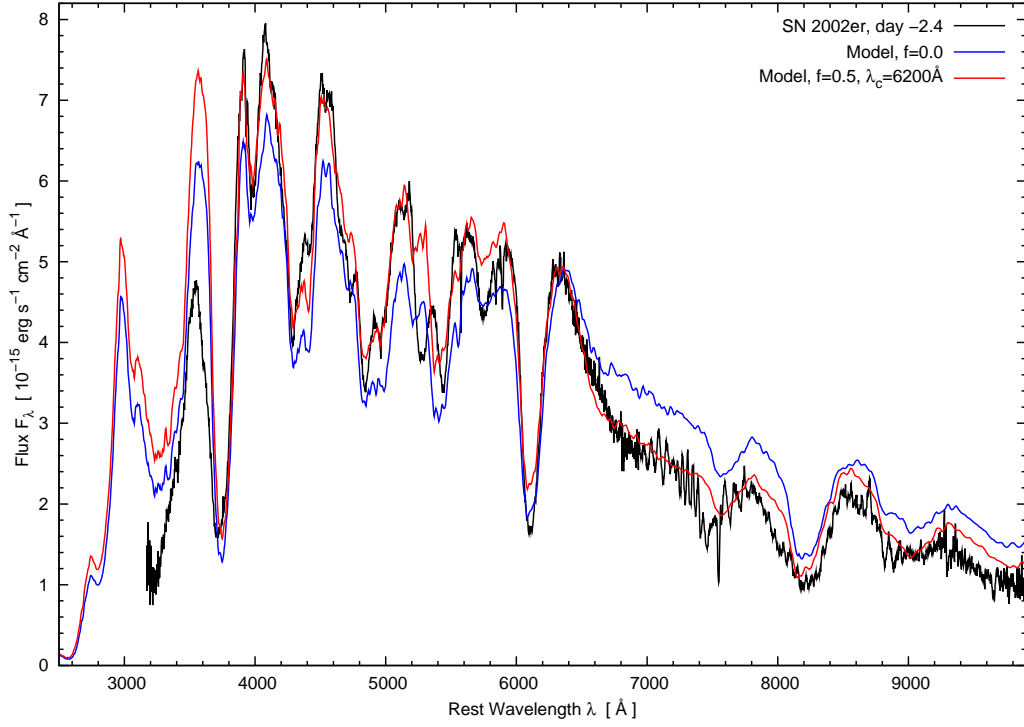


Figure 6.2.: Observed spectrum and corresponding models of SN 2002er at day -2.4 using $E(B - V) = 0.36$, $\mu = 32.60$, $t_{exp} = 17.6$ d. The red model is calculated with the modified incident radiation field $f = 0.5$, $\lambda_c = 6200 \text{ \AA}$.

simultaneously improve both the problem of the total flux and that of the colour.

Alternatively, we can apply our new approach. Since the overall energy emitted at the photosphere is conserved but the offset in the red can now contribute to the flux in the blue, the incident luminosity might be reduced possibly leading to a lower temperature at the photosphere but a steeper shape of the model spectrum. Indeed, as it can be seen in Fig 6.2, the results from synthetic spectra calculations confirm nicely our expectations. Two models are shown both with the same parameters for the epoch ($t_{exp} = 17.6$ d), the reddening ($E(B - V) = 0.36$), and the distance ($\mu = 32.60$) but the red one is calculated with the flux redistribution. In this case the black body function is truncated by a factor of $f_F = 0.5$ redwards of $\lambda_c = 6200 \text{ \AA}$. The distance in both cases is 0.3 shorter than it is observationally predicted, because the parameter study showed that this is the highest acceptable value for a reddening of $E(B - V) = 0.36$ and it is compatible with the error on the distance measurement (Pignata, priv. comm.). The following

discussion refers to the synthetic spectrum obtained with the new approach.

A luminosity of $\log_{10}L = 43.0$ (erg s^{-1}), emitted at a photospheric radius of 9300 km s^{-1} , leads to a photospheric temperature of $T_{BB} = 11,460 \text{ K}$. The epoch of 17.6 d is chosen according to a rise time of $t_{max} = 20.0 \text{ d}$, which is about half a day larger than the typical rise time of SNe Ia (Riess et al. 1999a). We identify strong Si II lines at 6360 \AA , 5970 \AA , now showing almost the correct line ratio, and at 4130 \AA . Additionally, the deep absorption near 4800 \AA contains a significant amount of Si II. The rest of this feature is caused by Fe II. Weak Si III lines can be seen at 4570 \AA and 5740 \AA , the latter is a bit too strong in the model. S II produces the absorptions near 5400 \AA . The feature $\sim 4400 \text{ \AA}$ is due to Mg II 4481 \AA , as well as the one near 7500 \AA . Finally we recognise the strong Ca II H&K lines and the Ca II IR triplet. Although it is not as pronounced as in the case of SN 2002bo (Stehle et al. 2004, and Chapt. 5), a high velocity component in the Ca II lines can be seen that cannot be reproduced by the model.

6.3.2. Day –11.3

In order to confirm our results near maximum light we modelled the spectrum at 11.3 days before maximum. Unfortunately there is no photometry available for this spectrum and it was necessary to infer the flux level in a different way. Using $E(B - V) = 0.36$, SN 2002er and SN 2002bo have very similar intrinsic colour $(B - V)_0$ in the pre-maximum phase. Assuming that this means a similar evolution in brightness before maximum, the V and B magnitudes of SN 2002er can be derived by comparing them to the values of SN 2002bo. SN 2002bo has $\Delta V = 1.5$ and $\Delta B = 1.64$ between day –11 and day –2. The same difference applied to SN 2002er gives $V_{-11} = 16.25$ and $B_{-11} = 16.56$. The observed spectrum ($V_{obs} = 15.82$) is then normalised to V_{-11} and it is kept in mind that the B band is under estimated by 0.1 mag. After that the model is calculated using the same values for distance and reddening as in the maximum one. The result is shown in Fig. 6.3.

The photospheric radius is located at $14,800 \text{ km s}^{-1}$, the luminosity reaches $\log_{10}L = 42.3$ (erg s^{-1}), and the temperature is $T_{BB} = 9620 \text{ K}$. This temperature regime nicely reproduces the strong Si II line absorptions, although the Si II 6350 \AA is slightly too strong. The somewhat higher flux in the blue part of the model is on purpose to account for the under estimation of this waveband in

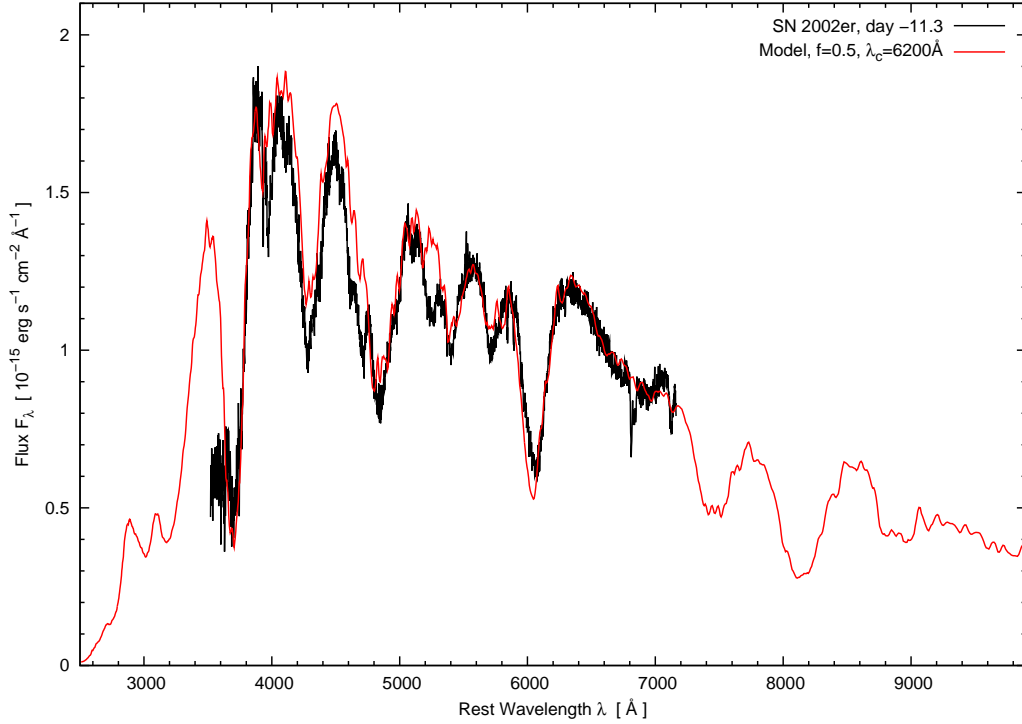


Figure 6.3.: Observed spectrum and corresponding model of SN 2002er at day -11.3 using $E(B - V) = 0.36$, $\mu = 32.60$, $t_{exp} = 8.7$ d, $f = 0.5$, $\lambda_c = 6200$ Å.

the normalisation. All the lines that can be seen have already been discussed in the previous section. Unfortunately, there is no coverage of the near IR region, which could be useful to study the effect of high velocity material.

6.4. Conclusion

In this Chapter we presented an improved treatment of the photospheric luminosity and tested it with synthetic spectra of SN 2002er. The method of a truncated black body, where the red flux is redistributed to shorter wavelengths, represents the true physical conditions in the SN ejecta much better than simply using an unmodified Planck function.

The modification is realised in the MC code by introducing two parameters. These parameters are adjusted according to the spectrum actually in question. This seems to be rather ad-hoc and is certainly somewhat unpleasant, since our long term ambition is to reduce the number of free parameters so that we reach

a higher level of self-consistency in calculating synthetic spectra. However, the models of SN 2002er significantly improved by applying the new method and the results confirm our approach. It is therefore a very good compromise until the complete treatment of the energy deposition from the ^{56}Ni and ^{56}Co decay is developed and implemented in the code. Two main advantages became clear from the synthetic spectra calculations:

1. Most of the previous models suffer from a temperature that is too high to reproduce the observed lines and their profiles. Since one typically tries to fit the flux level in the UV and optical regions, where the main features of the spectra are, the photospheric luminosity is pushed to high values. Thus, the emitted flux at these wavelengths represents the real flux rather well but in the red part of the spectra it is generally overestimated, and so is the total photospheric luminosity. Since the temperature scales in first order with the fourth power of the luminosity, the overestimate of the total flux leads to significantly higher temperature. This in turn affects the ionisation structure and therefore the lines and the emergent spectrum. By shifting the excessive flux from the red to the blue we not only decrease the emitted radiation in this region but at the same time increase the luminosity in the blue part. A smaller total luminosity is sufficient to reproduce the overall flux level and the temperature in the SN ejecta is decreased, too.
2. The line absorption depth of the models in the red part of the spectra fits the observations significantly better. Most of the flux in this region is originally not emitted at the photosphere by lines deeper in the ejecta but is rather due to consecutive downgrading of the photons' frequency caused by their increasing Doppler shift and the line blocking in the blue. The MC procedure naturally simulates this behaviour (Sect. 8.2).

From the spectral analysis point of view, it can be said that the 'normal' SN 2002er also shows peculiarities which make it an exciting object to analyse in more detail. Namely these interesting topics are (1) the high velocity Ca lines in the early time spectra and (2) the unusually high absolute magnitudes derived from the photometric analysis (Pignata et al. 2004) compared to the value of $\Delta m_{15}(B)$ and the cold line properties in the spectrum. However, a complete spectral analysis using the combination of the flux redistribution method and Abundance Tomography has to be postponed until the data are reduced properly.

7. Evidence for circumstellar interaction in Type Ia Supernovae

Several recent analyses of SNe Ia spectra detect detached, high-velocity components in near-maximum spectra, which can possibly be explained by interaction of the outermost region of the SN ejecta with circumstellar material. In this Chapter, we present synthetic spectra showing high-velocity absorptions in the Ca II and/or Si II lines in the otherwise normal SNe Ia SN 2002dj, SN 2003du, and SN 1999ee. We discuss alternative explanations, including abundance enhancements in the outer ejecta, a density enhancement of the SN envelope, and H dominated outer parts of the envelope as a result of circumstellar interaction.

7.1. High velocity line features

The analyses of SN 2002bo and SN 2002er, presented in Section 5.2 and 6.3, confirmed high-velocity line absorptions in their pre-maximum spectra, although they are not as pronounced as in the three objects we discuss in this Chapter. High-velocity components were observed in several SNe Ia spectra before. The first suggestion of high-velocity components was made by Hatano et al. (1999), who noticed features that they interpreted as high-velocity Ca II and Fe II in the spectra of SN 1994D. They showed by means of spectral modelling that Ca II and Fe II are present at $v > 25,000 \text{ km s}^{-1}$, and reaching $v = 40,000 \text{ km s}^{-1}$, detached from the photospheric component ($v < 16,000 \text{ km s}^{-1}$). Further evidence came from SN 2000cx (Li et al. 2001), which shows two strong and well separated components of the Ca II IR triplet at high velocities. Thomas et al. (2004) analysed the spectra of this rather peculiar SN Ia, using a simple 3-D spectrum synthesis model. They confirmed that detached Ca II is present at high velocities, this time $v > 16000 \text{ km s}^{-1}$. They also noticed a corresponding broadening of the Ca II H&K doublet, which however did not show detached features. Recently,

Branch et al. (2004) confirmed these findings and additionally reported that high-velocity Ti II features are also present. Detached features were also observed in SN 2001el (Wang et al. 2003) at $v \sim 22 - 26,000 \text{ km s}^{-1}$ and in SN 2004dt (F. Patat, priv. comm.).

7.1.1. SN 2003du

Supernova 2003du was discovered by LOTOSS on 2003 April 22.4 UT at magnitude of ~ 15.9 (Schwartz & Holvorcem 2003). The host galaxy is UGC 9391, a nearby SBd galaxy with a recession velocity of 1914 km s^{-1} . Based on a spectrum taken at the Isaac Newton Telescope on 2003 April 24.06 UT, Kotak et al. (2003) classified SN 2003du as a normal SN Ia at about two weeks before maximum light. Following this observation an intensive optical and infrared observational campaign was initiated by the ESC. After one year we have more than 40 spectra available covering the period from -13.4 to $+271$ relative to B maximum which makes SN 2003du to one of the best observed SNe Ia ever. Not only the ESC but also two other groups took observations of SN 2003du. Gerardy et al. (2004) used the Hobby-Eberly Telescope to obtain several optical spectra around maximum light and Anupama et al. (2005) published recently their results from optical observations of SN 2003du at the Indian Astronomical Observatory.

A high-velocity component in the Ca II IR triplet near 8000 \AA is detected a large expansion velocity ($\approx 18,000 \text{ km s}^{-1}$), which is nearly constant between -11 and $+3$ days and disappears shortly thereafter. Other than this feature, the spectral evolution and light curve of SN 2003du resemble those of normal SNe Ia. We computed synthetic spectra for day -11.5 which is the earliest epoch that covers both the optical and the near-infrared with the Ca II IR triplet. The earliest observed spectrum was taken on day -13.4 but extends only from $5000 - 7500 \text{ \AA}$. Models of that epoch were used as a check for the models of day -11.5 and are not shown here. The distance to the galaxy is given as 35.5 Mpc ($\mu = 32.75$) and there is very little extinction of the SN light on our line of sight ($E(B - V) = 0.01$). The observational input parameters for the calculation are taken from Stanishev et al. (2004, in prep.).

7.1.2. SN 2002dj

Supernova 2002dj was the second target observed by the ESC. It was discovered on 2002 June 12.2 UT by Hutchings & Li (2002) and confirmed to be a SN Ia by Riello et al. (2002) two days later. SN 2002dj is hosted in the giant elliptical galaxy NGC 5018 at a distance of 39.4 Mpc ($\mu = 32.98$). Since there is no evidence of absorption from the host galaxy in the low resolution spectra of SN 2002dj, it is assumed $E(B - V) = 0.10$ as the colour excess due to the interstellar material in the Milky Way. The observations cover the spectral evolution of SN 2002dj from -10.9 to $+274$ days relative to B maximum.

Pignata et al. (2004, in prep.) find a remarkable similarity between SN 2002dj and SN 2002bo both from the photometric and spectroscopic points of view. The twin nature of the two SNe is highlighted by comparison of the expansion velocity evolution for several lines. The behaviour of the Si II 6350 Å doublet is nearly identical for both objects. A rather high velocity of the Si II line for SN 2002bo was found in the analysis of Section 5.3, and so is for SN 2002dj. The Ca II H&K doublet of SN 2002dj is significantly higher than in SN 2002bo, while the expansion velocity of the S II 5460 doublet is lower in SN 2002dj. The S II line forms near the photosphere indicating that SN 2002dj has a lower photospheric velocity. Pignata et al. also find a deeper S II 4553, 4568 Å absorption in the SN 2002dj spectrum at -6 days. Given the temperature sensitivity of this feature (Nugent et al. 1995b) this indicates a higher photospheric temperature.

The Ca II H&K doublet is formed in the outer layers of the ejecta. Higher velocities of this feature in SN 2002dj compared to SN 2002bo is a further indication of peculiar conditions in these regions. The Ca II IR triplet in SN 2002dj exhibits even higher velocities ($\gtrsim 18,000 \text{ km s}^{-1}$) but cannot be compared to SN 2002bo, since the observations do not include these wavelengths at early times (s. Sect. 5.3). The high-velocity component in this feature is visible in all pre-maximum spectra, decreasing slowly with time.

In order to analyse this issue we computed a synthetic spectrum for the earliest epoch. The observational input parameters are given by Pignata et al. (in prep.). Corresponding to a rise time of 19 d the epoch of the day -10.9 spectrum is 8.1 d. A luminosity of $\log_{10} L = 42.42$ (erg s^{-1}) emitted at a photospheric radius of $v_{ph} = 10,400 \text{ km s}^{-1}$ leads to a converged temperature at the inner boundary

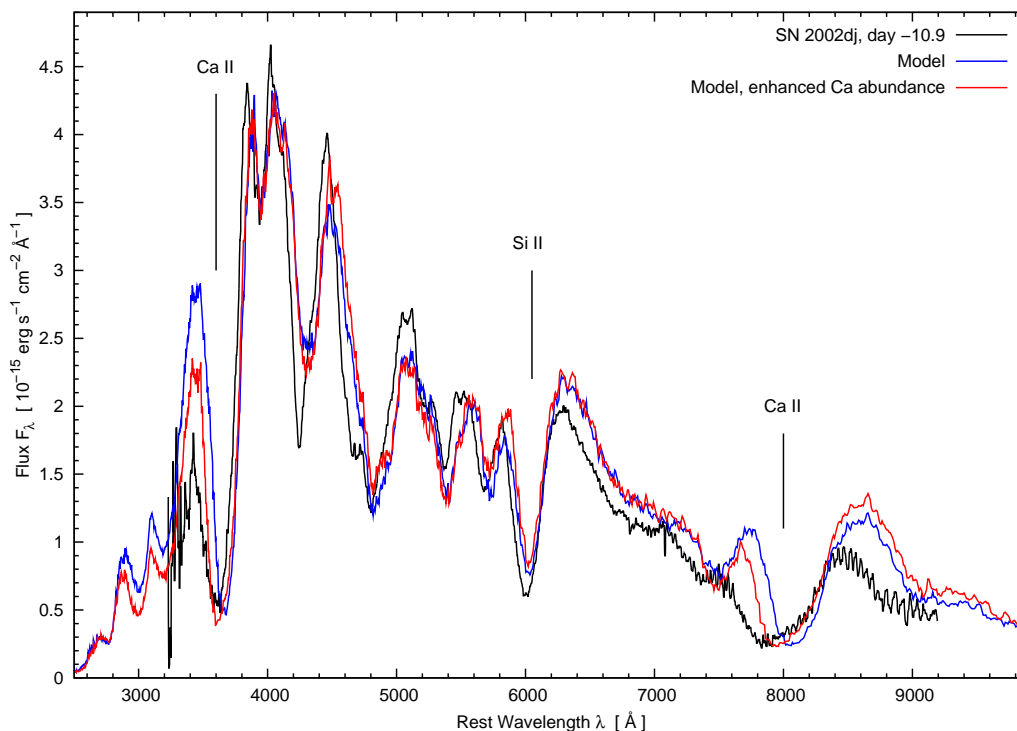


Figure 7.1.: Synthetic spectra of SN 2002dj at day -10.9 . The red model is calculated with an enhanced Ca abundance in the outer layers.

of $T_{BB} = 14,370$ K. The SN envelope is divided into four abundance shells above the photosphere. The inner radii of the three outermost shells are $14,000 \text{ km s}^{-1}$, $22,000 \text{ km s}^{-1}$, and $25,000 \text{ km s}^{-1}$, respectively. In Fig. 7.1 the synthetic spectrum (blue line) is shown in comparison with the observations and the high-velocity line features are labelled.

The overall shape of the spectrum can be reproduced rather well and all observed features are visible in the model. However, none of the model lines resembles the high-velocity component clearly seen in the spectrum. In particular the blue wing of the Ca II IR triplet is missing completely in the synthetic spectrum. But also the Si II line near 6000 \AA lacks high-velocity absorption in the model. This proves the need for a different solution to explain the high-velocity components.

7.1.3. SN 1999ee

A more subtle object in the context of high-velocity component is SN 1999ee, a otherwise normal SN Ia (Hamuy et al. 2002, Stritzinger et al. 2002). In Mazzali et al. (2005) we argue that in this case not only Ca II and possibly Fe II show high-velocity features, but that a sudden change in the shape of the profile and the position of Si II 6355 Å is due to the presence (and progressive thinning out) of a high-velocity Si component, which is identified for the first time in a SN Ia.

Optical and infrared spectra of SN 1999ee covering the period from -9 d to $+42$ days relative to B maximum were presented by Hamuy et al. (2002). SN 1999ee is a rather slow-decliner ($\Delta m_{15}(B) = 0.91$), but it does not show the spectroscopic peculiarities of SN 1991T and similar SNe. The spectral evolution and line identification are discussed by Hamuy et al. (2002).

Although the spectra of SN 1999ee look like those of a typical SN Ia, the Ca II IR triplet shows two small notches, separated by exactly the line separation of the two strongest components ($\lambda 8542$ and 8662 Å). The narrow features are first visible on day -2 , and persist until day $+3$, during which time their position does not change significantly, indicating that they are formed in a layer that is detached above the photosphere, with central velocity ~ 22000 km s $^{-1}$. This is similar to the SNe Ia discussed above, although in SN 1999ee the narrow features are not clearly separated from the main broad absorption, which is of photospheric origin. If these features are correctly identified, their weakness in the two earlier spectra (day -9 and -7) could result from the fact that the photosphere at those early epochs was located at velocities comparable to that of the narrow features. These would therefore blend almost completely with the broad component, resulting in a very broad Ca II IR triplet, as is indeed observed. The later disappearance of the narrow features, going from day $+3$ to day $+8$, is then the combined consequence of the decreasing density in the high-velocity zone caused by expansion and of the inward motion of the photosphere, which becomes removed from the detached Ca II zone. Fig. 7.2 shows how the Ca II IR triplet can be decomposed into three different components, one broad and two narrow. Fig. 7.3 shows the time evolution of the central velocity of each component. The broad photospheric absorption drops rather smoothly from $20,000$ to $15,000$ km s $^{-1}$, but the two detached features are clearly measured at velocities between $24,000$ and $20,000$ km s $^{-1}$ and then disappear.

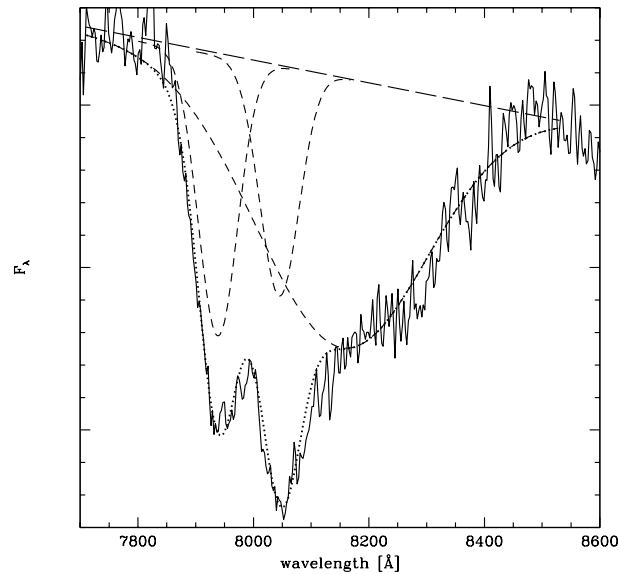


Figure 7.2.: Decomposition of the absorption part of the Ca II IR triplet into three gaussian components in SN 1999ee. The broad component is the blended photospheric feature, while the narrow ones are the high-velocity absorptions of the two strongest lines in the triplet.

There is however another piece of observational evidence, not as clear perhaps as that of the Ca II IR triplet but certainly at least as rich in physical implications: the sudden change in the shape of the Si II 6350 Å line between day -7 and day -2 . In the two earliest spectra, the line appears unusually blue (with a central wavelength of ~ 6000 Å, indicating a velocity of $\sim 16,000$ km s $^{-1}$). Additionally, it displays a P-Cygni profile which increases in strength towards the highest velocities, both in absorption and in emission, which is unusual for SNe Ia lines. After this phase, the line moves suddenly to the red, and it looks like a perfectly normal SN line on day $+3$. The velocity evolution of the Si II line is also shown in Fig. 7.3. After the sudden drop, the velocity of the line continues to decrease, but at a much lower rate.

The coincidence in time of the appearing of the Ca II narrow features and the redward shift of the Si II line, and then of the disappearing of the Ca II features and the return to normal of the Si II line suggests that these events may be correlated. The behaviour of the Si II line may also be due to the presence of high-velocity material, which makes the line appear at bluer wavelengths than

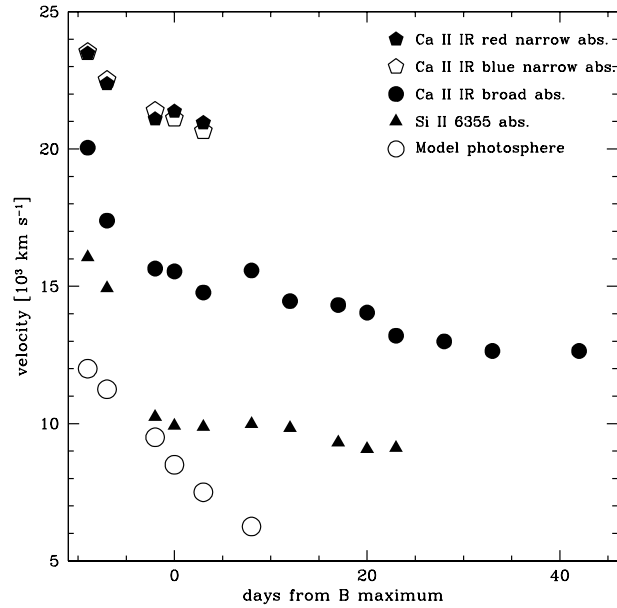


Figure 7.3.: Time evolution of the observed velocity of the Ca II IR triplet components, the Si II 6355 Å line, and the photospheric velocity adopted in model calculations for SN 1999ee.

usual at first. Later, as this material becomes optically thin, the line recovers its typical profile.

In order to locate accurately the regions responsible for the detached features and to describe realistically their physical properties, we modelled the sequence of spectra of SN 1999ee. As a first step, we tried to obtain reasonable fits to each spectrum across the observed wavelength range. For this we used the standard W7 density structure. We then modified the density and abundance distributions to reproduce the narrow Ca II features and the behaviour of the Si II line.

We have modelled all 6 available spectra, starting from the first one, at day -9 , and until day $+8$. This covers the time when the spectral anomalies are present. We tried to reproduce the global properties of the spectra, neglecting the narrow Ca II features or the fast Si II line when present. This step was necessary in order to define quantities such as the luminosity and the photospheric velocity, which we can compare to the observed velocities plotted in Fig. 7.3.

The series of model fits is shown in Fig. 7.4. The earliest spectra are sufficiently well reproduced, but then the quality of the fits becomes rapidly worse. Even

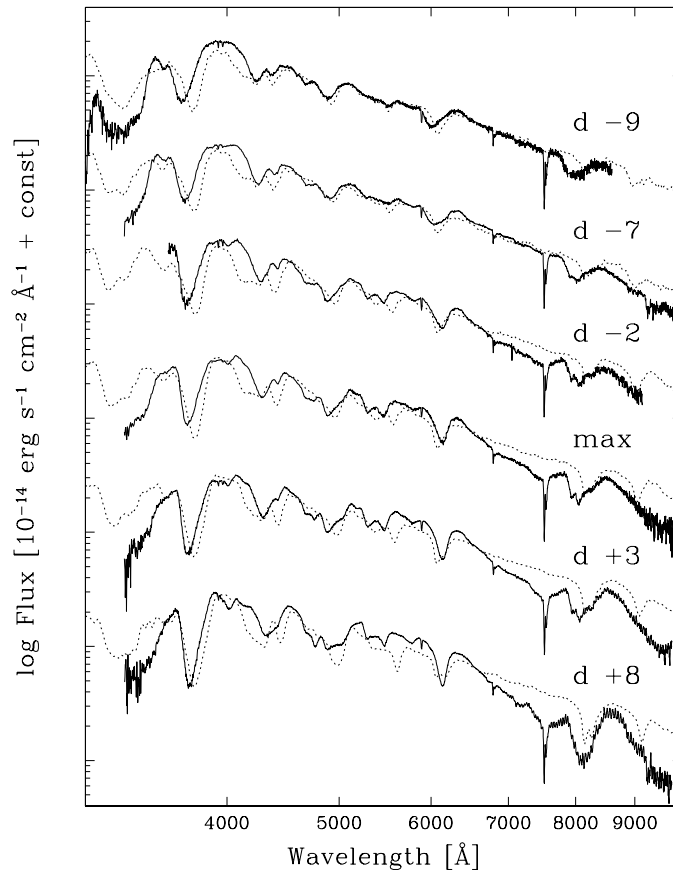


Figure 7.4.: Synthetic spectral sequence (dotted lines) of SN 1999ee using W7 densities and abundances.

at the earliest epochs, close inspection reveals defects caused by neglecting of the high-velocity components. In particular, looking at the first spectrum, the Ca II IR triplet and H&K doublet, and the Si II 6350 Å line are significantly too red in the model, while other features such as the absorptions near 4250 and 4900 Å, which are dominated by Fe III lines at this epoch, are correctly reproduced. This behaviour repeats at other epochs, including those where the narrow components are present.

Another shortcoming is that the models fail to reproduce the observations near 4700 Å. This is just blue of the Fe III-dominated absorption complex. At later epochs the feature is dominated by Fe II lines (multiplet 48). A rather similar feature in SN 1994D was attributed to high-velocity Fe II absorption by Hatano et al. (1999).

7.2. An abundance enhancement?

The first try to reproduce the various spectral anomalies is carried out by modifying the distribution in velocity space of the elements involved. Guided by the observed spectra, we introduced regions of increased abundances (relative to W7) of the elements in question at well defined velocities, trying to improve the synthetic spectra.

a) SN 2003du

The maximum light epoch for SN 2003du is assumed to be 19.5 d leading to an epoch of 8.0 d for the day -11.5 spectrum. A synthetic spectra is computed and shown in Fig. 7.5 together with the observed spectrum. The blue model represents the best fit using the normal W7 density distribution and an enhanced Ca abundance in the outer layers to account for the high-velocity component in the Ca II IR triplet. A stratified abundance distribution is used with five abundance shells above the photosphere. The four outer shells are located at $17,000 \text{ km s}^{-1}$, $19,850 \text{ km s}^{-1}$, $22,100 \text{ km s}^{-1}$, and $25,000 \text{ km s}^{-1}$, respectively where the innermost radius is determined by the photospheric radius of the models at day -13.4 .

The model is calculated with a photospheric velocity of $13,600 \text{ km s}^{-1}$ and a photospheric luminosity of $\log_{10} L = 42.67$ (erg s^{-1}). Ca is enhanced significantly compared to typical values of SNe Ia. The outermost shell contains purely Ca whereas the shell above $22,100 \text{ km s}^{-1}$ consists of 80% Ca and 20% other elements (O, Mg, Si, S, and Fe) relative abundances by mass.

The model reproduces the overall shape of the spectrum as well as the main features. However, there are significant discrepancies in some places. In particular the blue wing of Ca II IR triplet cannot be fitted with the normal W7 model, although the Ca abundance is enhanced enormously because the densities at velocities above $\sim 16,000 \text{ km s}^{-1}$ are too low and most of the photons escape the envelope before they interact with the line. The Ca II H&K doublet is not affected by the high-velocity component as seriously as the IR triplet. The H&K line has a lower optical depth and is therefore saturated more easily. The lack of density is substituted sufficiently by the abundance enhancement.

Another shortcoming of the model is the wavelength region around 4500 \AA .

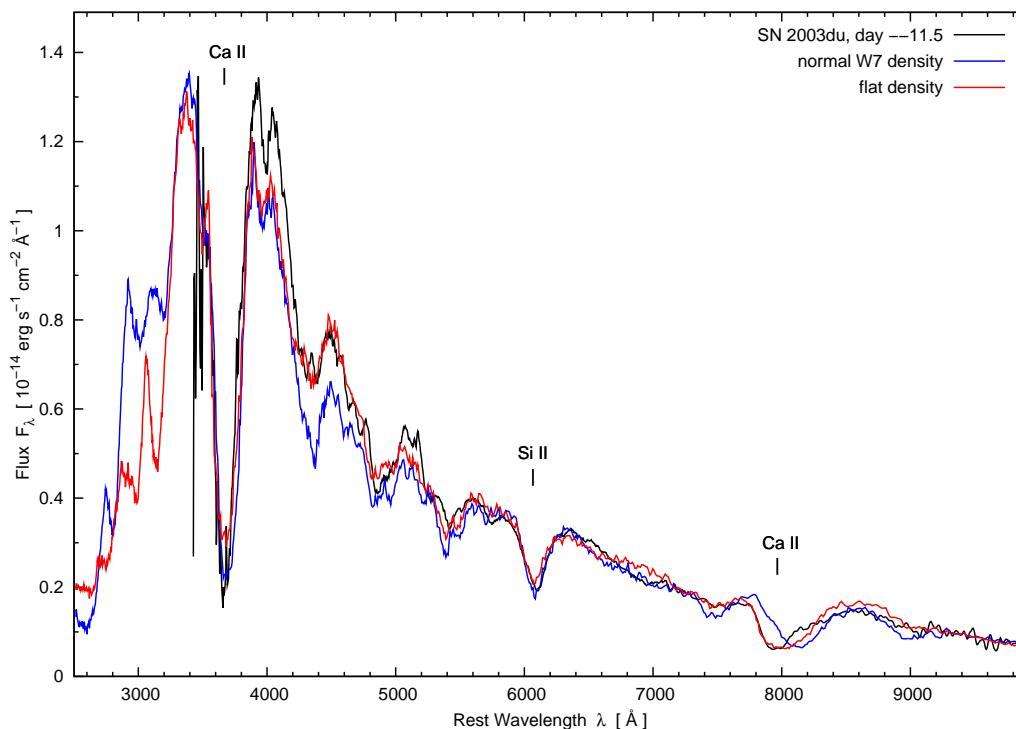


Figure 7.5.: Synthetic spectra of SN 2003du at day -11.5 using normal W7 density (blue) and flat density profile with Hydrogen (red).

The absorptions due to Fe III, Mg II, and Si III are strong compared to the observations. The overall ionisation level is very high in the synthetic spectrum leading to strong absorption of doubly ionised lines. The SN model atmosphere is therefore hotter and more flux is emitted in the UV.

b) SN 2002dj

The setup for the enhanced Ca model of SN 2002dj is the same as in Section 7.1.2 concerning luminosity, photospheric velocity, epoch, reddening, and density structure (W7). We also kept the boundaries of the abundance shells but the Ca abundances in the outer shells are enhanced. Each of them contains 80% of Ca relative abundance by mass leading to a total Ca mass of $0.025 M_{\odot}$ in this region. The synthetic spectra is shown in Fig. 7.1 (red line).

The enhanced Ca model is very similar to the synthetic spectra calculated with the W7-like abundances for Ca. Only the Ca II IR triplet is affected significantly.

As expected, the absorption extends more to the blue and is now closer to the observations. However, this is still not enough to account for the high-velocity component seen in the spectrum.

This mismatch applies to all line features in the model as well, since the abundances of the other elements are kept with respect to the previous calculation for SN 2002dj.

c) SN 1999ee

Starting from the first spectrum, we increased the abundance of Si by factors between 5 and 20 at velocities between about 16000 and 22000 km s⁻¹, and that of Ca by a factor of about 20 at velocities larger than about 20000 km s⁻¹. It is however not possible to reproduce the narrow features near 4700Å by simply increasing the Fe abundance. This in fact generates both Fe III and Fe II lines at high velocity, but there are Fe III-dominated absorptions, like that at 4250Å, that do not show high-velocity components. Therefore, we increased only the opacity of the Fe II in order to get a qualitative assessment of the possible role of high-velocity Fe II. The opacity of Fe II was increased by factors of $\sim 10^4$ at $v > 28000$ km s⁻¹. The results for the earliest spectrum are shown in Fig. 7.6. The position of the Si II and Ca II lines is now reproduced much better, and the absorption near 4700Å is reproduced as high-velocity Fe II, demonstrating the plausibility of the hypothesis that high-velocity components are responsible.

If high-velocity features are to be taken seriously it should be possible to reproduce their effect on the spectra consistently at all epochs. Therefore, we applied the enhancements to the abundances of Si, Ca, and Fe II in the velocity shells defined above, at all other epochs. The results are shown in Fig. 7.7. Remarkably, the adopted high-velocity distribution seems to give an excellent description of all observed peculiarities. The Si II line is still blue on day -7 ($\lambda \sim 6000\text{\AA}$), but in the next epoch, day -2, it has shifted by at least 150Å to the red. This is due to the reduced opacity of the high-velocity Si region, as the photosphere moves further inwards. The line is then reproduced well at all later epochs. As for Ca II, in the two earliest epochs the introduction of the high-abundance region leads only to a blueward shift of the absorption, since $v(ph) \sim v(det)$. At later epochs, however, the Ca II high-abundance region becomes detached. Since the velocity separation of the high-abundance region

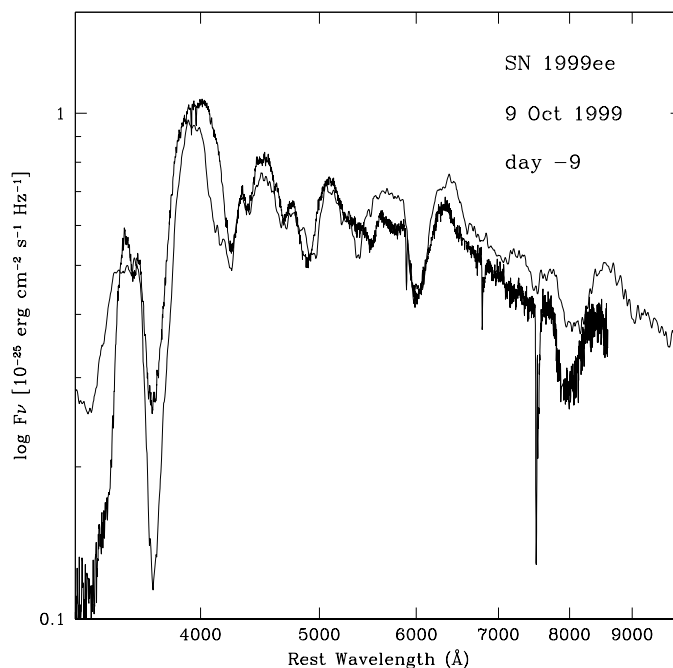


Figure 7.6.: Model for the Oct. 9 of SN 1999ee spectrum with increased abundances of Si, Ca, and increased optical depth of Fe II lines (thin line).

from the photosphere is much greater than the velocity separation of the two strongest lines in the triplet, which is in turn larger than the velocity width of the high-velocity region, the two narrow absorptions are formed. They persist - at the correct wavelength - until the last epoch, when they disappear as their optical depth becomes too small. As we remarked earlier, Ca II H&K does not show distinctly detached features. However, the introduction of the high-velocity component leads to significant line optical depth at high velocity, causing the line to shift bluewards. This is the case for all the six spectra modelled. Finally, the feature we tentatively attributed to Fe II is also reproduced very accurately in all except possibly the last epoch.

The modified abundances imply that the regions involved are dominated by Si ($\sim 90\%$ by mass), and have a high abundance of Ca ($\sim 10\%$ by mass). The Fe abundance can be low ($\sim 1\%$ by mass), but the ionisation degree of Fe must favour Fe II over Fe III. Wang et al. (2003) obtained rather similar values for SN 2001el. These abundances would imply significant burning of the outer layers of progenitor white dwarf (WD).

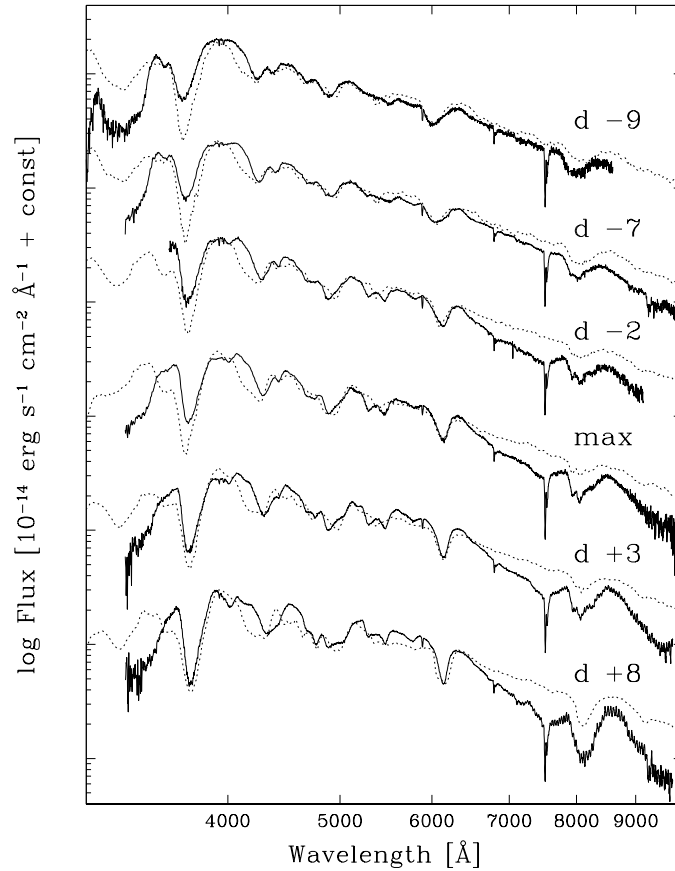


Figure 7.7.: Synthetic spectral series for SN 1999ee using the abundance distribution discussed in Section 7.2c (dotted lines).

Burned material such as Si may be produced at very high (but not the highest) velocities if the explosion mechanism was a delayed detonation (e.g. Höflich & Khokhlov (1996), Iwamoto et al. (1999)). Alternatively, in the deflagration model, a thin He envelope ($0.01M_{\odot}$) could be located in the outermost part of the WD and be burned by a precursor shock during the explosion; for a layer with densities as low as $\sim 10^5$ and $\sim 10^6$ g cm^{-3} , Si-rich and Ca-rich elements are synthesized, respectively (Hashimoto et al. 1983, Nomoto 1982b).

An alternative possibility might be that the outermost shells have a higher abundance of these species, preserving the metallicity of the progenitor (Lentz et al. 2000). The required abundance ratios seem however to high for this scenario.

Another relatively unexplored possibility is that He shell flashes during the

pre-SN evolution might produce elements such as Mg, Si, and Ca. The He flash is stronger for slower accretion, becoming stronger as the white dwarf approaches the Chandrasekhar mass (Nomoto 1982a).

7.3. A density enhancement?

A different possibility to obtain high-velocity features is an overall increase in density above what is predicted by W7. This was tested for the early spectra of SN 2003du and SN 2002dj. The results were comparable to a pure density enhancement and yet not satisfactory.

In the case of SN 1999ee the density increase may help explaining the low ionisation degree of Fe at high velocity. Therefore, in the next set of models, we increased the density in a few shells at high velocity, leaving the original W7 abundances unchanged.

In these models, there is much less freedom to change parameters to obtain a good fit, since the test is to determine whether changing the density in a number of shells can lead to all high-velocity features being reproduced consistently, and to verify that models with this density change reproduce the observed spectra at all epochs.

Since the high-velocity features appear at $v > 16000 \text{ km s}^{-1}$, we increased the density of the corresponding shells with respect to W7, without changing the abundances. We selected a set of density changes which allowed us to get a good fit of the day -9 spectrum. In this model, shown in Fig. 7.8, the density was increased by a factor 1.5 at $16750 < v < 20750 \text{ km s}^{-1}$, by a factor 8 at $20750 < v < 22500 \text{ km s}^{-1}$, and by a factor 5 at $v > 22500 \text{ km s}^{-1}$. The extra mass contained in the ‘bump’ is $0.1M_{\odot}$. This is a large increase of the mass at the highest velocities. Model W7, in fact, has only $\sim 0.07 M_{\odot}$ of material above 16750 km s^{-1} .

Increasing the density leads to much broader and bluer Ca II and Si II lines. The spectrum is very well reproduced, but the 4700\AA feature is not, although the ionisation of Fe is indeed reduced at the velocities where the density is enhanced. The Ca II IR triplet becomes broad, but it is still narrower than the observed profile.

We used this modified density distribution to compute spectra at all observed

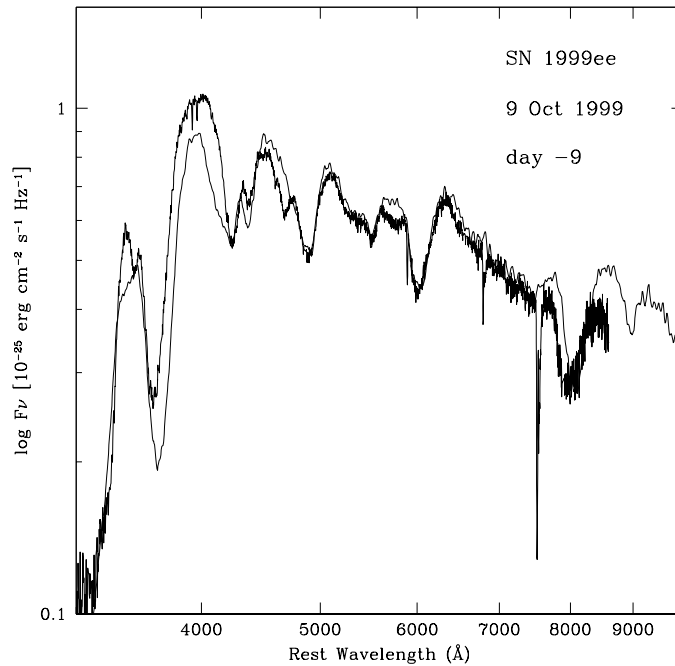


Figure 7.8.: Model for the Oct. 9 SN 1999ee spectrum with increased density at high velocity (thin line).

epochs. The results are shown in the sequence of Fig. 7.9. The change in density is able to explain both the sudden redward shift of the Si II line and the appearance of the narrow components in the Ca II IR triplet. The fact that the timing of the change is correctly reproduced confirms that both the position and the amount of the modification are correctly estimated.

A weak high-velocity Fe II absorption appears at 4700\AA in the spectra near maximum light. An increase in the Fe abundance as well as in density seems to be necessary to reproduce the feature as Fe II, so we cannot confirm this identification.

The quality of the fits suggests that an increase in density is a possibility that must be considered seriously at least for some objects. An overall variation of the density by this amount may occur if the explosion is not spherically symmetric, so that parts of the ejecta may be affected by burning differently from others. If these regions have sufficiently large angular scale, they may give rise to the observed spectral peculiarities. Polarisation measures in SN 2001el (Wang et al. 2003) may support this possibility.

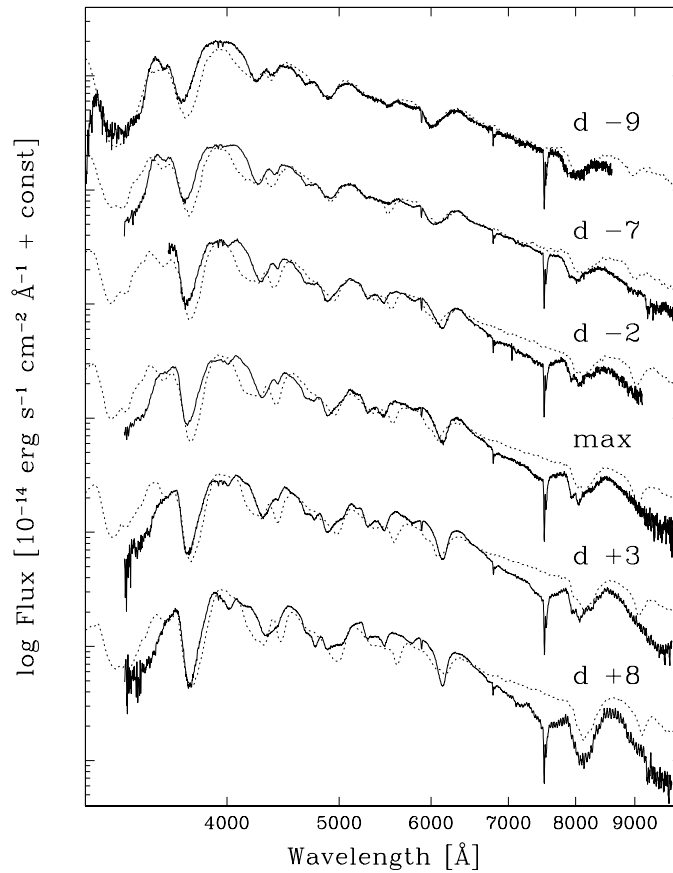


Figure 7.9.: Synthetic spectral series for SN 1999ee using the increased density discussed in Section 7.3 (dotted lines).

7.4. Circumstellar interaction?

In the models in the previous section, the full width of the Ca II IR triplet in the earliest spectrum was not reproduced, even though the density was significantly enhanced. One possibility would be to add even more mass at the highest velocities. However, it is probably not reasonable to expect that the deviation from the spherically symmetric density structure can be much larger than what we have used in the case of SN 1999ee. A different possibility to add mass at the highest velocities is the accumulation of circumstellar material.

If the SN ejecta interact with a circumstellar environment, it is most likely that the CSM composition is dominated by hydrogen. Therefore different amounts

of H are added to the outer shells. The limit is reached when H lines start to appear, since they are not visible in the observations.

a) SN 2003du

The model with the flat density profile shown in Fig. 7.5 (red line) is calculated with the same input parameters for the distance, the reddening and the epoch but with different abundances as described in Section 7.2a.

The photospheric radius in the flat model is located deeper in the ejecta than in the normal W7 model ($v_{ph} = 12,000 \text{ km s}^{-1}$). A slightly lower luminosity of $\log_{10} L = 42.65 \text{ (erg s}^{-1}\text{)}$ is emitted at the photosphere. The density profile is flattened relative to W7 (Nomoto et al. 1984) by adding $\sim 0.03 M_{\odot}$ above $18,500 \text{ km s}^{-1}$. The Ca abundance is slightly enhanced but not as dramatically as in the models in Section 7.2a (5% by mass in the outer two shells). Instead we used 70% H in the shells above $22,100 \text{ km s}^{-1}$ leading to a total H mass of $0.02 M_{\odot}$. This is a relatively small amount but has significant impact on the entire synthetic spectrum.

Most prominent is the effect in the Ca II IR triplet. Not only the correct depth of the line is reproduced by the model but also the velocity at which the line absorption occurs. The blue wing of the feature corresponds perfectly to the observations. Additionally, an improved behaviour of the model near 4500 \AA can be seen. The H_{α} line that is recognised in the model line list is hidden in the Si II 6350 \AA .

The effect caused by the H can be explained as follows: since the electron density is significantly increased when even a relatively small amount of H is added, recombination is favoured. Since at the highest velocities Ca is mostly doubly ionised, once H is introduced the fraction of Ca II increases (by factors between 3 and 6 in the zones affected for the particular model we used). This leads to an increased strength of the Ca II lines and to the observed broader absorption. A second-order effect is also at play. A higher electron density means that photons have a higher probability of scattering off electrons. This results in a longer residence time of photons in the H-rich shells, and thus in turn in a higher probability that photons can interact with spectral lines. The effect of this is an increased line absorption - in all lines - at the highest velocities, since that is where the electron density effect is at play. Since the Ca II lines are

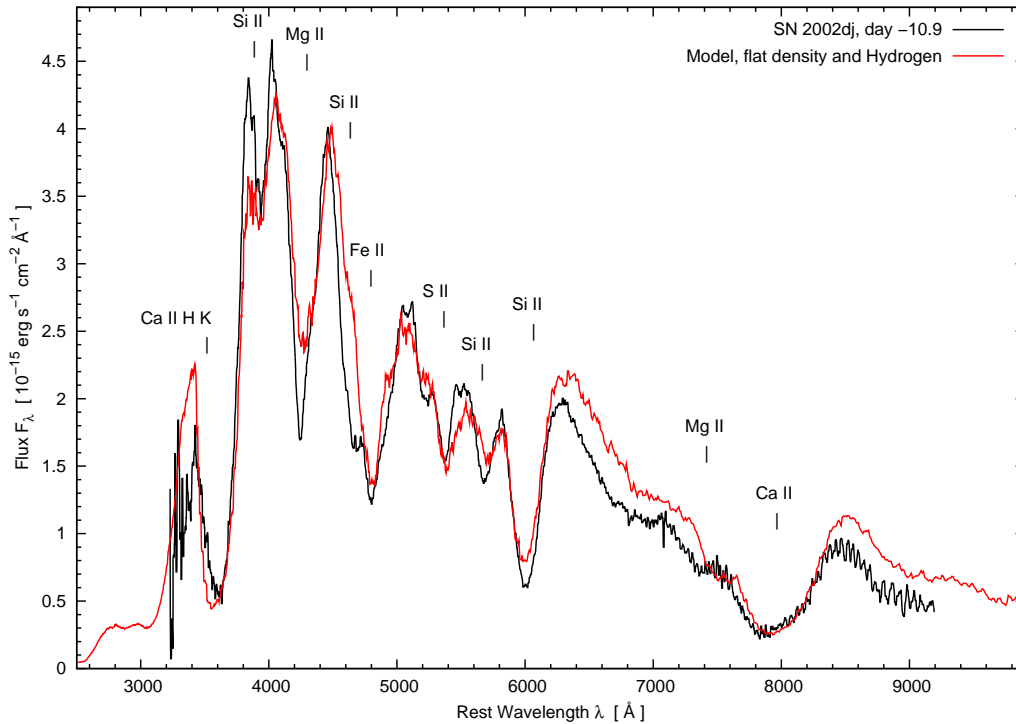


Figure 7.10.: Synthetic spectrum of SN 2002dj at day -10.9 using flat density profile and a $0.04 M_{\odot}$ Hydrogen outer shell.

the strongest in the optical spectrum, they are also the most affected. Electron scattering opacity is also responsible for the partial suppression of the peak near 4000 \AA .

b) SN 2002dj

In the case of SN 2002dj we used a flat density profile based on W7 with an increase of $0.06 M_{\odot}$ above $18,500 \text{ km s}^{-1}$. Apart from that the input parameters are the same as in the previous models for SN 2002dj. The H content in the outer two shells is $0.04 M_{\odot}$.

The model (Fig. 7.10) reproduces the observed spectrum very well. Most of the line features closely resemble the observations both in line strength and line profile. A remarkable mismatch can only be seen in the peaks near 4000 \AA and 5500 \AA and in the absorption depth of the Mg II 4481 \AA feature. The suppression of the peaks is due to the H as explained above. The large line ratio of the two

Si II lines near 6000 Å indicates a low temperature (Nugent et al. 1995b). Since the photospheric velocity is relatively low for an epoch of 8.1 d, the temperature of the model at the inner boundary is high. This leads to a triple ionisation near the photosphere of many ions, in particular Si. The strong Si II lines seen in the observations are formed further out in the ejecta where the temperature is sufficiently low. The density enhancement in the outer parts causes the photons to interact with lines at high velocities where they otherwise would just escape.

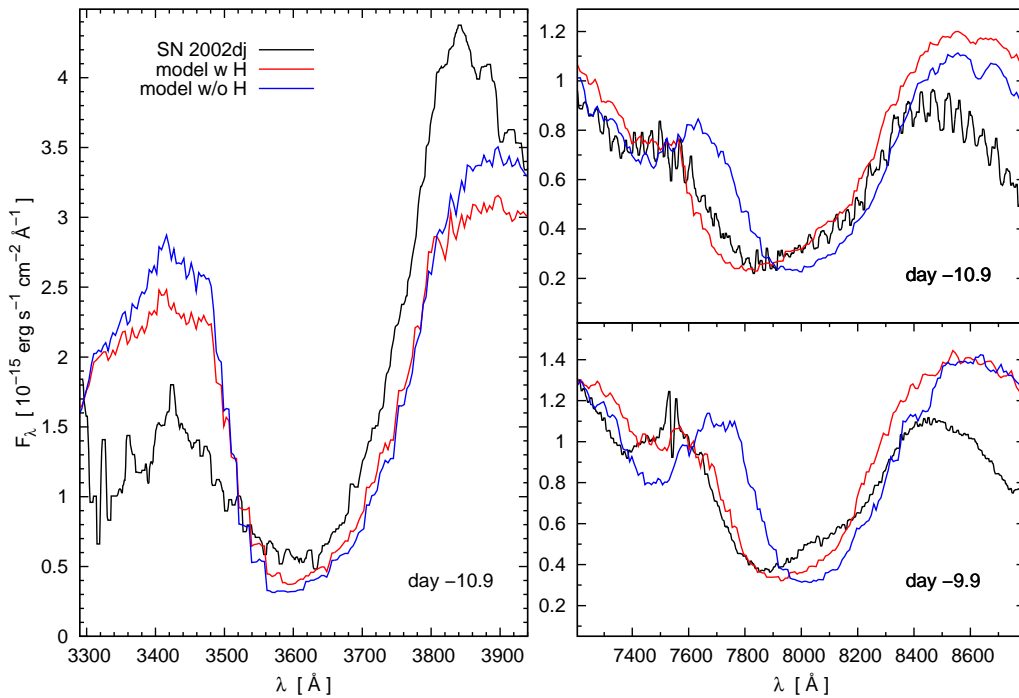


Figure 7.11.: The effect of H on the Ca II H&K doublet and Ca II IR triplet in SN 2002dj

The high-density outer regions with the H are necessary to fit the Ca II IR triplet correctly. Moreover, the H effect improves the line profiles in all features owing to the increased absorptions at high velocities. Thus, the missing high-velocity absorption in the Si II lines is now fixed in the model.

Figure 7.11 demonstrates the different strength of the effect to the two Ca II features seen in the spectrum. The Ca II H&K doublet is saturated even in the case of no H while the Ca II IR triplet strongly depends on the H in order to achieve the high-velocity component.

c) SN 1999ee

For SN 1999ee we tested different ways of adding hydrogen in the spectrum on day -9 , taking only thermal effects into account. In each test, the limiting value of the H mass was constrained by the strength of the synthetic H_α line. H_α is in fact not visible in the observed spectra.

First, starting from the modified W7 density distribution that we derived in the previous section, we introduced H uniformly in the ejecta at $v > 11250 \text{ km s}^{-1}$. This was done by simultaneously reducing the abundances of all other elements. With this method we obtained an upper limit for the H mass of $0.021 M_\odot$, corresponding to a H abundance of 4% H by mass, which is actually $\sim 50\%$ by number. Although H_α is produced at this point, no changes are seen in either the Ca II or the Si II line profiles.

Then we assumed that only the outermost parts of the modified density structure contains hydrogen, 50% by mass, to simulate the piling up of CSM material, and increased this H shell inwards. It is sufficient to introduce H above 25000 km s^{-1} to see a change in the synthetic Ca II IR triplet. Although H_α is not seen, the presence of H has an indirect influence on the spectra, making the Ca II IR triplet significantly broader (Fig. 7.12). The total H mass in this model is $0.004 M_\odot$.

7.5. Discussion

We have shown that a modification of the abundances or an increase of the mass at the highest ejecta velocities can explain the high velocity features observed in the spectra of SN 2003du, SN 2002dj, and SN 1999ee. The former situation might result from the nuclear burning reaching the outermost layers of the white dwarf. The outer layers must contain mostly products of incomplete burning, in particular Si, and some Fe. A change of the density structure could be due to either a non spherical deviation from the average properties of the explosion, or to the accumulation of CSM material.

If the bump in density is due to SN material, it should contain $\sim 0.1 M_\odot$ of material. This is a rather large change. However, it is quite possible that what we can reproduce as a ‘density bump’ in one-dimensional models may actually be just a ‘density blob’ in three dimensions. Attempts have been made

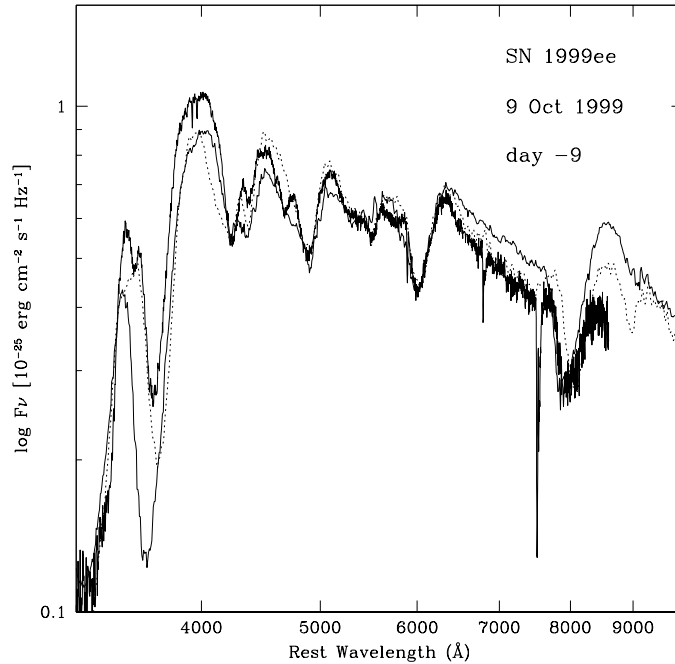


Figure 7.12.: Model for the Oct. 9 SN 1999ee spectrum using the increased density of Section 7.3 but with an outer $0.004 M_{\odot}$ of Hydrogen (thin line). The model without H shown in Fig. 7.8 is also shown here as a dotted line for comparison.

to model detached components as blobs in 3-D (Kasen et al. 2004). Unfortunately, spectropolarimetric data are not available for our objects, and so the geometry cannot be constrained, resulting in a degeneracy of solutions.

Qualitatively, in order to reproduce the observed spectral signatures, any blob must not be too small in size compared to the size of the photosphere. If one such blob is observed because it happens to lie along our line-of-sight, chances are that at least a few others are ejected. To support this, we note that two separate sets of high-velocity features were observed in SN 2000cx. It is a matter of probability to determine the optimal number and size of such blobs so that they are only observed in a few SNe. Unfortunately, the blobs become too thin to be visible as narrow emissions in the nebular spectra, where a head count would be much easier since radiative transport is not an issue. The question whether a global density enhancement or a blob are to be preferred could be resolved with more spectropolarimetric observations. Both SN 2001el (Wang et al. 2003) and SN 2004dt show polarisation at early epochs.

If however we assume that H-dominated CSM material is piled at the highest velocities, the enhanced electron density causes the ionisation degree to be lower in those regions. Line broadening is then caused by the increased optical depth of the Ca II IR triplet. This can explain the high-velocity components in SN 2003du and SN 2002dj in an appreciable way. The calculations for SN 1999ee cannot by themselves prove that the spectral peculiarities – at least partially – due to an outer shell of H, since the H mass we used is much smaller than the mass added by modifying the density profile. Still, it is another strong hint for the correctness of this interpretation.

In view of the mounting evidence that SNe Ia can indeed interact with CSM (e.g. Hamuy et al. 2003, Deng et al. 2004), it will be interesting to really verify whether models where the only density enhancement is due to H-rich material can account for the high-velocity components. A very important test in this context is to see whether this model can also reproduce the remaining spectra of SN 2003du and SN 2002dj that are not analysed in this work. Applying the Abundance Tomography method to these objects will improve our knowledge significantly in the near future.

8. UV spectra of Type Ia Supernovae

The UV part of a SN Ia spectrum is crucial for the line formation not only for the blue part of the spectrum but it affects all wavelength regions. In this Chapter, the influence of the UV on the emergent spectrum, owing to the effect of line blocking, is described. In Section 8.1, the physics of line blocking and the impact on the ionisation and the radiation field in the SN envelope are explained. We show in Section 8.2 how the MC approach deals with line blocking and how it is implemented in our MC code. Synthetic spectra are calculated and compared to SN 2001eh and SN 2001ep both of which have also been observed in the UV.

8.1. The line blocking effect

Due to the large velocity gradients in SN envelopes, the UV part of the spectra, which is otherwise almost free from continuous absorption (the redmost important ground state ionisation edge being Ca II at 1044 \AA), is effectively blocked by the superposition within the expanding envelope of the thousands of strong metal lines. As these photons travel through the ejecta, they suffer an increasing redshift relative to the surrounding material due to the homologous expansion of the SN envelope. This brings them into resonance with redder and redder lines. The number of lines can be very large, since the ejected matter reaches velocities of more than $20,000 \text{ km s}^{-1}$. The line overlap becomes very strong, especially in the UV where the metal lines crowd densely. The photons are trapped in this line forest and only escape, if they are scattered to longer wavelengths where the line opacity is much lower.

The effect of line blocking is to reduce the intensity of the radiation field in the UV. This affects strongly the emergent spectrum, since the peak intensity of the radiation emitted at the photosphere falls just in this wavelength region at typical photospheric temperatures of the order of $10,000 \text{ K}$. If line blocking was absent, the spectrum in the visible and IR parts would be essentially featureless.

UV photons would simply escape the ejecta at roughly the wavelength they are emitted rather than being shifted to the red.

Supernova envelopes contain many ions with high lying excited states from which photoionisation at optical wavelengths can occur (e.g. Fe II, Co II, Si II, Ca II). This is very important, because the relatively flat density profile in SNe favours the population of the excited levels. Since the excited states absorb radiation from the optically thin regions, photoionisation from these levels is preferred to photoionisation from the ground states. This leads to a much higher radiation temperature compared to the local temperature, which in turn makes the photoionisation from excited levels very efficient. Line blocking on the other hand decreases the overall degree of ionisation by reducing photoionisation from excited levels and influences indirectly the level populations. Line blocking has a strong impact on the ionisation structure and the radiation field and thus on the emergent spectrum.

8.2. Monte Carlo treatment of the UV

Given the strong influence of the line blocking on the spectra formation in SNe Ia, it is absolutely necessary to treat this process correctly in synthetic spectra calculations. Radiation transport techniques which solve the coupled equations of the radiation field and the level populations encounter a severe difficulty in computing this effect. They must explicitly take into account a very large number of lines simultaneously, which increases the computation time enormously. The MC approach in contrast deals intrinsically with line blocking. As described in detail in Section 4.2.4, individual energy packets are followed on their path through the SN envelope, where they can interact only with single lines, if they are redshifted to the resonance wavelength of the line.

Line blocking leads to large backscattering of the high-frequency continuum photons, i.e. they have a high probability to be reabsorbed in the photosphere after suffering several interactions with metal lines in the innermost part of the ejecta. Photons that are reabsorbed in the photosphere exit the MC experiment (Mazzali et al. 1992) and contribute only to the backwarming effect by increasing the black body temperature at the photosphere.

The branching treatment of the line emissions (Sect. 4.2.4) is also very impor-

tant for the spectral synthesis for two reasons: (1) Photons that are absorbed by one of the lines in the line blocking region have a realistic chance to ‘jump’ to a much redder wavelength where the line opacity is lower and it is easier to escape the ejecta. Without branching a photon scatters many more times and it is much more likely reabsorbed in the photosphere than transferred to such a line-free window. Thus, the backwarming is overestimated leading to a higher photospheric temperature. (2) Although branching is mostly from blue to red, some blue and UV photons are also generated by decays down to low-lying levels in the outer part of the envelope. This process of ‘reversely fluorescence’ is very important, since these photons do not see the line blocking effect and can escape the ejecta rather easily. They give rise to the emergent UV flux, which is otherwise suppressed too strongly compared to the observations (Pauldrach et al. 1996).

8.3. Models of UV spectra

Since the UV part has such a big influence on the entire spectrum, it is crucial to have reliable models of this spectral region. Unfortunately, only very few UV spectra have been observed and analysed in the past (e.g. SN 1992A, Kirshner et al. 1993, Nugent et al. 1995a, Pauldrach et al. 1996), and spectral synthesis calculations must be trusted blindly. The lack of observations is due to the fact that these wavelengths can only be observed with orbiting instruments, because the UV radiation is absorbed in the atmosphere before it reaches the Earth. Aiming at a full understanding of SNe Ia and being aware of the importance of UV spectra for this purpose, the ESC in a worldwide collaboration with many institutes of the SNe Ia community started recently a programme on UV spectral and photometrical observations with the Hubble Space Telescope. The synthetic spectra of SN 2001eh and SN 2001ep, shown in the following Sections, prove the ability of our MC code to make scientific use of these data.

8.3.1. SN 2001eh

Supernova 2001eh was discovered on 2001 August 31.5 UT by Ganeshalingam et al. (2001) 38".3 west and 4".7 north of the nucleus of UGC 1162. The early-time spectra closely resemble those of the normal SN Ia 1990N. Sixteen optical

Table 8.1.: Abundances of SN 2001eh on day 10 ($t_{exp} = 29.5$ d). The total mass of the SN envelope above the photosphere at that time is $0.72 M_{\odot}$.

Species	Chemical abundances (M_{\odot})			
	Inner radii of the abundance shells (km s^{-1})			
	7800	9000	11,000	15,000
O	4.08E-02	8.39E-02	1.34E-01	2.08E-02
Na	2.68E-02	2.15E-02	0.00E+00	0.00E+00
Mg	0.00E+00	6.11E-03	4.07E-02	2.71E-03
Si	9.78E-03	3.12E-02	5.42E-02	2.71E-03
S	7.90E-03	1.52E-02	1.90E-02	8.14E-04
Ca	3.64E-04	9.72E-04	1.36E-03	0.00E+00
Ti	2.84E-05	3.88E-05	5.42E-05	5.43E-06
Cr	2.84E-05	3.88E-05	5.42E-05	5.43E-06
Fe	9.79E-03	9.20E-03	1.90E-03	1.90E-05
Co	4.72E-02	2.77E-02	1.14E-02	1.14E-04
Ni	9.27E-04	5.43E-04	2.24E-04	2.25E-06

spectra were taken between day -4 and about two months after maximum[†]. The SN was observed with the HST twice, on October 26 and on November 4. The earlier HST spectrum is combined with the ground-based observations of the same day and is used for the modelling. The light curves have not yet been derived from the photometry, thus the epoch is not exact and is estimated to 10 d after maximum light (T. Matheson, priv. comm.). Assuming a typical rise time of SNe Ia of 19.5 d (Riess et al. 1999a) for SN 2001eh the spectrum corresponds to an epoch of 29.5 d. At this time the SN is about to pass into the nebular phase where the Schuster-Schwarzschild approximation becomes less valid. This makes it slightly difficult to calculate a synthetic spectrum with the MC code for which the existence of a photosphere is a basic assumption. However, problems are expected to occur only the red part of the spectrum. In the UV part, where we focus on in this analysis, the photosphere is still a sound approximation.

The host galaxy has a recession velocity of $11,103 \text{ km s}^{-1}$ leading to a distance modulus of $\mu = 35.85$ ($H_0 = 75 \text{ km s}^{-1} \text{ Mpc}^{-1}$). The reddening of the SN is

[†]We would like to thank T. Matheson from the Harvard-Smithsonian Center for Astrophysics, Cambridge, MA, USA for making the unpublished data of SN 2001eh and SN 2001ep available to us.

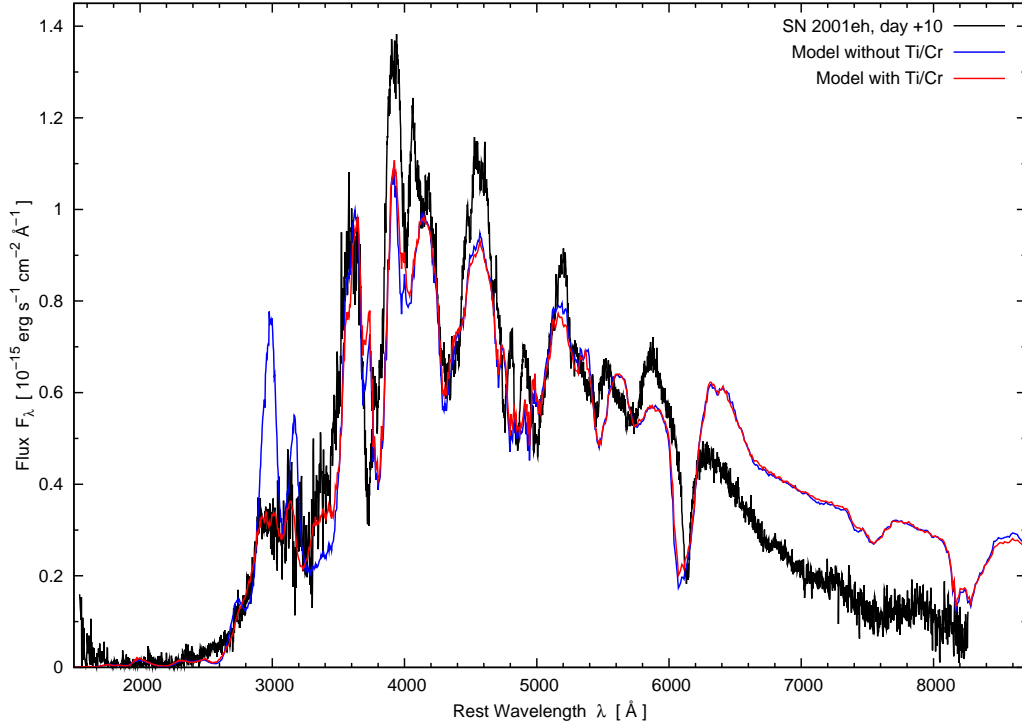


Figure 8.1.: Synthetic spectra of SN 2001eh at day +10 showing the effect of Titanium on the UV.

$E(B - V) = 0.06$. The model is calculated with these input parameters and the procedure explained in Section 4.3. The SN envelope is divided into 4 abundance shells above the photosphere at 7800 km s^{-1} . The inner boundaries of the outer shells are located at 9000 km s^{-1} , $11,000 \text{ km s}^{-1}$, and $15,000 \text{ km s}^{-1}$, respectively. The abundances are not stratified by the Abundance Tomography procedure but derived iteratively to reproduce the observed spectrum. Table 8.1 gives the abundances of each element that is used in the model calculation for the various shells.

The emitted luminosity of $\log_{10} L = 43.06 \text{ (erg s}^{-1}\text{)}$ leads to a converged photospheric temperature of $T_{BB} = 8990 \text{ K}$. At this epoch the spectrum begins to be dominated by Fe group elements, namely Fe II and Co II, although lines of IME are still visible mainly the optical. The best fit model is shown in Fig. 8.1 (red line).

We identify the rather broad absorption feature near 7500 Å as a blend of O I 7772 Å and Mg II $7877, 7896 \text{ Å}$. The deep line at $\sim 6100 \text{ Å}$ corresponds to

Si II 6350 Å. The weaker Si II 5958, 5979 Å line is blended by Na I 5892 Å. The Na I line typically only appears a few days after maximum. Next to the red we find S II 5454, 5606 Å. The three narrow features in the range 4700 – 5050 Å are Fe II 5169 Å, Fe II 5018 Å, and Fe II 4924 Å from red to blue, respectively. The broad line near 4300 Å is identified as Mg II 4481 Å, which is somewhat unusual at this epoch. Fe II 4233 Å and Co II 4161 Å compose the absorption at ~ 4050 Å followed by the strong Ca II H&K near 3700 Å.

In the UV part bluewards from the Ca II H&K, individual lines cannot be distinguished. Hundreds of lines block the flux nearly completely, especially below ~ 2800 Å, and give rise to the pseudo-continuum discussed in Section 8.1. We identify strong Co II and Fe II lines as well as many Ni II, Ti II, and Cr II absorption features of intermediate and smaller strength. In addition to the best fit model in Fig. 8.1 a synthetic spectrum with the same input parameters as before but without Ti and Cr is shown. The impact of these two elements on the UV is enormous. Although the total mass of both elements together is only $1.24 \times 10^{-4} M_{\odot}$ ($\sim 0.02\%$ of the SN envelope above 7800 km s^{-1}), their many lines contribute very efficiently to the line blocking effect. They are necessary to block the flux at ~ 2950 Å and ~ 3150 Å where the opacities of Fe II and Co II are low.

In the UV part, which is the most important in this analysis, the synthetic spectrum reproduces the observations very well. The model is not as good in the optical part compared to the observed spectrum but shows all main line features. Even the three narrow Fe lines just below 5000 Å are reproduced in the model.

8.3.2. SN 2001ep

Supernova 2001ep is another object that was observed with the HST. It was discovered on 2001 October 3.5 UT by Hutchings & Li (2001) and was spectroscopically confirmed to be a SN Ia by Matheson et al. (2001). SN 2001ep belongs to the galaxy NGC 1699. The observations provide us with 24 optical and 2 HST spectra (T. Matheson, priv. comm.). The earlier HST spectrum again was taken ~ 10 days after maximum light and is combined with the corresponding observations of the optical wavelengths at the same epoch. We used the same procedure as before to estimate the time since the explosion which gives again 29.5 d. The distance to the SN is 50.12 Mpc ($\mu = 33.50$) and the reddening $E(B - V)$ is 0.05.

Table 8.2.: Abundances of SN 2001ep on day 10 ($t_{exp} = 29.5$ d). The total mass of the SN envelope above the photosphere at that time is $0.86 M_{\odot}$.

Species	Chemical abundances (M_{\odot})			
	Inner radii of the abundance shells (km s^{-1})			
	6500	8500	10,000	13,000
O	4.08E-02	8.39E-02	1.34E-01	2.08E-02
Na	2.68E-02	2.15E-02	0.00E+00	0.00E+00
Mg	0.00E+00	6.11E-03	4.07E-02	2.71E-03
Si	9.78E-03	3.12E-02	5.42E-02	2.71E-03
S	7.90E-03	1.52E-02	1.90E-02	8.14E-04
Ca	3.64E-04	9.72E-04	1.36E-03	0.00E+00
Ti	2.84E-05	3.88E-05	5.42E-05	5.43E-06
Cr	2.84E-05	3.88E-05	5.42E-05	5.43E-06
Fe	9.79E-03	9.20E-03	1.90E-03	1.90E-05
Co	4.72E-02	2.77E-02	1.14E-02	1.14E-04
Ni	9.27E-04	5.43E-04	2.24E-04	2.25E-06

This time the photospheric velocity amounts to 6500 km s^{-1} and the abundance shells are located at 8500 km s^{-1} , $10,000 \text{ km s}^{-1}$, and $13,000 \text{ km s}^{-1}$, respectively with their abundances given in Table 8.2.

Figure 8.2 shows the observed spectrum together with two synthetic spectra with and without Ti and Cr, respectively. In the best fit model (red line) a photospheric luminosity of $\log_{10} L = 42.81$ (erg s^{-1}) is used. This leads to a converged photospheric temperature of 8930 K . The main features are labelled in the Fig. and are equivalent to the lines in the SN 2001eh spectrum even though they are differently pronounced. Since we find less Mg in SN 2001ep, the absorption near 7500 \AA consists only of O I 7772 \AA and the Mg II 4481 \AA is weaker and blended with lines of Ti II, Fe II, and Co II. The S II 5606 \AA line is weaker, too, and the absorption at $\sim 5800 \text{ \AA}$ contains mainly the Na I 5892 \AA line and less contribution of the Si II $5958, 5979 \text{ \AA}$ lines. In the case of SN 2001ep the observed spectrum extends to almost $10,000 \text{ \AA}$ and we can see the Ca II IR triplet.

The best fit model reproduces the observations very well, especially in the UV, where the flux profile of SN 2001ep is rendered almost perfectly. Comparing the two models in Fig. 8.2, which are identical except for the Ti/Cr abundance, the striking influence of these species can be seen directly. The combined total mass

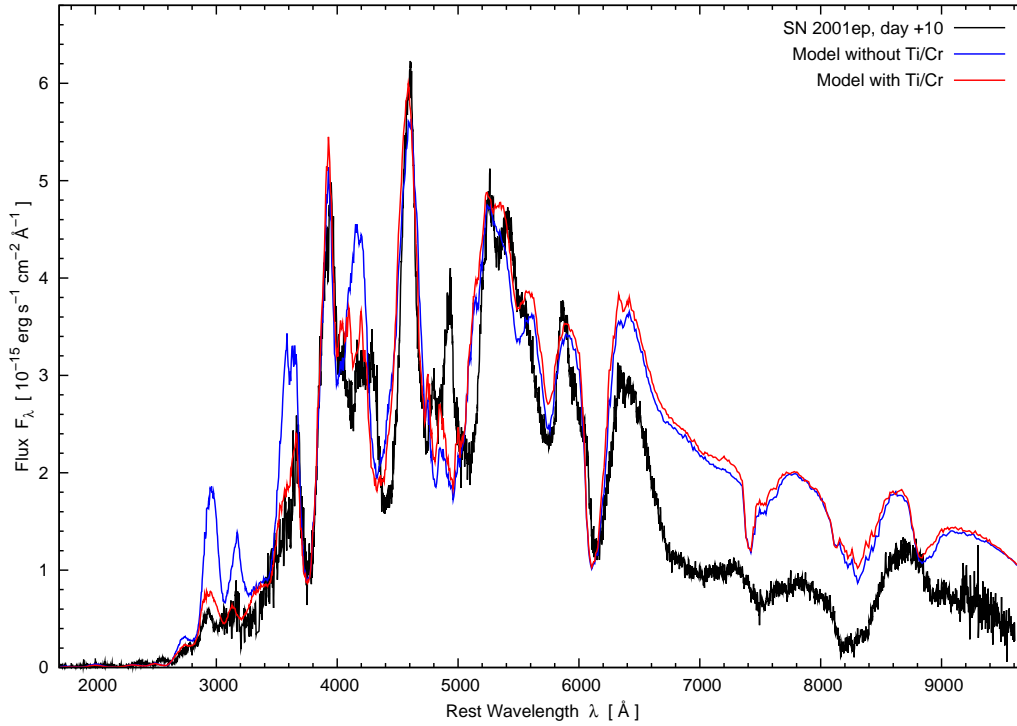


Figure 8.2.: Synthetic spectra of SN 2001ep at day +10 showing the influence of Titanium on the UV.

of the two elements is $1.18 \times 10^{-2} M_{\odot}$ corresponding to 1.4% of the total envelope mass above the photosphere. This value is higher than in the previous model but still at an acceptable level.

8.4. Conclusion

In this Chapter we proved the ability of our MC code to treat the line blocking effect in the UV spectra of SNe Ia. The synthetic spectra reproduce the HST observations of SN 2001eh and SN 2001ep very well. Only in the red parts of the two spectra the models exhibit a significant discrepancy. The higher flux in the model can be explained with the shortcoming of the Schuster-Schwarzschild approximation at that epoch.

A very interesting point is the importance of Ti and Cr for the line blocking effect and thus the spectra formation especially in the UV. This also confirms the significance of this wavelength region to be covered by the observations in order

to further our understanding of SNe Ia. Although we did not apply the complete Abundance Tomography method to these objects, we could substantiate the importance of abundance analyses.

The HST campaign initiated by the ESC is a valuable extent of SNe Ia observations. The MC method can contribute significantly to the analyses when the programme finally delivers spectral data.

9. Conclusions

The goal of this thesis was to improve methods of radiation transport calculations and to further our knowledge about the physics of Type Ia Supernovae (SNe Ia) by means of spectral synthesis. The analyses were focused on the early phase of very well observed nearby SNe Ia. The different approaches to carry out spectral synthesis calculations were introduced in Chapter 3 followed by a detailed description of the original MC method in Chapter 4. In Chapter 5, the new method of Abundance Tomography is motivated and the implementation in the Monte Carlo (MC) procedure is laid out. The Abundance Tomography method is applied to the normal SN 2002bo. In Chapter 6, we improved a shortcoming of the original code by modifying the function describing the incident radiation field at the photospheric radius. The flux redistribution was tested and exemplified by means of synthetic spectra calculations of SN 2002er. The evidence of indirect signs of H in SNe Ia spectra caused by interaction with circumstellar material were discussed in Chapter 7. In Chapter 8, we finally focussed on the UV part of the spectra and discussed the MC treatment of this important wavelength region in SNe. Models for spectra of SN 2001ep and SN 2001eh, which were observed with the Hubble Space Telescope (HST), demonstrated the ability of the MC approach to handle this issue.

9.1. Improvements to synthetic spectra calculations and their impact on astrophysics and cosmology

The previous MC code proved over many years to be a very powerful and efficient tool for spectral synthesis by several successful and detailed analyses. The Abundance Tomography procedure presented in this work turns out to be a valuable and important enhancement of the precursor version. Other approaches only use a homogenous abundance distribution and there was never before an

attempt to resolve the chemical composition of a SN ejecta from high-velocity outer regions down to the centre. Thanks to the excellent time coverage of the observed spectra provided by the European Supernova Collaboration (ESC), it was possible to resolve the abundance layers in SN 2002bo with an accuracy of better than 1000 km s^{-1} in most of the radial velocity regions.

Applied to the early time spectra of SN 2002er, the “modified black body function” was shown to improve the calculations of synthetic spectra. The redistribution of the emergent flux at the photosphere represents the natural situation much better than the unmodified Planck function does. This new approach makes excellent use of the branching already implemented in the code a few years ago. Moreover, in addition to the improvement of the temperature and ionisation structure by using a stratified abundance distribution, this method furthers our effort to achieve a more realistic description of the physical conditions in SNe Ia. Redistribution of the excessive red flux to shorter wavelengths, where in fact most of the radiation is emitted, leads to lower luminosities needed in the model calculations and hence to a lower temperature, which then reproduces the observed line features much more accurately.

The great success of the Abundance Tomography of SN 2002bo is the consistency of the abundances derived from the early time spectra with the spectral synthesis of the nebular phase. The abundances above $\sim 7500 \text{ km s}^{-1}$ directly entered the late phase calculation and complemented nicely the abundances of the inner ejecta.

Furthermore, the opacities for a bolometric light curve synthesis were calculated by means of the previously determined abundance distribution. The observed bolometric light curve, and most important the rise to maximum light, was perfectly reproduced using these opacities. That kind of approach has not been carried out before to calculate SNe light curves. The light curve check was independent from the spectral analysis and confirmed spectacularly the correctness and accuracy of the Abundance Tomography method.

The abundance distribution in the SN envelope plays the major role for the understanding of the diversity of the nearby SNe Ia. Understanding the diversity is in turn essential to draw reliable conclusions for cosmology. The Abundance

Tomography procedure delivers the key to address these issues and is currently the only method to solve this problem.

Apart from cosmology, the Abundance Tomography method delivers important implications on the explosion models and the nucleosynthesis in SNe Ia. With the knowledge of the abundance distribution in a larger sample of objects we can constrain and prove these models.

The Abundance Tomography has great impact on progenitor models. The evidence for hydrogen at high velocities revealed by means of spectral synthesis calculations using stratified abundances gives a very strong hint to the correctness of the single-degenerate scenario. Since it was also necessary in our analysis to increase the densities in the outer regions of the SN envelope in order to reproduce the high-velocity components, we conclude that the hydrogen cannot be primordial. Instead, it is most likely inherent in the accreted material from the companion of the white dwarf.

In order to understand the complete process of spectra formation in SNe Ia, the observations and therefore spectral synthesis have to cover the entire wavelength range that is accessible with our instruments. The UV part plays a very important role because most of the flux is emitted in this wavelength region and is then transferred to the red mostly through line blocking. The spectral analysis of the HST observations of SN 2001eh and SN 2001ep proves the ability of our MC code to treat UV spectra very well.

However, there are still shortcomings. Even with the improved MC method, we are still far from a fully realistic treatment of the radiation transfer mechanism in SNe ejecta. Although the Schuster-Schwarzschild approximation is well justified during the first few weeks after the explosion, it is not correct to assume that all radiation is emitted at a sharply defined photosphere. In particular, the need for the modification of the incident radiation field as described above shows that the pseudo photospheric radius is strongly wavelength dependent. Therefore, it will be necessary to implement the deposition of the energy provided by the radioactive decay of ^{56}Ni and ^{56}Co .

The modified nebular approximation used to calculate level populations and the radiation field in the SN envelope is very advanced and produces realistic

results, but it cannot compete with a full NLTE treatment of the radiation transport. On the other hand, NLTE codes will be very time consuming also in the near future so that the MC method keeps the unique feature that it is capable of calculating synthetic spectra almost online.

9.2. Future prospects

One of the major objectives for the coming future is to extend the Abundance Tomography to a larger sample of objects. Thus it will really be possible to make statements about the cause of the diversity of SNe Ia and to constrain further explosion and nucleosynthesis models. The observational campaign of the ESC is perfectly well suited for this purpose. Several objects have already been followed up with both photometric and spectroscopic observations. Notably, most of the ESC SNe Ia were caught very early and provide us with an extensive set of spectra normally covering all phases of the evolution. Especially SN 2003du is worth mentioning. It is one of the best observed SNe Ia ever. So far the ESC observations covered only optical and infrared wavelengths. Therefore, the upcoming UV spectra from the HST, provide us with a perfect data base for the Abundance Tomography analyses.

Another urgent issue that needs addressing is the treatment of the energy input to the SN ejecta. A solution for this shortcoming of the actual version of the MC code is currently being developed (Hultzs, priv. comm.) and will be available in the near future to be implemented in our MC procedure. Finally, multi-dimensional effects in SNe Ia become more and more relevant for spectral analysis, since several explosion models are meanwhile calculated in three dimensions. Our goal is therefore to extend the MC procedure to 3-D in order to study geometrical effects on spectra formation.

Bibliography

- Abbott, D. C., Lucy, L. B. (1985): Multiline transfer and the dynamics of stellar winds, *ApJ* **288**, 679–693
- Aldering, G., Adam, G., Antilogus, P., Astier, P., Bacon, R., Bongard, S., Bonnaud, C., Copin, Y., Hardin, D., Henault, F., Howell, D. A., Lemonnier, J., Levy, J., Loken, S. C., Nugent, P. E., Pain, R., Pecontal, A., Pecontal, E., Perlmutter, S., Quimby, R. M., Schahmanche, K., Smadja, G., Wood-Vasey, W. M. (2002): Overview of the Nearby Supernova Factory, in *Survey and Other Telescope Technologies and Discoveries*. Edited by Tyson, J. Anthony; Wolff, Sidney. *Proceedings of the SPIE, Volume 4836*, pp. 61-72 (2002)., pp. 61–72
- Anupama, G. C., Sahu, D. K., Jose, J. (2005): Type Ia supernova SN 2003du: Optical observations, *A&A* **429**, 667–676
- Arnett, D. (1996): *Supernovae and nucleosynthesis. An investigation of the history of matter, from the Big Bang to the present*, Princeton series in astrophysics, Princeton, NJ: Princeton University Press
- Arnett, D. W. (1969): A possible model of Supernovae: Detonation of ^{12}C , *Ap&SS* **5**, 180–212
- Arnett, W. D. (1982): Type I Supernovae. I - Analytic solutions for the early part of the light curve, *ApJ* **253**, 785–797
- Axelrod, T. S. (1980): Late time optical spectra from the Ni-56 model for Type I Supernovae, *Ph.D. Thesis*
- Baade, W., Zwicky, F. (1934): Remarks on super-novae and cosmic rays, *Physical Review* **46**, 76–77
- Benetti, S., Mazzali, P. A., et al. (2004a): On the diversity of Type Ia Supernovae. In preparation
- Benetti, S., Meikle, P., Stehle, M., Altavilla, G., Desidera, S., Folatelli, G., Goobar, A., Mattila, S., Mendez, J., Navasardyan, H., Pastorello, A., Patat, F., Riello, M., Ruiz-Lapuente, P., Tsvetkov, D., Turatto, M., Mazzali, P., Hillebrandt, W. (2004b): Supernova 2002bo: inadequacy of the single parameter description, *MNRAS* **348**, 261–278

- Benz, W. (1997): Three-dimensional simulations of core ignition in sub-Chandrasekhar mass models, in *NATO ASIC Proc. 486: Thermonuclear Supernovae*, pp. 457–474
- Benz, W., Cameron, A. G. W., Press, W. H., Bowers, R. L. (1990): Dynamic mass exchange in doubly degenerate binaries. I - 0.9 and 1.2 solar mass stars, *ApJ* **348**, 647–667
- Brahe, T. (1573): *De nova et nullius aevi memoria prius visa stella, iam pridem anno a NATO Christo 1572, mense Novembri primum conspecta, contemplatio mathematica. Hafniae, Laurentius, 1573.*, Kopenhagen
- Branch, D., Baron, E. A., Jeffery, D. J. (2003a): Optical spectra of Supernovae, *Lecture Notes in Physics, Berlin Springer Verlag* **598**, 47–75
- Branch, D., Fisher, A., Nugent, P. (1993): On the relative frequencies of spectroscopically normal and peculiar Type Ia Supernovae, *AJ* **106**, 2383–2391
- Branch, D., Garnavich, P., Matheson, T., Baron, E., Thomas, R. C., Hatano, K., Challis, P., Jha, S., Kirshner, R. P. (2003b): Optical spectra of the Type Ia Supernova 1998aq, *AJ* **126**, 1489–1498
- Branch, D., Livio, M., Yungelson, L. R., Boffi, F. R., Baron, E. (1995): In search of the progenitors of Type Ia Supernovae, *PASP* **107**, 1019–1029
- Branch, D., Thomas, R. C., Baron, E., Kasen, D., Hatano, K., Nomoto, K., Filippenko, A. V., Li, W., Rudy, R. J. (2004): Direct analysis of spectra of the peculiar Type Ia Supernova 2000cx, *ApJ* **606**, 413–423
- Burkert, A., Ruiz-Lapuente, P. (1997): Dormant dwarf spheroidal galaxies, deactivated by Type Ia Supernovae, *ApJ* **480**, 297–302
- Cacella, P., Hirose, Y., Nakano, S., Kushida, Y., Kushida, R., Li, W. D. (2002): Supernova 2002bo in NGC 3190, *IAU Circ.* **7847**, 1
- Cappellaro, E., Evans, R., Turatto, M. (1999): A new determination of Supernova rates and a comparison with indicators for galactic star formation, *A&A* **351**, 459–466
- Cappellaro, E., Mazzali, P. A., Benetti, S., Danziger, I. J., Turatto, M., della Valle, M., Patat, F. (1997): SN Ia light curves and radioactive decay, *A&A* **328**, 203–210
- Cappellaro, E., Turatto, M. (2001): Supernova types and rates, in *ASSL Vol. 264: The Influence of Binaries on Stellar Population Studies*, pp. 199–214

- Castor, J. I. (1970): Spectral line formation in Wolf-rayet envelopes., *MNRAS* **149**, 111–127
- Chiappini, C., Romano, D., Matteucci, F. (2003): Oxygen, carbon and nitrogen evolution in galaxies, *MNRAS* **339**, 63–81
- Colgate, S. A., McKee, C. (1969): Early Supernova luminosity, *ApJ* **157**, 623–643
- Contardo, G., Leibundgut, B., Vacca, W. D. (2000): Epochs of maximum light and bolometric light curves of Type Ia Supernovae, *A&A* **359**, 876–886
- Deng, J., Kawabata, K. S., Ohya, Y., Nomoto, K., Mazzali, P. A., Wang, L., Jeffery, D. J., Iye, M., Tomita, H., Yoshii, Y. (2004): Subaru spectroscopy of the interacting Type Ia Supernova SN 2002ic: Evidence of a hydrogen-rich, asymmetric circumstellar medium, *ApJ* **605**, L37–L40
- Eastman, R. G., Pinto, P. A. (1993): Spectrum formation in Supernovae - numerical techniques, *ApJ* **412**, 731–751
- Elias, J. H., Frogel, J. A., Hackwell, J. A., Persson, S. E. (1981): Infrared light curves of Type I Supernovae, *ApJ* **251**, L13–L16
- Ferrara, A., Tolstoy, E. (2000): The role of stellar feedback and dark matter in the evolution of dwarf galaxies, *MNRAS* **313**, 291–309
- Filippenko, A. V. (1997): Optical spectra of Supernovae, *ARA&A* **35**, 309–355
- Filippenko, A. V., Richmond, M. W., Branch, D., Gaskell, M., Herbst, W., Ford, C. H., Treffers, R. R., Matheson, T., Ho, L. C., Dey, A., Sargent, W. L. W., Small, T. A., van Breugel, W. J. M. (1992): The subluminescent, spectroscopically peculiar Type Ia SN 1991bg in the elliptical galaxy NGC 4374, *AJ* **104**, 1543–1556
- Fisher, A., Branch, D., Nugent, P., Baron, E. (1997): Evidence for a High-velocity Carbon-rich Layer in the Type IA SN 1990N, *ApJ* **481**, L89–L92
- Fisher, A. K. (2000): Direct analysis of Type Ia Supernovae spectra, *Ph.D. Thesis*
- Gómez, G., López, R. (1998): The Canarias Type Ia Supernova archive. II. A standard spectral evolution sequence, *AJ* **115**, 1096–1102
- Gamezo, V. N., Khokhlov, A. M., Oran, E. S. (2004): Deflagrations and detonations in thermonuclear Supernovae, *Physical Review Letters* **92**(21), 211102–1–4
- Gamezo, V. N., Khokhlov, A. M., Oran, E. S., Chtchelkanova, A. Y., Rosenberg, R. O. (2003): Thermonuclear Supernovae: Simulations of the deflagration stage and their implications, *Science* **299**, 77–81

- Ganeshalingam, M., Li, W. D., Chornock, R., Filippenko, A. V. (2001): Supernova 2001eh in UGC 1162, *IAU Circ.* **7714**, 4
- Garnavich, P. M. (1995): Infrared spectra of Supernovae, *Bulletin of the American Astronomical Society* **27**, 864p
- Gerardy, C. L., Höflich, P., Fesen, R. A., Marion, G. H., Nomoto, K., Quimby, R., Schaefer, B. E., Wang, L., Wheeler, J. C. (2004): SN 2003du: Signatures of the circumstellar environment in a normal Type Ia Supernova?, *ApJ* **607**, 391–405
- Green, D. A., Stephenson, F. R. (2003): Historical Supernovae, *Lecture Notes in Physics, Berlin Springer Verlag* **598**, 7–19
- Hachisu, I., Kato, M., Nomoto, K. (1999a): A wide symbiotic channel to Type Ia Supernovae, *ApJ* **522**, 487–503
- Hachisu, I., Kato, M., Nomoto, K., Umeda, H. (1999b): A new evolutionary path to Type Ia Supernovae: A Helium-rich supersoft X-ray source channel, *ApJ* **519**, 314–323
- Hamuy, M., Maza, J., Pinto, P. A., Phillips, M. M., Suntzeff, N. B., Blum, R. D., Olsen, K. A. G., Pinfield, D. J., Ivanov, V. D., Augusteijn, T., Brilliant, S., Chadid, M., Cuby, J.-G., Doublier, V., Hainaut, O. R., Le Floc'h, E., Lidman, C., Petr-Gotzens, M. G., Pompei, E., Vanzi, L. (2002): Optical and infrared spectroscopy of SN 1999ee and SN 1999ex, *AJ* **124**, 417–429
- Hamuy, M., Phillips, M. M., Suntzeff, N. B., Maza, J., González, L. E., Roth, M., Krisciunas, K., Morrell, N., Green, E. M., Persson, S. E., McCarthy, P. J. (2003): An asymptotic-giant-branch star in the progenitor system of a Type Ia Supernova, *Nature* **424**, 651–654
- Hamuy, M., Phillips, M. M., Suntzeff, N. B., Schommer, R. A., Maza, J., Antezan, A. R., Wischnjewsky, M., Valladares, G., Muenza, C., Gonzales, L. E., Aviles, R., Wells, L. A., Smith, R. C., Navarrete, M., Covarrubias, R., Williger, G. M., Walker, A. R., Layden, A. C., Elias, J. H., Baldwin, J. A., Hernandez, M., Tirado, H., Ugarte, P., Elston, R., Saavedra, N., Barrientos, F., Costa, E., Lira, P., Ruiz, M. T., Anguita, C., Gomez, X., Ortiz, P., della Valle, M., Danziger, J., Storm, J., Kim, Y.-C., Bailyn, C., Rubenstein, E. P., Tucker, D., Cersosimo, S., Mendez, R. A., Siciliano, L., Sherry, W., Chaboyer, B., Koopmann, R. A., Geisler, D., Sarajedini, A., Dey, A., Tyson, N., Rich, R. M., Gal, R., Lamontagne, R., Caldwell, N., Guhathakurta, P., Phillips, A. C., Szkody, P., Prosser, C., Ho, L. C., McMahan, R., Baggley, G., Cheng, K.-P., Havlen, R., Wakamatsu, K., Janes, K., Malkan, M., Baganoff, F., Seitzer, P., Shara, M., Sturch, C., Hesser, J., Hartig, A. N. P., Hughes, J., Welch, D., Williams, T. B., Ferguson, H., Francis,

- P. J., French, L., Bolte, M., Roth, J., Odewahn, S., Howell, S., Krzeminski, W. (1996): BVRI light curves for 29 Type Ia Supernovae, *AJ* **112**, 2408–2437
- Han, Z., Podsiadlowski, P. (2004): The single-degenerate channel for the progenitors of Type Ia Supernovae, *MNRAS* **350**, 1301–1309
- Hashimoto, M.-A., Hanawa, T., Sugimoto, D. (1983): Explosive helium burning at constant pressures, *PASJ* **35**, 1–15
- Hatano, K., Branch, D., Fisher, A., Baron, E., Filippenko, A. V. (1999): On the high-velocity ejecta of the Type Ia Supernova SN 1994D, *ApJ* **525**, 881–885
- Hauschildt, P. H., Baron, E. (1999): Numerical solution of the expanding stellar atmosphere problem, *J. Comp. Appl. Math.* **109**, 41–63
- Hernandez, M., Meikle, W. P. S., Aparicio, A., Benn, C. R., Burleigh, M. R., Chrysostomou, A. C., Fernandes, A. J. L., Geballe, T. R., Hammersley, P. L., Iglesias-Paramo, J., James, D. J., James, P. A., Kemp, S. N., Lister, T. A., Martinez-Delgado, D., Oscoz, A., Pollacco, D. L., Rozas, M., Smartt, S. J., Sorensen, P., Swaters, R. A., Telting, J. H., Vacca, W. D., Walton, N. A., Zapatero-Osorio, M. R. (2000): An early-time infrared and optical study of the Type Ia Supernova 1998bu in M96, *MNRAS* **319**, 223–234
- Hillebrandt, W., Niemeyer, J. C. (2000): Type Ia Supernova explosion models, *ARA&A* **38**, 191–230
- Höflich, P. (1995): Analysis of the Type Ia Supernova SN 1994D, *ApJ* **443**, 89–108
- Höflich, P., Gerardy, C., Linder, E., et al. (2003): Models for Type Ia Supernovae and cosmology, *Lecture Notes in Physics, Berlin Springer Verlag* **635**, 203–227
- Höflich, P., Khokhlov, A. (1996): Explosion models for Type Ia Supernovae: A comparison with observed light curves, distances, H_0 , and q_0 , *ApJ* **457**, 500–528
- Höflich, P., Khokhlov, A. M., Wheeler, J. C. (1995): Delayed detonation models for normal and subluminous Type Ia Supernovae: Absolute brightness, light curves, and molecule formation, *ApJ* **444**, 831–847
- Hoyle, F., Fowler, W. A. (1960): Nucleosynthesis in Supernovae., *ApJ* **132**, 565–590
- Hutchings, D., Li, W. D. (2001): SN 2001ep in NGC 1699, *IAU Circ.* **7727**, 1
- Hutchings, D., Li, W. D. (2002): SN 2002dj in NGC 5018, *IAU Circ.* **7918**, 1
- Iben, I., Tutukov, A. V. (1984): Supernovae of Type I as end products of the evolution of binaries with components of moderate initial mass (M not greater than about 9 solar masses), *ApJS* **54**, 335–372

- Iben, I. J., Tutukov, A. V. (1994): Helium-accreting degenerate dwarfs as preSupernovae and scenarios for the ultrasoft x-ray sources, *ApJ* **431**, 264–272
- Iben, I. J., Tutukov, A. V. (1999): On the evolution of close triple stars that produce Type Ia Supernovae, *ApJ* **511**, 324–334
- Iwamoto, K., Brachwitz, F., Nomoto, K., Kishimoto, N., Umeda, H., Hix, W. R., Thielemann, F. (1999): Nucleosynthesis in Chandrasekhar mass models for Type Ia Supernovae and constraints on progenitor systems and burning-front propagation, *ApJS* **125**, 439–462
- Kasen, D. (2004): Aspherical Supernovae, *Ph.D. Thesis*
- Kasen, D., Nugent, P., Thomas, R. C., Wang, L. (2004): Could there be a hole in Type Ia Supernovae?, *ApJ* **610**, 876–887
- Kasen, D., Nugent, P., Wang, L., Howell, D. A., Wheeler, J. C., Höflich, P., Baade, D., Baron, E., Hauschildt, P. H. (2003): Analysis of the flux and polarization spectra of the Type Ia Supernova SN 2001el: Exploring the geometry of the high-velocity ejecta, *ApJ* **593**, 788–808
- Khokhlov, A. (1994): Supernovae deflagrations in three dimensions, *ApJ* **424**, L115–L117
- Khokhlov, A. M. (1991): Delayed detonation model for Type Ia Supernovae, *A&A* **245**, 114–128
- Khokhlov, A. M. (1995): Propagation of turbulent flames in Supernovae, *ApJ* **449**, 695–713
- Kirshner, R. P., Jeffery, D. J., Leibundgut, B., Challis, P. M., Sonneborn, G., Phillips, M. M., Suntzeff, N. B., Smith, R. C., Winkler, P. F., Winge, C., Hamuy, M., Hunter, D. A., Roth, K. C., Blades, J. C., Branch, D., Chevalier, R. A., Fransson, C., Panagia, N., Wagoner, R. V., Wheeler, J. C., Harkness, R. P. (1993): SN 1992A: Ultraviolet and optical studies based on HST, IUE, and CTIO observations, *ApJ* **415**, 589–615
- Klein, R. I., Castor, J. I. (1978): H and He II spectra of Of stars, *ApJ* **220**, 902–923
- Kotak, R., Meikle, W. P. S., Adamson, A., Leggett, S. K. (2004): On the nature of the circumstellar medium of the remarkable Type Ia/II_n supernova SN 2002ic, *MNRAS* **354**, L13–L17
- Kotak, R., Meikle, W. P. S., Rodriguez-Gil, P. (2003): Supernova 2003du in UGC 9391, *IAU Circ.* **8122**, 3

- Kurucz, R., Bell, B. (1995): Atomic Line Data, *Atomic line data (R.L. Kurucz and B. Bell) Kurucz CD-ROM No. 23. Cambridge, Mass.: Smithsonian Astrophysical Observatory, 1995.* **23**
- Leibundgut, B. (2000): Type Ia Supernovae, *A&A Rev.* **10**, 179–209
- Leibundgut, B. (2001): Cosmological implications from observations of Type Ia Supernovae, *ARA&A* **39**, 67–98
- Lentz, E. J., Baron, E., Branch, D., Hauschildt, P. H., Nugent, P. E. (2000): Metallicity effects in non-LTE model atmospheres of Type Ia Supernovae, *ApJ* **530**, 966–976
- Li, W., Filippenko, A. V., Chornock, R., Berger, E., Berlind, P., Calkins, M. L., Challis, P., Fassnacht, C., Jha, S., Kirshner, R. P., Matheson, T., Sargent, W. L. W., Simcoe, R. A., Smith, G. H., Squires, G. (2003): SN 2002cx: The most peculiar known Type Ia Supernova, *PASP* **115**, 453–473
- Li, W., Filippenko, A. V., Gates, E., Chornock, R., Gal-Yam, A., Ofek, E. O., Leonard, D. C., Modjaz, M., Rich, R. M., Riess, A. G., Treffers, R. R. (2001): The unique Type Ia Supernova 2000cx in NGC 524, *PASP* **113**, 1178–1204
- Li, W. D., Filippenko, A. V., Riess, A. G., Treffers, R. R., Hu, J. Y., Qiu, Y. L. (2000): A high peculiarity rate for Type Ia SNe, in *American Institute of Physics Conference Series*, pp. 91–94
- Livio, M. (2000): The progenitors of Type Ia Supernovae, in *Type Ia Supernovae, Theory and Cosmology. Edited by J. C. Niemeyer and J. W. Truran. Published by Cambridge University Press, 2000*, pp. 33–48
- Livne, E. (1993): Numerical simulations of the convective flame in white dwarfs, *ApJ* **406**, L17–L20
- Lucy, L. B. (1971): The formation of resonance lines in extended and expanding atmospheres, *ApJ* **163**, 95–110
- Lucy, L. B. (1991): Nonthermal excitation of helium in Type Ib Supernovae, *ApJ* **383**, 308–313
- Lucy, L. B. (1999a): Computing radiative equilibria with Monte Carlo techniques, *A&A* **344**, 282–288
- Lucy, L. B. (1999b): Improved Monte Carlo techniques for the spectral synthesis of Supernovae, *A&A* **345**, 211–220
- Lundmark, K. (1920): *Svenska Vetenskapsakad. Handl* **60**, 8

- Marion, G. H., Höflich, P., Vacca, W. D., Wheeler, J. C. (2003): Near-infrared spectra of Type Ia Supernovae, *ApJ* **591**, 316–333
- Matheson, T., Jha, S., Challis, P., Kirshner, R., Huchra, J. (2001): Supernova 2001ep in NGC 1699, *IAU Circ.* **7731**, 3
- Mazzali, P. A. (2000): Applications of an improved Monte Carlo code to the synthesis of early-time Supernova spectra, *A&A* **363**, 705–716
- Mazzali, P. A. (2001): On the presence of silicon and carbon in the pre-maximum spectrum of the Type Ia SN 1990N, *MNRAS* **321**, 341–346
- Mazzali, P. A., Benetti, S., Stehle, M., Branch, D., Deng, J., Maeda, K., Nomoto, K., Hamuy, M. (2005): High-velocity features in the spectra of the Type Ia supernova SN 1999ee: a property of the explosion or evidence of circumstellar interaction?, *MNRAS* **357**, 200–206
- Mazzali, P. A., Danziger, I. J., Turatto, M. (1995): A study of the properties of the peculiar SN Ia 1991T through models of its evolving early-time spectrum., *A&A* **297**, 509–534
- Mazzali, P. A., Lucy, L. B. (1993): The application of Monte Carlo methods to the synthesis of early-time Supernovae spectra, *A&A* **279**, 447–456
- Mazzali, P. A., Lucy, L. B., Butler, K. (1992): Barium and other s-process elements in the early-time spectrum of SN 1987A, *A&A* **258**, 399–411
- Mazzali, P. A., Lucy, L. B., Danziger, I. J., Gouiffes, C., Cappellaro, E., Turatto, M. (1993): Models for the early-time spectral evolution of the 'standard' Type Ia Supernova 1990N, *A&A* **269**, 423–445
- Mazzali, P. A., Nomoto, K., Cappellaro, E., Nakamura, T., Umeda, H., Iwamoto, K. (2001a): Can differences in the nickel abundance in Chandrasekhar-mass models explain the relation between the brightness and decline rate of normal Type Ia Supernovae?, *ApJ* **547**, 988–994
- Mazzali, P. A., Nomoto, K., Patat, F., Maeda, K. (2001b): The nebular spectra of the Hypernova SN 1998bw and evidence for asymmetry, *ApJ* **559**, 1047–1053
- Meikle, W. P. S. (2000): The absolute infrared magnitudes of Type Ia Supernovae, *MNRAS* **314**, 782–792
- Mihalas, D. (1978): *Stellar atmospheres /2nd edition/*, San Francisco, W. H. Freeman and Co., 1978. 650 p.
- Minkowski, R. (1941): Spectra of Supernovae, *PASP* **53**, 224–225

- Mochkovitch, R., Guerrero, J., Segretain, L. (1997): The merging of white dwarfs, in *NATO ASIC Proc. 486: Thermonuclear Supernovae*, pp. 187–204
- Niemeyer, J. C., Bushe, W. K., Ruetsch, G. R. (1999): Small-scale interaction of turbulence with thermonuclear flames in Type Ia Supernovae, *ApJ* **524**, 290–294
- Niemeyer, J. C., Hillebrandt, W. (1995a): Microscopic instabilities of nuclear flames in Type Ia Supernovae, *ApJ* **452**, 779–784
- Niemeyer, J. C., Hillebrandt, W. (1995b): Turbulent nuclear flames in Type Ia Supernovae, *ApJ* **452**, 769–778
- Nomoto, K. (1982a): Accreting white dwarf models for Type I Supernovae. I - Presupernova evolution and triggering mechanisms, *ApJ* **253**, 798–810
- Nomoto, K. (1982b): Accreting white dwarf models for Type I Supernovae. II - Off-center detonation Supernovae, *ApJ* **257**, 780–792
- Nomoto, K., Iben, I. (1985): Carbon ignition in a rapidly accreting degenerate dwarf - A clue to the nature of the merging process in close binaries, *ApJ* **297**, 531–537
- Nomoto, K., Iwamoto, K., Suzuki, T. (1995): The evolution and explosion of massive binary stars and Type Ib-Ic-IIb-III Supernovae, *Phys. Rep.* **256**, 173–191
- Nomoto, K., Kondo, Y. (1991): Conditions for accretion-induced collapse of white dwarfs, *ApJ* **367**, L19–L22
- Nomoto, K., Sugimoto, D. (1977): Rejuvenation of helium white dwarfs by mass accretion, *PASJ* **29**, 765–780
- Nomoto, K., Sugimoto, D., Neo, S. (1976): Carbon deflagration supernova, an alternative to carbon detonation, *Ap&SS* **39**, L37–L42
- Nomoto, K., Thielemann, F.-K., Yokoi, K. (1984): Accreting white dwarf models of Type I Supernovae. III - Carbon deflagration Supernovae, *ApJ* **286**, 644–658
- Nomoto, K., Uenishi, T., Kobayashi, C., Umeda, H., Ohkubo, T., Hachisu, I., Kato, M. (2003): Type Ia Supernovae: Progenitors and diversities, in *From Twilight to Highlight: The Physics of Supernovae*, pp. 115–127
- Nomoto, K., Umeda, H., Hachisu, I., Kato, M., Kobayashi, C., Tsujimoto, T. (2000): Type Ia Supernova progenitors, environmental effects, and cosmic Supernova rates, in *Type Ia Supernovae, Theory and Cosmology. Edited by J. C. Niemeyer and J. W. Truran. Published by Cambridge University Press, 2000*, pp. 63–88, astro-ph/9907386

- Nugent, P., Baron, E., Branch, D., Fisher, A., Hauschildt, P. H. (1997): Synthetic spectra of hydrodynamic models of Type Ia Supernovae, *ApJ* **485**, 812–819
- Nugent, P., Baron, E., Hauschildt, P. H., Branch, D. (1995a): Spectrum synthesis of the Type Ia Supernovae SN 1992A and SN 1981B, *ApJ* **441**, L33–L36
- Nugent, P., Phillips, M., Baron, E., Branch, D., Hauschildt, P. (1995b): Evidence for a spectroscopic sequence among Type Ia Supernovae, *ApJ* **455**, 147–150
- Pain, R., Hook, I. M., Deustua, S., Gabi, S., Goldhaber, G., Groom, D., Kim, A. G., Kim, M. Y., Lee, J. C., Pennypacker, C. R., Perlmutter, S., Small, I. A., Goobar, A., Ellis, R. S., McMahon, R. G., Glazebrook, K., Boyle, B. J., Bunclark, P. S., Carter, D., Irwin, M. J. (1996): The Type Ia Supernova rate at z approximately 0.4, *ApJ* **473**, 356–364
- Patat, F., Barbon, R., Cappellaro, E., Turatto, M. (1994): Light curves of Type II Supernovae. 2: The analysis, *A&A* **282**, 731–741
- Patat, F., Benetti, S., Cappellaro, E., Danziger, I. J., della Valle, M., Mazzali, P. A., Turatto, M. (1996): The Type Ia Supernova 1994D in NGC 4526: the early phases, *MNRAS* **278**, 111–124
- Pauldrach, A. W. A., Duschinger, M., Mazzali, P. A., Puls, J., Lennon, M., Miller, D. L. (1996): NLTE models for synthetic spectra of Type Ia Supernovae. The influence of line blocking., *A&A* **312**, 525–538
- Pauldrach, A. W. A., Hoffmann, T. L., Lennon, M. (2001): Radiation-driven winds of hot luminous stars. XIII. A description of NLTE line blocking and blanketing towards realistic models for expanding atmospheres, *A&A* **375**, 161–195
- Percival, W. J., Sutherland, W., Peacock, J. A., Baugh, C. M., Bland-Hawthorn, J., Bridges, T., Cannon, R., Cole, S., Colless, M., Collins, C., Couch, W., Dalton, G., De Propris, R., Driver, S. P., Efstathiou, G., Ellis, R. S., Frenk, C. S., Glazebrook, K., Jackson, C., Lahav, O., Lewis, I., Lumsden, S., Maddox, S., Moody, S., Norberg, P., Peterson, B. A., Taylor, K. (2002): Parameter constraints for flat cosmologies from cosmic microwave background and 2dFGRS power spectra, *MNRAS* **337**, 1068–1080
- Perlmutter, S., Aldering, G., Goldhaber, G., Knop, R. A., Nugent, P., Castro, P. G., Deustua, S., Fabbro, S., Goobar, A., Groom, D. E., Hook, I. M., Kim, A. G., Kim, M. Y., Lee, J. C., Nunes, N. J., Pain, R., Pennypacker, C. R., Quimby, R., Lidman, C., Ellis, R. S., Irwin, M., McMahon, R. G., Ruiz-Lapuente, P., Walton, N., Schaefer, B., Boyle, B. J., Filippenko, A. V., Matheson, T., Fruchter, A. S., Panagia, N., Newberg, H. J. M., Couch, W. J., The Supernova Cosmology

- Project (1999): Measurements of Ω and Λ from 42 high-redshift Supernovae, *ApJ* **517**, 565–586
- Phillips, M. M. (1993): The absolute magnitudes of Type Ia Supernovae, *ApJ* **413**, L105–L108
- Phillips, M. M., Lira, P., Suntzeff, N. B., Schommer, R. A., Hamuy, M., Maza, J. (1999): The reddening-free decline rate versus luminosity relationship for Type Ia Supernovae, *AJ* **118**, 1766–1776
- Pignata, G., Patat, F., Benetti, S., Blinnikov, S., Hillebrandt, W., Kotak, R., Leibundgut, B., Mazzali, P. A., Meikle, P., Qiu, Y., Ruiz-Lapuente, P., Smartt, S. J., Sorokina, E., Stritzinger, M., Stehle, M., Turatto, M., Marsh, T., Martin-Luis, F., McBride, N., Mendez, J., Morales-Rueda, L., Narbutis, D., Street, R. (2004): Photometric observations of the Type Ia SN 2002er in UGC 10743, *MNRAS* **355**, 178–190
- Pinto, P. A., Eastman, R. G. (2000): The physics of Type Ia Supernova light curves. II. Opacity and diffusion, *ApJ* **530**, 757–776
- Reinecke, M., Hillebrandt, W., Niemeyer, J. C. (1999a): Thermonuclear explosions of Chandrasekhar-mass C+O white dwarfs, *A&A* **347**, 739–747
- Reinecke, M., Hillebrandt, W., Niemeyer, J. C. (2002): Three-dimensional simulations of type Ia Supernovae, *A&A* **391**, 1167–1172
- Reinecke, M., Hillebrandt, W., Niemeyer, J. C., Klein, R., Gröbl, A. (1999b): A new model for deflagration fronts in reactive fluids, *A&A* **347**, 724–733
- Reiss, D. J. (1999): The rate of Supernovae in the nearby and distant universe, *Ph.D. Thesis*
- Renzini, A. (1999): Chemical evolution on the scale of clusters of galaxies, and beyond, in *Chemical Evolution from Zero to High Redshift*, pp. 185–196
- Riello, M., Benetti, S., Altavilla, G., Pastorello, A., Turatto, M., Cappellaro, E., O’Toole, S. (2002): Supernova 2002dj in NGC 5018, *IAU Circ.* **7919**, 2
- Riess, A. G., Filippenko, A. V., Challis, P., Clocchiatti, A., Diercks, A., Garnavich, P. M., Gilliland, R. L., Hogan, C. J., Jha, S., Kirshner, R. P., Leibundgut, B., Phillips, M. M., Reiss, D., Schmidt, B. P., Schommer, R. A., Smith, R. C., Spyromilio, J., Stubbs, C., Suntzeff, N. B., Tonry, J. (1998): Observational evidence from Supernovae for an accelerating Universe and a cosmological constant, *AJ* **116**, 1009–1038

- Riess, A. G., Filippenko, A. V., Li, W., Treffers, R. R., Schmidt, B. P., Qiu, Y., Hu, J., Armstrong, M., Faranda, C., Thouvenot, E., Buil, C. (1999a): The rise time of nearby Type Ia Supernovae, *AJ* **118**, 2675–2688
- Riess, A. G., Kirshner, R. P., Schmidt, B. P., Jha, S., Challis, P., Garnavich, P. M., Esin, A. A., Carpenter, C., Grashius, R., Schild, R. E., Berlind, P. L., Huchra, J. P., Prosser, C. F., Falco, E. E., Benson, P. J., Briceño, C., Brown, W. R., Caldwell, N., dell'Antonio, I. P., Filippenko, A. V., Goodman, A. A., Grogin, N. A., Groner, T., Hughes, J. P., Green, P. J., Jansen, R. A., Kleyna, J. T., Luu, J. X., Macri, L. M., McLeod, B. A., McLeod, K. K., McNamara, B. R., McLean, B., Milone, A. A. E., Mohr, J. J., Moraru, D., Peng, C., Peters, J., Prestwich, A. H., Stanek, K. Z., Szentgyorgyi, A., Zhao, P. (1999b): BVRI light curves for 22 Type Ia Supernovae, *AJ* **117**, 707–724
- Riess, A. G., Strolger, L., Tonry, J., Casertano, S., Ferguson, H. C., Mobasher, B., Challis, P., Filippenko, A. V., Jha, S., Li, W., Chornock, R., Kirshner, R. P., Leibundgut, B., Dickinson, M., Livio, M., Giavalisco, M., Steidel, C. C., Benítez, T., Tsvetanov, Z. (2004): Type Ia Supernova Discoveries at $z > 1$ from the Hubble Space Telescope: Evidence for Past Deceleration and Constraints on Dark Energy Evolution, *ApJ* **607**, 665–687
- Röpke, F. K., Hillebrandt, W. (2004a): Full-star Type Ia Supernova explosion models. Submitted to *A&A*, astro-ph/0409286
- Röpke, F. K., Hillebrandt, W. (2004b): The case against the progenitor's carbon-to-oxygen ratio as a source of peak luminosity variations in Type Ia Supernovae, *A&A* **420**, L1–L4
- Ruiz-Lapuente, P., Canal, R. (1998): Type Ia Supernova counts at High- z : Signatures of cosmological models and progenitors, *ApJ* **497**, 57–60
- Ruiz-Lapuente, P., Comeron, F., Méndez, J., Canal, R., Smartt, S. J., Filippenko, A. V., Kurucz, R. L., Chornock, R., Foley, R. J., Stanishev, V., Ibata, R. (2004): The binary progenitor of Tycho Brahe's 1572 Supernova, *Nature* **431**, 1069–1072
- Saio, H., Nomoto, K. (1985): Evolution of a merging pair of C + O white dwarfs to form a single neutron star, *A&A* **150**, L21–L23
- Saio, H., Nomoto, K. (1998): Inward propagation of nuclear-burning shells in merging C-O and He white dwarfs, *ApJ* **500**, 388–397
- Schmitz, M. F., Gaskel, C. M. (1988): A comparison of the SN 1987A light curve with other Type II Supernovae and the detectability of similar Supernovae, in *Supernova 1987A in the Large Magellanic Cloud*, pp. 112–115

- Schwartz, M., Holvorcem, P. R. (2003): Supernova 2003du in UGC 9391, IAU Circ. **8121**, 1
- Smartt, S. J., Patat, F., Meikle, P., Araujo, S. (2002): Supernova 2002er in UGC 10743, IAU Circ. **7961**, 2
- Spergel, D. N., Verde, L., Peiris, H. V., Komatsu, E., Nolta, M. R., Bennett, C. L., Halpern, M., Hinshaw, G., Jarosik, N., Kogut, A., Limon, M., Meyer, S. S., Page, L., Tucker, G. S., Weiland, J. L., Wollack, E., Wright, E. L. (2003): First-Year Wilkinson Microwave Anisotropy Probe (WMAP) Observations: Determination of Cosmological Parameters, *ApJS* **148**, 175–194
- Spyromilio, J., Meikle, W. P. S., Allen, D. A., Graham, J. R. (1992): A large mass of iron in Supernova 1991T, *MNRAS* **258**, 53–56
- Stehle, M., Mazzali, P. A., Benetti, S., Hillebrandt, W. (2004): Abundance Tomography of Type Ia Supernovae: I. The case of SN 2002bo. Submitted to *MNRAS*, astro-ph/0409342
- Stephenson, F. R., Green, D. A. (2002): *Historical Supernovae and their remnants, by F. Richard Stephenson and David A. Green. International series in astronomy and astrophysics, vol. 5. Oxford: Clarendon Press, 2002, ISBN 0198507666*
- Stritzinger, M., Hamuy, M., Suntzeff, N. B., Smith, R. C., Phillips, M. M., Maza, J., Strolger, L.-G., Antezana, R., González, L., Wischnjewsky, M., Candia, P., Espinoza, J., González, D., Stubbs, C., Becker, A. C., Rubenstein, E. P., Galaz, G. (2002): Optical photometry of the Type Ia Supernova 1999ee and the Type Ib/c Supernova 1999ex in IC 5179, *AJ* **124**, 2100–2117
- Thomas, R. C., Branch, D., Baron, E., Nomoto, K., Li, W., Filippenko, A. V. (2004): On the geometry of the high-velocity ejecta of the peculiar Type Ia Supernova 2000cx, *ApJ* **601**, 1019–1030
- Tonry, J. L., Schmidt, B. P., Barris, B., Candia, P., Challis, P., Clocchiatti, A., Coil, A. L., Filippenko, A. V., Garnavich, P., Hogan, C., Holland, S. T., Jha, S., Kirshner, R. P., Krisciunas, K., Leibundgut, B., Li, W., Matheson, T., Phillips, M. M., Riess, A. G., Schommer, R., Smith, R. C., Sollerman, J., Spyromilio, J., Stubbs, C. W., Suntzeff, N. B. (2003): Cosmological results from High-*z* Supernovae, *ApJ* **594**, 1–24
- Travaglio, C., Hillebrandt, W., Reinecke, M., Thielemann, F.-K. (2004): Nucleosynthesis in multi-dimensional SN Ia explosions, *A&A* **425**, 1029–1040
- Truran, J. W., Arnett, W. D., Cameron, A. G. W. (1967): Nucleosynthesis in Supernova shock waves, *Canadian Journal of Physics* **45**, 2315–2332

- Wang, L., Baade, D., Höflich, P., Khokhlov, A., Wheeler, J. C., Kasen, D., Nugent, P. E., Perlmutter, S., Fransson, C., Lundqvist, P. (2003): Spectropolarimetry of SN 2001el in NGC 1448: Asphericity of a normal Type Ia Supernova, *ApJ* **591**, 1110–1128
- Wang, L., Baade, D., Höflich, P., Wheeler, J. C., Kawabata, K., Nomoto, K. (2004): On the hydrogen emission from the Type Ia Supernova SN 2002ic, *ApJ* **604**, L53–L56
- Webbink, R. F. (1984): Double white dwarfs as progenitors of R Coronae Borealis stars and Type I Supernovae, *ApJ* **277**, 355–360
- Wheeler, J. C., Benetti, S. (2000): *Supernovae*, Allen's astrophysical quantities, 4th edition; edited by Cox, A. N.; New York: AIP Press; Springer. ISBN: 0387987460, chapter 18, pp. 451–469
- Wheeler, J. C., Harkness, R. P. (1990): Type I Supernovae., *Reports of Progress in Physics* **53**, 1467–1557
- Wheeler, J. C., Piran, T., Weinberg, S. (Eds.) (1990): *Jerusalem Winter School for Theoretical Physics. Supernovae. Volume 6, Jerusalem, Dec. 28, 1988- Jan. 5, 1989.*
- Whelan, J., Iben, I. J. (1973): Binaries and Supernovae of Type I, *ApJ* **186**, 1007–1014
- Wiese, W. L., Fuhr, J. R., Deters, T. M. (1996): *Atomic transition probabilities of carbon, nitrogen, and oxygen : A critical data compilation*, Washington, DC: American Chemical Society for the National Institute of Standards and Technology (NIST)
- Wilson, O. C. (1939): Possible applications of Supernovae to the study of the nebular redshifts., *ApJ* **90**, 634–636
- Wood-Vasey, W. M., Li, W. D., Swift, B., Ganeshalingam, M. (2002): Supernovae 2002ep, 2002eq, 2002er, 2002es, 2002et, *IAU Circ.* **7959**, 1
- Woosley, S. E., Axelrod, T. S., Weaver, T. A. (1984): Nucleosynthesis in stellar explosions, in *ASSL Vol. 109: Stellar Nucleosynthesis*, pp. 263–296
- Woosley, S. E., Weaver, T. A. (1994): Massive stars, supernovae, and nucleosynthesis, in *Les Houches Session LIV: Supernovae*, edited by J. Audouze, S. Bludman, R. Mochovitch, J. Zinn-Justin, Elsevier, Amsterdam, pp. 63–154
- Young, T. R., Branch, D. (1989): Absolute light curves of Type II Supernovae, *ApJ* **342**, L79–L82

Zwicky, F. (1939): On the theory and observation of highly collapsed stars, *Physical Review* **55**, 726–743

Zwicky, F. (1965): *Supernovae*, Stellar Structure - Stars and Stellar Systems: Compendium of Astronomy and Astrophysics, Vol. VIII, edited by Lawrence H. Aller and Dean B. McLaughlin. University of Chicago Press, pp. 367–424

Danksagung

An dieser Stelle möchte ich mich bei Paolo Mazzali herzlichst bedanken. Er hat zur Bearbeitung des Themas angeregt und durch seine stetige Unterstützung die vorliegende Arbeit ermöglicht. Durch seine Freude und seinen Enthusiasmus an der Astrophysik hat er auch mich für dieses Fachgebiet begeistert. Über die Wissenschaft hinaus ist er in den drei Jahren mehr als ein Betreuer für mich geworden.

Mein besonderer Dank gilt Wolfgang Hillebrandt, der durch seine Förderung und fachliche Hilfe erheblich zum Gelingen dieser Arbeit beigetragen hat.

Die Betreuung durch Adi Pauldrach beschränkte sich nicht nur auf wissenschaftliche Diskussionen, sondern beinhaltete auch die allwöchentlichen Fußballspiele, die eine perfekte Abwechslung zur Astrophysik waren.

Für die sehr gute Zusammenarbeit bedanke ich mich bei Stefano Benetti, Giuliano Pignata, Philipp Podsiadlowski, Ken Nomoto, Keichi Maeda und bei den vielen anderen Mitarbeitern auf diesem Forschungsgebiet. Ohne ihre Hilfe und die wissenschaftliche Unterstützung wäre diese Arbeit kaum möglich gewesen.

Philip Hultzs, Tadius Hoffmann und Christoph Thomas danke ich recht herzlich für die aufwendigen Korrekturarbeiten und die allzeit kompetente Hilfe bei technischen Problemen.

Die angenehme Atmosphäre am Max-Planck-Institut für Astrophysik und der Universitäts-Sternwarte ist allen Mitarbeitern zu verdanken und war meiner Arbeit sehr förderlich. Stellvertretend möchte ich hier Tamara Repolust, André Nickel, Daniel Sauer und Fritz Röepke erwähnen und mich für die vielen wissenschaftlichen und allgemeinen Gespräche sowie die gemeinsamen Unternehmungen außerhalb der Arbeit bedanken.

Meinen Freunden danke ich sehr für die moralische Unterstützung und die Abwechslung, die hin und wieder nötig war: Marcus Hänsel, Manfred Zarnetzki, Philip Hultzs, Christoph Widmer, Gudrun Wind, Johny Setiawan, Harald und Rose Seiler, Christoph Thomas, Sabine Münch und Virginia Borges.

Erwähnen möchte ich an dieser Stelle auch Herrn Fetscher, der mit seinem sehr interessanten Physikunterricht den Anstoß für mein Studium gab.

Mein besonderer Dank gilt meiner Schwester und vor allem meinen Eltern, die mir dies alles ermöglichten und mich weit über die Arbeit jederzeit voll unterstützten.

Von ganzem Herzen danke ich Anja, für alles was sie für mich getan hat.

Lebenslauf

<i>Name</i>	Matthias Stehle	
<i>Geburtsdatum</i>	2. Dezember 1972	
<i>Geburtsort</i>	Sigmaringen	
<i>Staatsangehörigkeit</i>	deutsch	
<i>Schulbildung</i>	1983–1992	Hohenzollern-Gymnasium in Sigmaringen
<i>Zivildienst</i>	1992–1993	
<i>Studium</i>	1993–1998	Studium für das Lehramt an Gymnasien in Physik, Sportwissenschaft und Mathematik an der Albert-Ludwigs-Universität Freiburg i. Br.
	1995–1996	Zwischenprüfung in Physik und Sportwissenschaft
	Apr. 1998	Vordiplom in Physik
	1998–2000	Studium der Physik an der Ludwig-Maximilians-Universität München
	2000–2001	Diplomarbeit am Max-Planck-Institut für Physik, Werner-Heisenberg-Institut, München, Thema: <i>Bestimmung der Masse des neutralen B_s-Mesons mit dem ALEPH-Experiment</i>
<i>Promotion</i>	seit Nov. 2001	Doktorand am Max-Planck-Institut für Astrophysik, Garching und der Universitäts-Sternwarte München

München, 4. November 2004

